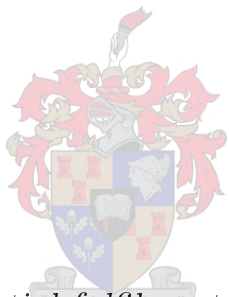


# Obtaining Non-linear Orthotropic Material Models for PVC-Coated Polyester via Inverse Bubble Inflation

by

Charles F Jekel Jr



*Thesis presented in partial fulfilment of the requirements for  
the degree of Master of Engineering (Mechanical) in the  
Faculty of Engineering at Stellenbosch University*

Supervisor: Prof. Gerhard Venter  
Co-supervisor: Dr. Martin Venter

March 2016

# Declaration

By submitting this thesis electronically, I declare that the entirety of the work contained therein is my own, original work, that I am the sole author thereof (save to the extent explicitly otherwise stated), that reproduction and publication thereof by Stellenbosch University will not infringe any third party rights and that I have not previously in its entirety or in part submitted it for obtaining any qualification.

Date: March 2016.

Copyright © 2016 Stellenbosch University  
All rights reserved.

# Abstract

## Obtaining Non-linear Orthotropic Material Models for PVC-Coated Polyester via Inverse Bubble Inflation

C F Jekel Jr

*Department of Mechanical and Mechatronic Engineering,  
University of Stellenbosch,  
Private Bag X1, Matieland 7602, South Africa.*

Thesis: MEng (Mech)

March 2016

Uniaxial tests in the warp, fill, and 45° bias direction were performed on PVC-coated polyester to determine a non-linear orthotropic material model. Optimization was used to minimize the load displacement error of the uniaxial test results and uniaxial finite element models. A method for determining non-linear orthotropic material models from an inverse bubble inflation test is described. The inverse bubble inflation method is demonstrated with a known non-linear orthotropic material model. Inverse bubble inflation analyses were performed on four PVC-coated polyester samples, and a unique non-linear orthotropic material model was determined from each sample. Three point bending tests of inflatable PVC-coated polyester cylinders were used to compare and validate the material models. Finite element models were created replicating the three point bending tests. It was shown that the bubble material models overestimate the stiffness of the inflatable beams, while the uniaxial material model underestimates the stiffness.

# Uittreksel

## Verkryging an Nie-Liniêre Ortotropiese Materiaalmodelle vir PVC-Bedekte Poliêster Deur Omgekeerde Borrel-Opblasning

(“*Obtaining Non-linear Orthotropic Material Models for PVC-Coated Polyester via Inverse Bubble Inflation*”)

C F Jekel Jr

*Departement Meganiese en Megatroniese Ingenieurswese,  
Universiteit van Stellenbosch,  
Privaatsak X1, Matieland 7602, Suid Afrika.*

Tesis: MIng (Meg)

Maart 2016

Eenassige (of uniaksiale) toetse in die skering-, inslag- en  $45^\circ$  skuins-rigtings is uitgevoer op PVC -bedekte poliêster om ‘n nie-liniêre ortotropiese materiaal model vas te stel. Optimering is gebruik om die ladingsverplasingsfout van die uniaksiaaltoets se resultate en uniaksiaal eindige element-modelle te minimeer. ‘n Metode vir die vasstelling van nie-liniêre ortotropiese materiaalmodelle vanaf ‘n omgekeerde borrel-opblaastoets word beskryf. Die omgekeerde borrel-opblaasmetode word gedemonstreer met ‘n bekende nie-liniêre ortotropiese materiaalmodel. Omgekeerde borrel-opblaas-analise is uitgevoer op vier PVC-bedekte poliêster voorbeelde, en ‘n unieke nie-liniêre ortotropiese materiaalmodel is vasgestel uit elke voorbeeld. Drie-punt buigtoetse op die opblaasbare PVC-bedekte poliêster-silinders is gebruik om die materiaalmodelle te vergelyk en te verifieer. Eindige element-modelle is geskep deur die drie-punt toetse te duplikeer. Die resultate het gewys dat die borrel-materiaalmodelle die styfheid van die opblaasbare balke oorskot, en die uniaksiale materiaalmodel die styfheid onderskat.

# Acknowledgements

I would like to express my sincere gratitude to the following people and organizations:

Thanks to Bill Hunt, what started as a stray email lead to the adventure of a lifetime.

Thank you Prof. Gerhard Venter for taking me as a student. Your supervision has been most helpful. I'm very grateful for having the opportunity to study under you in Stellenbosch.

This project would not have been possible without much of the wisdom of Dr. Martin Venter. Thank you for all of the insight.

Many thanks to Johan Stander. Thank you for helping me get set up in the office and acquainting me with the Stellenbosch area.

Thank you Arlene Slabbert for performing the heavy lifting required by the beam tests, and for your support throughout this project.

Thanks to my Mother and Father, this adventure couldn't be possible without your unconditional support.

I would like to thank the Wilhelm Frank Trust for project funding.

Computations were performed using the University of Stellenbosch's Rhasatsha HPC: <http://www.sun.ac.za/hpc>

# Contents

|  |      |
|--|------|
| <b>Declaration</b>   | ii   |
| <b>Abstract</b>  | iii  |
| <b>Uittreksel</b>  | iv   |
| <b>Acknowledgements</b>  | v    |
| <b>Contents</b>  | vi   |
| <b>List of Figures</b>   | viii |
| <b>List of Tables</b>  | xii  |
| <b>1 Introduction</b>  | 1    |
| 1.1 Background . . . . .   | 1    |
| 1.2 Objectives . . . . .   | 3    |
| 1.3 Thesis Outline . . . . .                                       | 5    |
| <b>2 Literature and Concepts</b>                                   | 6    |
| 2.1 FE Material Models and PVC-coated Polyester . . . . .          | 6    |
| 2.2 Bubble Inflation Tests . . . . .                               | 9    |
| 2.3 Inverse Method . . . . .                                       | 10   |
| 2.4 Optimization . . . . .   | 11   |
| 2.5 MSC Marc . . . . .   | 13   |
| 2.6 Digital Image Correlation . . . . .                            | 15   |
| 2.7 Inflatable Beam Bending . . . . .                              | 16   |
| <b>3 Non-Linear Orthotropic Material Model from Uniaxial Tests</b> | 20   |
| 3.1 Experimental Tests . . . . .                                   | 20   |
| 3.2 Virtual Strain Gauge . . . . .                                 | 22   |
| 3.3 Uniaxial Finite Element Models . . . . .                       | 26   |
| 3.4 Optimization of FE Models . . . . .                            | 29   |
| 3.5 Material Models . . . . .                                      | 30   |

|  |           |
|--|-----------|
| <b>4 Inverse Bubble Inflation Method</b>                         | <b>34</b> |
| 4.1 Methodology . . . . .  | 35        |
| 4.2 Surface Fitting . . . . .                                    | 37        |
| 4.3 Optimization . . . . .                                       | 42        |
| 4.4 Results . . . . .  | 45        |
| <b>5 Inverse Bubble Tests</b>                                    | <b>48</b> |
| 5.1 Bubble Inflation Test . . . . .                              | 48        |
| 5.2 Inverse Analysis . . . . .                                   | 50        |
| 5.3 Resulting Non-linear Orthotropic Material Model Comparison . | 55        |
| 5.4 Uniaxial Tests and Material Model Comparison . . . . .       | 58        |
| <b>6 Inflatable Beam Bending</b>                                 | <b>62</b> |
| 6.1 PVC-Coated Polyester Inflatable Cylinders . . . . .          | 62        |
| 6.2 Three Point Bending Test Method . . . . .                    | 62        |
| 6.3 Three Point Bending Test Results . . . . .                   | 66        |
| 6.4 Inflatable Beam Bending FE Models . . . . .                  | 68        |
| 6.5 FE Bending Results of Material Models . . . . .              | 72        |
| <b>7 Conclusion</b>  | <b>78</b> |
| 7.1 Uniaxial Material Models . . . . .                           | 78        |
| 7.2 Inverse Bubble Inflation Method . . . . .                    | 78        |
| 7.3 Bubble Inflation Tests . . . . .                             | 79        |
| 7.4 Inflatable Beam Testing . . . . .                            | 79        |
| 7.5 Future Work . . . . .  | 80        |
| <b>Appendices</b>  | <b>82</b> |
| <b>A Digital Image Correlation on Steel Ball</b>                 | <b>83</b> |
| A.1 DIC Data on Steel Bearing Ball . . . . .                     | 83        |
| A.2 Least Squares Spherical Fit . . . . .                        | 84        |
| A.3 Radius Comparison . . . . .                                  | 86        |
| <b>B Festo SPTE-P10R-S4-V-2.5K Pressure Transmitter</b>          | <b>88</b> |
| <b>C ASM Posiwire WS12-2000-10V-L10 Draw Wire</b>                | <b>90</b> |
| <b>D Three Point Bending Mesh Convergence</b>                    | <b>91</b> |
| <b>List of References</b>  | <b>94</b> |

# List of Figures

|     |  |    |
|-----|--|----|
| 2.1 | Overview of a bubble inflation test setup . . . . .  | 10 |
| 2.2 | Newton-Raphson method for a non-linear FE analysis . . . . .   | 14 |
| 2.3 | Random paint speckle pattern on PVC-coated polyester . . . . .   | 16 |
| 2.4 | Two camera StrainMaster Portable by LaVision GmbH . . . . .  | 17 |
| 3.1 | Fitted polynomials through the load displacement values for five tests in each material direction . . . . .  | 21 |
| 3.2 | Contrast DIC images of uniaxial specimen in the material fill direction with circles highlighting evidence of material slip in the deformed state . . . . .                          | 22 |
| 3.3 | Virtual strain gauge on the initial and deformed uniaxial specimen in the material fill direction where the blue is an overlay of the masked region on the uniaxial sample . . . . . | 23 |
| 3.4 | Load strain gauge displacement values for the uniaxial tests in the Warp, Fill, and 45° bias material directions with fitted polynomial indicated by the solid line . . . . .        | 25 |
| 3.5 | Symmetric FE mesh of the warp uniaxial test with boundary conditions . . . . .   | 27 |
| 3.6 | 45° bias uniaxial test FE mesh with boundary conditions and virtual strain gauge indicated by the green dots in the center of the mesh . . . . .                                     | 28 |
| 3.7 | Load displacement result of the non-linear orthotropic FE models (dashed line) on top of the polynomial fitted to the virtual strain gauge data (solid line) . . . . .               | 31 |
| 3.8 | Non-linear orthotropic material model determined from the simultaneous optimization of the three FE models, where each modulus is limited to the failure strain . . . . .            | 32 |
| 4.1 | Mesh used for the bubble inflation FE model . . . . .  | 35 |
| 4.2 | Normalized maximum displacement value of FE bubble inflation model for various Poisson's ratios . . . . .  | 37 |
| 4.3 | Non-linear orthotropic material model moduli as functions of strain . . . . .  | 38 |
| 4.4 | Nodal displacement $x$ values on the fitted fourth order polynomial surface at 300 kPa . . . . .   | 39 |

|  |    |
|--|----|
| 4.5 Nodal displacement $y$ values on the fitted fourth order polynomial surface at 300 kPa . . . . .   | 40 |
| 4.6 Nodal displacement $z$ values on the fitted fourth order polynomial surface at 300 kPa . . . . .   | 40 |
| 4.7 Displacement $z$ nodal values against the displacement $z$ polynomial fitted values at 300 kPa . . . . .   | 41 |
| 4.8 Optima sorted from worst to best of optimization results from 50 random starting points . . . . .  | 45 |
| 4.9 Five best material models resulting from the optimization of 50 random starting points plotted alongside known solution . . . . .                            | 46 |
| 4.10 Node locations cut through the $y$ axis from the FE bubble inflation models of the five best material models plotted alongside the known solution . . . . . | 47 |
| 4.11 Node locations cut through the $x$ axis from the FE bubble inflation models of the five best material models plotted alongside the known solution . . . . . | 47 |
| <br>5.1 Top plate resting on the base of the aluminum bubble inflation test fixture . . . . .  | 49 |
| 5.2 Maximum strain values in the warp direction ( $\varepsilon_1$ ) of bubble inflation test 3 overlaid on the DIC image . . . . .                               | 51 |
| 5.3 Maximum strain values in the fill direction ( $\varepsilon_2$ ) of bubble inflation test 3 overlaid on the DIC image . . . . .                               | 52 |
| 5.4 Maximum strain values in the shear direction ( $\gamma_{12}$ ) of bubble inflation test 3 overlaid on the DIC image . . . . .                                | 53 |
| 5.5 Displacement $z$ nodal values against the displacement $z$ polynomial fitted values at 328 kPa of bubble inflation test 3 . . . . .                          | 54 |
| 5.6 Optima sorted from worst to best objective function of optimization results from 50 random starting points for the four bubble inflation tests . . . . .     | 55 |
| 5.7 Non-linear orthotropic $E_1$ determined from the uniaxial and inverse bubble inflation tests limited to the maximum strain value . . . . .                   | 56 |
| 5.8 Non-linear orthotropic $E_2$ determined from the uniaxial and inverse bubble inflation tests limited to the maximum strain value . . . . .                   | 57 |
| 5.9 Non-linear orthotropic $G_{12}$ determined from the uniaxial and inverse bubble inflation tests limited to the maximum strain value . . . . .                | 58 |
| 5.10 Warp uniaxial test and the results of the uniaxial FE models utilizing the bubble inflation material models . . . . .                                       | 59 |
| 5.11 Fill uniaxial test and the results of the uniaxial FE models utilizing the bubble inflation material models . . . . .                                       | 60 |
| 5.12 45° bias uniaxial test and the results of the uniaxial FE models utilizing the bubble inflation material models . . . . .                                   | 61 |

|      |   |    |
|------|---|----|
| 6.1  | Three PVC-coated polyester cylinders with diameters of 150 mm, 200 mm, 250 mm . . . . .   | 63 |
| 6.2  | Inflatable cylinder valve on the end cap and seam running down the length of the cylinder . . . . .   | 64 |
| 6.3  | 150 mm inflatable cylinder bending in the test setup . . . . .  | 65 |
| 6.4  | Dimensions in mm of three point bending test setup . . . . .  | 65 |
| 6.5  | Center load displacement of the three point bending test on the 150 mm diameter cylinder for three different inflated pressures . . .                           | 67 |
| 6.6  | Center load displacement of the three point bending test on the 200 mm diameter cylinder for three different inflated pressures . . .                           | 68 |
| 6.7  | Center load displacement of the three point bending test on the 250 mm diameter cylinder for three different inflated pressures . . .                           | 69 |
| 6.8  | 150 mm diameter inflatable cylinder at the buckling load in the three point bending test configuration . . . . .  | 69 |
| 6.9  | Inflated 150 mm diameter cylinder in MSC Marc with rigid elements replicating the three point bending boundary conditions . . .                                 | 70 |
| 6.10 | Bending 150 mm diameter inflatable cylinder FE model due to the displacement controlled rigid collar . . . . .  | 70 |
| 6.11 | Pressure volume work of three point bending 150 mm diameter cylinder inflated to 140.0 kPa . . . . .  | 72 |
| 6.12 | Three point bending load displacement results of 150 mm diameter cylinder inflated to 90 kPa compared to FE analyses using different material models . . . . .  | 73 |
| 6.13 | Three point bending load displacement results of 150 mm diameter cylinder inflated to 110 kPa compared to FE analyses using different material models . . . . . | 74 |
| 6.14 | Three point bending load displacement results of 150 mm diameter cylinder inflated to 140 kPa compared to FE analyses using different material models . . . . . | 74 |
| 6.15 | Three point bending load displacement results of 200 mm diameter cylinder inflated to 60 kPa compared to FE analyses using different material models . . . . .  | 75 |
| 6.16 | Three point bending load displacement results of 200 mm diameter cylinder inflated to 80 kPa compared to FE analyses using different material models . . . . .  | 75 |
| 6.17 | Three point bending load displacement results of 200 mm diameter cylinder inflated to 100 kPa compared to FE analyses using different material models . . . . . | 76 |
| 6.18 | Three point bending load displacement results of 250 mm diameter cylinder inflated to 50 kPa compared to FE analyses using different material models . . . . .  | 76 |
| 6.19 | Three point bending load displacement results of 250 mm diameter cylinder inflated to 65 kPa compared to FE analyses using different material models . . . . .  | 77 |

|   |    |
|---|----|
| 6.20 Three point bending load displacement results of 250 mm diameter cylinder inflated to 85 kPa compared to FE analyses using different material models . . . . . | 77 |
| A.1 52,080 DIC data points captured from the surface of the steel bearing ball plotted in 3D . . . . .  | 84 |
| A.2 52,080 DIC data points approximately captured 90° from the surface of the steel bearing ball plotted in the <i>xz</i> plane . . . . .                           | 85 |
| A.3 52,080 DIC data points approximately captured 144° from the surface of the steel bearing ball plotted in the <i>yz</i> plane . . . . .                          | 86 |
| A.4 52,080 DIC data points captured from the surface of the steel bearing ball plotted in 3D on top of the fitted sphere . . . . .                                  | 87 |
| B.1 Agreement of raw SPTE and Wiki Instruments pressure values . . .  | 89 |
| C.1 Agreement of ASM Posiwire WS12-2000-10V-L10 draw wire position sensor and meter stick displacement measurements . . . . .                                       | 90 |
| D.1 Demonstrated load displacement mesh convergence for the 150 mm cylinder in three point bending . . . . .  | 91 |
| D.2 Demonstrated load displacement mesh convergence for the 200 mm cylinder in three point bending . . . . .  | 92 |
| D.3 Demonstrated load displacement mesh convergence for the 250 mm cylinder in three point bending . . . . .  | 93 |

# List of Tables

|     |  |    |
|-----|--|----|
| 3.1 | Virtual strain gauge values including: initial length $l_i$ , final length $l_f$ , maximum engineering strain $\varepsilon$ (mm/mm), and coefficient of determination $R^2$ of the fitted polynomial . . . . . | 24 |
| 3.2 | Variables determined from the optimization of the uniaxial test cases that define the non-linear orthotropic material model of Eqs. 3.1-3.3 . . . . .  | 33 |
| 4.1 | Coefficient of determination for the polynomials used to define the bubble displacements . . . . .   | 41 |
| 4.2 | Variables and bounds used for the non-linear orthotropic material model . . . . .  | 44 |
| 5.1 | Maximum engineering strain values (mm/mm) of the bubble tests in the warp ( $\varepsilon_1$ ), fill ( $\varepsilon_2$ ), and shear ( $\gamma_{12}$ ) material directions . . . . .                             | 50 |
| 5.2 | The seven unique pressures (kPa) used for the inverse analysis of the recorded bubble tests . . . . .  | 51 |
| 5.3 | Coefficient of determination for the polynomials used to define the DIC displacements of bubble inflation test 4 . . . . .   | 53 |
| 5.4 | Variables of the non-linear orthotropic material models determined from the inverse analysis on the four bubble tests . . . . .  | 56 |
| 6.1 | This table shows the various diameters of inflatable cylinders along with the operating pressures used for the three point bending tests   | 66 |
| A.1 | Radius determined by spherical least squares fit to five sets of DIC images on steel bearing ball . . . . .  | 86 |

# Chapter 1

## Introduction

This chapter provides the background and motivation for investigating PVC-coated polyester, followed by a discussion of the objectives, goals, and contributions of this research. The layout of this thesis is presented at the end of this chapter.

### 1.1 Background

A structure for which additional stiffness and rigidity is obtained from an internalized pressure is an inflatable structure. Inflatable structures are useful in a variety of applications. Often inflatable structures are known to be a cheap and lightweight alternative to conventional structures. Most inflatable structures are made from pliable material which can be rolled up and folded for storage. These structures can thus be stored compactly when deflated, and deployed rapidly when inflated. This high stowed to deployed volume ratio, in addition to rapid deployment, and high strength-to-weight nature have allowed for inflatable structures to be found in a wide variety of applications such as temporary shelters, roofs, and portable bridges.

An inflatable structural concept was presented in 2004 called Tensairity<sup>®</sup>, which physically separates the tension and compression elements of a beam with a pressurized volume (Luchsinger *et al.*, 2004). Tensairity<sup>®</sup> structures have been used in the civil engineering field for creating lightweight roofs and bridges. To demonstrate the potential of Tensairity<sup>®</sup>, a mobile bridge was made, by Luchsinger *et al.* (2011), with an 8 m span from two Tensairity<sup>®</sup> girders. Each girder had a mass of 68 kg, and both girders fit inside the trunk of a small car. The girders can be assembled into a bridge in under 30 minutes. A small car was then parked on top of the bridge. This temporary bridge is just one demonstration of the rapid deployment and efficient volume storage potential of inflatable structures.

Inflatable structures have also been examined as wings on Unmanned Aerial Vehicles (UAVs). Norris and Pulliam (2009) discussed a history of inflatable

UAV wings with the first inflatable wing on a UAV dating back to the 1970s. A majority of the inflatable wings presented allowed for the wings to be packed tightly around the fuselage of the UAV. This configuration greatly reduces the profile of the entire UAV allowing for easier storage. An additional benefit is that the inflatable wings can be made lighter than conventional wings. Altogether the use of inflatable wings greatly improves the stowed to deployed volume of UAVs. However, much is unknown about the performance capabilities and limitations of inflatable wings.

Over the last decade, wind turbine capacities have continued to increase, resulting in larger wind turbine blades. Some of the largest blades, such as the Siemens B75, are 75 m long and weigh 25 tons. It is very expensive and logistically challenging to transport these large turbine blades to their site location. NREL's 2010 Cost of Wind Energy Review (Tegen *et al.*, 2012) showed that the single most expensive individual component of a 1.5 MW system wind turbine were the blades based on the land-based levelized cost of energy. As discussed, inflatable structures tend to be cheaper alternative to conventional structures while providing for efficient storage and transportation. Thus developing an inflatable wind turbine or fan blade may prove to be a favorable addition to conventional blade technology. However unlike inflatable UAV wings, there has hardly been any development in rotating inflatable blades.

There are a number of patents for inflatable wind turbine blades, however most patents fail to mention practical information such as specific materials, operating pressures, and seal locations. A GE patent filed in 2009 for an inflatable wind turbine blade uses an inflatable cavity and flexible skin (Cairo, 2011). When the inflatable cavity is inflated, the structure is stiffened, pulling the flexible skin into the shape of an airfoil. Potentially such a cavity could be made from inflatable air cylinders. A more complex design is shown in a 2008 German patent, which can use multiple inflatable cavities covered by a cloth to make up the blade's surface (Roland and Martin Fritzsche, 2008). Both of these patents show how concepts of an inflatable blade may work, while highlighting the advantages of an inflatable blade, but lack the detail necessary to create a working blade. A Chinese patent discusses a semi-inflatable blade of which the leading edge is non pressurized and rigid, but the trailing edge is made from a pressure filled fabric (ZENG, 2013). This design opens the possibility of a hybrid blade, in which there is a solid torque transfer beam that is attached to a pressurized airfoil. Overall, the patents demonstrate interest in inflatable blades while lacking solid examples and proof of their concepts. Since inflatable rotary blades are largely an underdeveloped technology, the potential research scope of investigating inflatable blades is tremendous, spanning across a number of engineering disciplines.

The design of new structures often requires some form of numerical analysis. The Finite Element (FE) method has been an important tool used to predict the load, deflection, and failure of fabric structures. FE models of inflatable structures provide information that is beneficial to the design process.

The ability to predict structural compliance and approximate failure allows engineers to intelligently evaluate design performance. However, the accuracy of these models depends largely on the ability for the material model to replicate the physical behavior of the material. It is a common subject of many research papers to investigate the method for obtaining suitable material models.

This thesis investigates the method of obtaining a material model suitable for FE analysis of inflatable structures. A new inverse bubble inflation test method is proposed and investigated, with a goal of making it easier to obtain a non-linear material model for various membrane materials used in inflatable structures. The performance of material models derived from the inverse bubble test and conventional uni-axial testing will be evaluated and compared. All FE analysis were performed in MSC Marc, an implicit non-linear FE solver. The material models will be experimentally validated utilizing a separate load case.

Cesair Inflatables, a specialty manufacturer of inflatable racing boats, was contacted for assistance with this project. The inflatable racing boats they manufacture are made from PVC-coated polyester fabric, a common membrane material. Caesar Inflatables made three inflatable cylinders for the experimental validation of the material models. These cylinders were modeled in MSC Marc, and physically tested under a three-point bending load case. The accuracy of the numerical model at predicting the bending behavior of the inflatable cylinder will largely depend upon the performance of the material model.

This thesis is a contribution to the ongoing research in inflatable structures. Details on obtaining a non-linear orthotropic material model from uni-axial testing, along with the test data on PVC-coated polyester will be provided. The new inverse bubble inflation technique serves to provide an improved method for obtaining accurate material models for a variety of inflatable membrane materials. The creation of FE models of an inflatable cylinder and inflated bubble are discussed in detail. The methods for creating these numerical models are not limited to cylinders and bubbles, and will be applicable for a variety of other inflatable structures.

## 1.2 Objectives

This thesis develops a material model for PVC-coated polyester. The PVC-coated polyester under investigation is VALMEX® 7318 5340 manufactured by Mehler Technologies GmbH. The processes of obtaining this material model should be simple, robust, and applicable for other membrane material used in inflatable structures. For these reasons an inverse bubble inflation test is purposed to be favorable over traditional uni-axial testing. The method developed to determine material parameters from the inverse bubble inflation test serves as a black box. The test data can be entered into the black box

which produces a material model. This finished product can greatly reduce the required time by the engineer to develop a material model for a structural membrane, in addition reducing the required number of tests. The bubble inflation test subjects the material to a complex load case, which may make it possible to develop a material model that would otherwise be difficult to obtain from conventional methods. The material models and FE analysis of the inflatable structures are performed in MSC Marc, however the principles and processes covered in this thesis will be applicable to other non-linear FE solvers.

As with all numerical models, the model's capability of replicating reality is largely unknown without some form of experimental validation. For this reason three inflatable cylinders have been manufactured from PVC-coated polyester with the intent of providing the experimental validation for the material model and numerical analysis. The cylinders are subjected to a three point bending test, intended as a simple load case in which the boundary conditions are easily replicated in a FE analysis of the test. The capabilities of the material model and numerical analysis will be defined by how well the physical test results are matched.

It is the intention of the processes developed in this thesis to prove useful in the design and analysis of inflatable structures. The ability for material models to accurately replicate the material's physical behavior is a widely studied research field, influenced by many factors. It is very easy to develop complicated models that are impractical to be utilized at a design stage by being either too time consuming to develop, computational impractical, or both. Furthermore, many characteristics of the material behavior will not be investigated because of a time constraint. Thus it is important to narrow the focus of this project by mentioning subjects that won't be investigated.

It is known that the PVC-coated polyester under investigation may exhibit highly non-linear behavior. Complicated non-linear behavior include material creep, biaxial load-ratio dependencies, and load rate dependencies. Much of this behavior is largely out of the scope of this project, but may be suitable for future work. The purpose of this work is to prove useful from a design perspective, which ultimately leads to accurately predicting a load deformation response through FE analysis. Further material behavior can be researched and added to the material model which accurately represents the load deformation response. Thus to serve as a starting point, this project focuses on obtaining load deformation behavior of the PVC-Coated polyester for implementation in the FE method.

The computational intensity of the material model should not inhibit the modeling of an entire inflatable structure. It is the fundamental goal that the methods developed in this thesis will be useful as a design tool when analyzing inflatable structures. Thus potential material models and approaches deemed too computational expensive will not be explored further in this thesis. The material models developed should be simple to implement while maintaining

efficiency when modeling a complete structure.

Only one material is tested in this thesis. While the material of focus for this thesis is PVC-coated polyester, the goal is not to present the material model for this material. Rather the focus of this project lies in the methods utilized in obtaining material behavior for use in the FE method. Specifically, the capability of the new inverse bubble inflation test in comparison to traditional tests on PVC-coated polyester. The contributions lie in the development of the inverse bubble test, serving as a simpler tool for obtaining material models for inflatable membrane materials.

A two dimensional non-linear elastic orthotropic material model is investigated for modeling the behavior of PVC-coated polyester. Structural membrane materials, used in inflatable structures, are generally modeled as orthotropic materials. Although this investigation only looks at PVC-coated polyesters, the non-linear orthotropic material model determined from inverse bubble inflation is applicable for other structural membrane materials.

The objectives of this thesis are summarized by the following points:

- Obtain a material model for PVC-coated polyester from conventional testing
- Define a black box method to test and obtain material models
- Use the black box method to obtain a material model, then compare the material models resulting from the black box and conventional tests
- Experimentally validate the material models by testing an inflatable structure, and determine which method produced the best material model

### 1.3 Thesis Outline

Throughout the entirety of this project, a collection of literature was accumulated and analyzed. The results of the literature study are found in Chapter 2. The results of uni-axial testing on the PVC-coated polyester are presented in Chapter 3, along with the material model developed from these tests. The methodology utilized in the inverse bubble inflation test is discussed in Chapter 4. Followed by the test results and discussion of the inverse bubble inflation tests on the PVC-coated polyester in Chapter 5. The experimental validation of the material models utilizing the inflatable cylinders is found in Chapter 6. The results of this project are concluded in Chapter 7 with the discussion of future work.

# Chapter 2

## Literature and Concepts

This chapter discusses theory, concepts, and literature necessary for understanding the work presented in this thesis. The chapter begins by discussing the various material models, and methods used to obtain the models for PVC-coated polyester in literature. A quick overview of bubble inflation tests and the inverse method is provided. Optimization was used throughout this project, so a background on optimization is presented. All finite element (FE) analyses in this thesis were solved with the non-linear FE solver MSC Marc, thus a brief description on how MSC Marc differs from conventional linear FE solvers is provided. Digital Image Correlation (DIC) methods and systems used throughout this project are explained. Lastly, the chapter ends with a literature review on inflatable beam testing.

### 2.1 FE Material Models and PVC-coated Polyester

Technical woven textiles, including PVC-coated polyester, are generally assembled utilizing two distinct yarn directions. These yarn directions are known as the warp and fill. The fill yarn is also commonly referred to as weft. In a typical weave, the warp yarns are pulled taut while the fill yarns are threaded through the warp yarns. As a result of the weave assembly, the warp and fill yarns lay orthogonal to each other in the plane of the fabric. Woven textiles are known to exhibit complex material behavior, largely due to their construction. Since yarns in the warp direction were previously tensioned unlike in the fill direction, it is expected that the material will exhibit a stiffer response in the warp direction. The interactions between the coated matrix and the woven yarns adds an additional layer of complexity for coated fabrics.

It is a difficult and widely researched topic to generate material models, suitable for the FE method that are capable of reproducing the behavior of woven textiles. The complex behavior, due to the assembly, of woven textiles further increases the difficulty of creating material models. While many dif-

ferent material models have been used to replicate the mechanical behavior of woven textiles, they generally fall into one of two categories: micromechanical or macromechanical.

Micromechanical models analyze the microscopic interactions of the material. For coated fabrics this would include the complicated behavior of woven fabrics such as crimp interchange, friction and contact between yarns, various extensions of the yarn directions, as well as the interaction between yarns and the coating. It is impractical to model a complete structure with these yarn interactions with the FE method, thus micromechanical models tend to be limited to just a unit cell which is representative of the fiber interactions. The unit cell would thus be used to generate the constitutive relations for a macromechanical material model suitable for the FE analysis of an entire inflatable structure.

Macromechanical models assume the material to be of a single continuum, for which the constitutive relationships can be determined from material testing. Often uniaxial and biaxial tests are performed on the material, in which case the experimental stress/strain relationship is used to characterize the material. An example of a macromechanical material model would be the plane stress constant thickness orthotropic model. This model has been commonly used, for membrane structures, because of the model's ability to exhibit direction dependent stiffness. Four constants are needed to define the material model, the Young's moduli in the warp and fill directions ( $E_1, E_2$ ), Poisson's ratio ( $\nu_{12}$ ), and the shear modulus ( $G_{12}$ ). If a material does not exhibit linear behavior, a non-linear material model can be used to improve the accuracy of the FE model.

PVC-coated polyester has been known to exhibit anisotropic behavior. Chen *et al.* (2007) performed uni-axial tests on PVC-coated polyester for varying bias angles of 15°, 30°, 45°, 60°, and 75°, as well as the warp and fill material directions. A unique stress strain curve was found for each test, demonstrating the anisotropic material behavior of the coated fabric. Despite this anisotropic behavior, it was found that a linear orthotropic elastic material model was suitable for replicating the uniaxial tests in the warp, fill, and 45° bias directions within 20 percent of the failure tensile strength.

Cavallaro *et al.* (2003) attempted to model a woven inflatable beam with a micromechanical material model. Symmetry was used to simplify the FE model. The FE model included individual yarn interactions such as contact and friction, as well as a bladder, but the model was plagued with convergence problems and deemed too computationally expensive. Thus a macromechanical material model was used to model the entire air beam. A unit cell model, consisting of beam elements, was utilized to obtain the parameters for a linear orthotropic material model. Shell elements were utilized to model the woven air beam in a bending case, which represented an experimental bending test on the beam. However, the FE model did not correlate well with experimental test results. This poor correlation was blamed on the ma-

terial model's inability to capture the non-linear shear response of the woven textiles.

It has been observed that the strength of coated fabrics in the warp and fill directions is dependent upon the ratio of the load in their respective directions. Galliot and Luchsinger (2009) performed biaxial extensions of PVC-coated polyester. The tests investigated the load ratio dependent behavior of the material, by subjecting the material to five different load ratios of 5:1, 2:1, 1:1, 1:2, and 1:5. The biaxial test subjected the material warp and fill directions to distinct loads, with a 5:1 load ratio meaning that the load in the warp direction was 5 times more than the load in the fill direction. Young's moduli were calculated in the two material directions for each test. A unique Young's modulus was then determined for each test, in both the warp and fill directions. A non-linear material model was proposed which accounted for the different responses upon the load ratio. The material model was fundamentally a plane stress linear orthotropic material model. Unique Young's moduli for both the warp and fill directions ( $E_1, E_2$ ) were determined at each iteration, based upon the elemental stress ratios. The end result was a non-linear material model capable of exhibiting load ratio dependent behavior without an increase to computational time.

Both uniaxial and biaxial tensile tests were conducted on PVC-coated polyester by Ambroziak and Kłosowski (2014). The uniaxial tests were conducted in the material warp and fill directions. Seven different load ratios of 8:1, 4:1, 2:1, 1:1, 1:2, 1:4, 1:8 were investigated for the biaxial tests. Stress strain curves were calculated in both material directions from the resulting tests. It was found that nearly identical stress strain curves were produced from the 1:1 biaxial load and the uniaxial tests. Thus uniaxial tests in the warp and fill direction are a good approximation of the biaxial stress state resulting from a 1:1 load ratio. In addition, all load ratios produced very similar stress strain relationships. The coefficients of determination between stress strain curves from the various load ratios were above 0.9. While load ratio dependent behavior is present, this suggests it is not the dominating factor in the material non-linearity. It was noted that the non-linear stress strain curves exhibited by the material could be well approximated utilizing a piece-wise linear function. In an effort to capture the non-linearity of the PVC-coated polyester, a tri-linear orthotropic material model was proposed. This material model is a plane stress linear orthotropic material model utilizing three different Young's moduli for both  $E_1$  and  $E_2$ . The Young's moduli are defined only for a particular strain region. Once an element exceeds the strain region of a defined modulus, a new Young's modulus is assigned. The result is a simple non-linear material model that correlated well with the experimental data.

In summary, the inherent non-linear behavior of coated fabrics has been widely documented. To model a complete inflatable structure at the micro level with yarn interactions has proven to be too computationally expensive. Thus,

PVC-coated polyester is typically modeled in the FE method as a plane stress linear orthotropic material. While the linear orthotropic material model is simple to implement, non-linear material models may more accurately describe the material response. One such material model discussed was a tri-linear orthotropic material model.

## 2.2 Bubble Inflation Tests

Bubble inflation tests are a popular method for introducing an equal biaxial load case, especially in cases where very large deformations may inhibit the ability for a conventional biaxial test. The bubble inflation tests have been used to characterize polymers such as Ethylene Tetra Fluoro Ethylene (ETFE) and even flour/water dough. A Bubble inflation test is made by clamping a material sample to a circular clamp. A medium is introduced on one side of the material, applying a pressure to the material. The material on the inside of the clamp is free to deform, creating a bubble shape from the pressure load. Image tracking techniques, such as DIC, can be used to track the deformation of the material. A simple overview of a sample bubble inflation test setup can be seen in Figure 2.1. Although the deformation of coated fabrics isn't expected to be as much as other polymer foils, the bubble inflation test still introduces a 1:1 biaxial load case at the center point of the material sample.

Bubble inflation tests are useful in obtaining the biaxial stress strain curve for a highly deformable material. It is generally assumed that the bubble, resulting from inflation, is spherical in shape. Reuge *et al.* (2001) and Charalambides *et al.* (2002) used a single camera to measure the bubble height while Galliot and Luchsinger (2011) used a two camera DIC system. Assuming that the material is incompressible, it is possible to approximate the strain with the bubble height and radius of the test fixture. Pressure vessel theory is used to calculate the stress with the assumed spherical shape and the bubble height. This results in a stress strain relationship for a 1:1 biaxial load case.

Galliot and Luchsinger (2011) performed uniaxial, biaxial, and bubble inflation tests on ETFE. Nearly identical stress strain relationships were developed for each test. However, only the uniaxial and bubble test could be used to evaluate the material failure. This was because the ETFE foils did not fail in the biaxial test device, due to the physical limitation of the biaxial test structure. Bubble inflation tests are not physically limited to a strain range, because bubble inflation test fixtures have no moving components unlike a conventional biaxial test device.

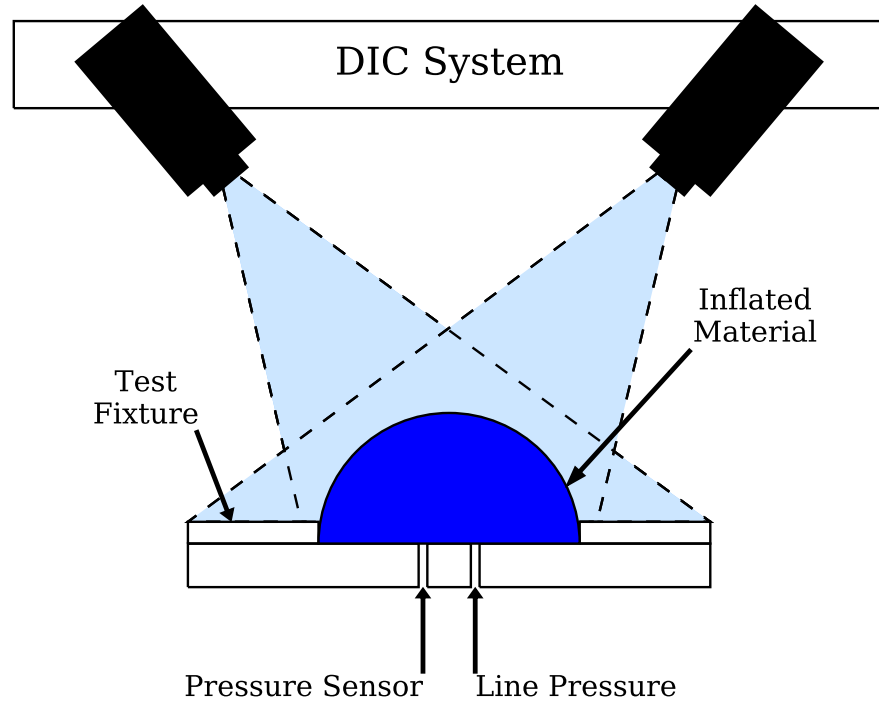


**Figure 2.1:** Overview of a bubble inflation test setup

### 2.3 Inverse Method

There are direct and inverse methods for obtaining material models. Uniaxial and biaxial tensile tests are commonly used to characterize the mechanical behavior of coated fabrics. With the direct method, a physical test is conducted to determine the material's constitutive relationship. The resulting experimental relationship is passed directly into the material model of an FE analysis that replicates the testing conditions. Ideally, it is then shown that the material model is capable of replicating the behavior of the physical test.

The inverse method is fundamentally different from the direct method. With the inverse method, an FE analysis is created replicating the conditions of the physical test first. Optimization is then used to determine the best material model parameters by minimizing the difference between the FE analysis and the physical test results. While each method has advantages, the inverse method may reduce the engineering time required to create material models suitable for FE analysis. More importantly, the material can be characterized

with a load state that is more complex than traditional uniaxial or biaxial testing. This added complexity may be more representative of reality. Materials such as technical woven textiles or coated fabrics violate continuum mechanics in a macro sense as the material is not represented by a single continuum. Thus the homogenization of the material into discrete elements for use in the FE method may be a cumbersome task. The inverse method is capable of determining the best homogenized FE material model representative of a complex load state.

Garbowski *et al.* (2011) used the inverse method to characterize paper by performing biaxial tests on paper. A circular hole was cut in the center of the biaxial test sample to increase the inhomogeneous response field. DIC was used to capture the full field displacements of the test samples. The physical test was reproduced in an FE analysis. The deformation of the cruciform specimen is then compared to the nodes of the FE model. An elastic-plastic orthotropic material model was thus determined with much success by optimizing the parameters of the material model, minimizing the differences between the FE model and the deformations of the test specimen. In the end a software package was created suitable for determining the constitutive relationship of test specimens that can be performed on a portable computer.

## 2.4 Optimization

The inverse method utilizes optimization to determine the best material model parameters. Fundamentally, optimization is a tool used to determine the best solution to a mathematically defined problem. The general form of an engineering optimization problem is arranged in Eq. 2.1. The goal of the optimization is to minimize the objective function, represented by  $f(x)$ . The design point  $x$  consists of each variable  $x_i$  that influences the objective function, constraints, or both. The lower and upper bounds are denoted by  $x_{iL}$  and  $x_{iU}$ , for each variable. The feasibility of an optimization problem can be defined mathematically by a set of constraints. The optimization is subject to the inequality constraints  $g_j(x)$  and the equality constraints  $h_k(x)$ .

$$\begin{aligned} & \text{minimize} && f(x), \quad x = [x_1, x_2, \dots, x_i]^T \\ & \text{subject to} && g_j(x), \quad i = 1, 2, \dots, q \\ & && h_k(x), \quad j = 1, 2, \dots, r \\ & && x_{iL} \leq x_i \leq x_{iU}, \quad k = 1, 2, \dots, s \end{aligned} \tag{2.1}$$

There are a number of different optimization algorithms, however most fall into one of two broad categories: gradient based optimization and non-gradient based optimization. Gradient based optimization algorithms begin from a single design point. Finite difference steps are typically performed for

each variable to obtain a search direction. A line search is performed based on the search direction to improve upon the previous design point. Once the best objective function has been found in this search direction, a new set of finite difference steps are calculated on the newly found best design point. This process is repeated until convergence is demonstrated.

As implied by the name, non-gradient based optimization methods do not use gradient information to find the optimum design point. In general non-gradient methods utilize a set of design points, while gradient methods begin from a single design point. The inspiration behind many non-gradient optimization algorithms has come from observations of nature. Popular algorithms include the genetic algorithm, the particle swarm algorithm, and other evolutionary based algorithms.

The best performing optimization algorithm is predominately unique for each specific engineering problem. With the inverse method, an optimization is performed with a FE analysis to determine a material model. Thus each time the objective function is evaluated an FE analysis is performed. The optimization algorithm should be chosen in a circumspect manner, because the number of FE analyses performed dictates the computational intensity of the method.

It is not the focus of this thesis to benchmark different optimization algorithms for one specific inverse problem, rather it is the focus to demonstrate that the inverse method is capable of producing material models suitable for the FE analysis of inflatable structures. Once the method has been demonstrated to be successful, the inverse method may be tweaked for performance characteristics. Gradient optimization was chosen as a reasonable method for the initial investigation of the inverse method.

Snyman (2005) recommends the use of gradient over non-gradient optimization methods based on his experience, stating that he believes non-gradient methods are too computationally expensive to be viable. Snyman also states, that through careful use of gradient based methods, it is possible to solve problems with multiple minima and numerical noise. For single objective gradient based constrained optimization, Venter (2010) states that three algorithms are commonly encountered for engineering purposes: the Sequential Linear Programming (SLP) algorithm, the Sequential Quadratic Programming (SQP) algorithm, and the Modified Method of Feasible Directions (MMFD) algorithm. All three algorithms were utilized in this thesis, however the MMFD algorithm was found to consistently perform the best throughout this investigation.

Vanderplaats Research & Development Inc. (2001) Design Optimization Tools (DOT) was the optimization library used in the work presented in this thesis. DOT is a multi-purpose gradient based software library designed for engineering applications. For the inverse method, a simple Python script interfaces with DOT and the MSC Marc input file. The material model variables are fed into DOT as variables to optimize. The optimization goal is to minimize the error between the FE model bubble displacements and the known

displacements. DOT was designed to be useful as an engineering optimizer, so the algorithm attempts to stay in the feasible region as much as possible during the one dimensional search.

## 2.5 MSC Marc

Non-linear FE analysis is used rather than linear FE analysis when the non-linearity is important in the analysis of the structure. In many engineering applications non-linear behavior may occur with the material, loading, or boundary conditions. The non-linear FE analysis software used throughout this thesis is MSC Marc. Marc is an implicit non-linear FE analysis solver, which utilizes the Newton-Raphson method to solve non-linear FE analyses. This section shows how Marc uses the Newton-Raphson method to solve non-linear FE analyses, by deriving the governing equations.

The governing equation of a linear static FE analysis is seen in Eq. 2.2. Where  $\mathbf{K}$  is the stiffness matrix,  $\mathbf{u}$  is the nodal displacement vector, and  $\mathbf{r}$  is the nodal force vector.

$$\mathbf{K}\mathbf{u} = \mathbf{r} \quad (2.2)$$

The linear equation is solved for the nodal displacements vector, as seen in Eq. 2.3. It is important to mention that the stiffness matrix is never inverted in practice, rather a linear equation solver is used to determine the nodal displacement vector. Representing this solver as an inverted matrix helps to keep the notation concise.

$$\mathbf{K}^{-1}\mathbf{r} = \mathbf{u} \quad (2.3)$$

With a non-linear FE analysis, both the stiffness matrix and the nodal force vector may be defined as functions of the incremental nodal displacement vector, as seen in Eq. 2.4. For example, a non-linear strain dependent material model can be represented as a stiffness matrix that is a function of the nodal displacement vector. A surface pressure load is an example of when the load will be a function of the displacement vector, because the nodal load vector becomes a function of the orientation of the structure.

$$\mathbf{K}(\mathbf{u}_n)^{-1}\mathbf{r}(\mathbf{u}_n) = \mathbf{u}_n \quad (2.4)$$

MSC Marc utilizes the Newton-Raphson method to solve for the nodal displacement vector, as seen in Eq. 2.5. The entire load of the non-linear FE analysis is split up into separate  $n$  increments. The initial nodal displacement vector of that increment is then updated in  $i$  iterations until convergence is demonstrated.

$$\mathbf{K}(\mathbf{u}_n^{i-1})^{-1}\mathbf{r}(\mathbf{u}_n^{i-1}) = \mathbf{u}_n^i \quad (2.5)$$

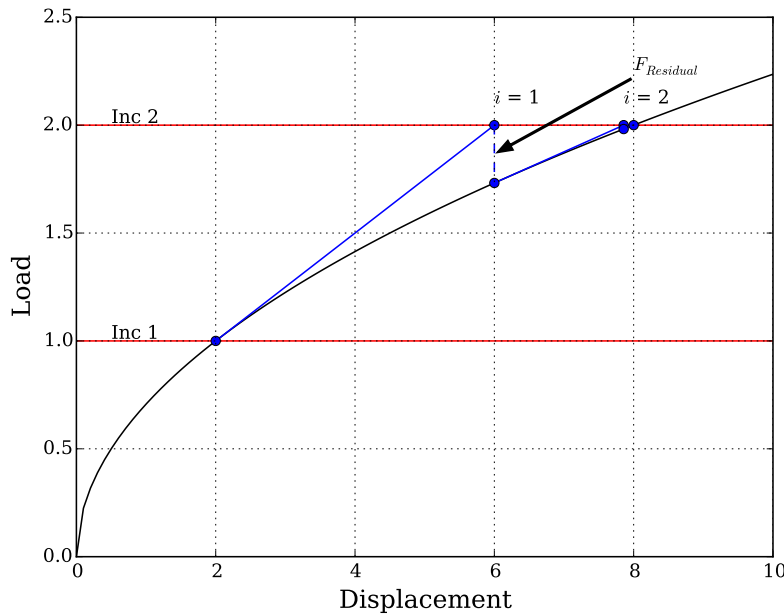


**Figure 2.2:** Newton-Raphson method for a non-linear FE analysis

The Newton-Raphson method can be visualized in Figure 2.2, where an arbitrary structure produces the non-linear load displacement curve. A load of 2 is applied from the solution of increment 1, to the first iteration of increment 2. The stiffness matrix and load vectors are assembled utilizing the nodal displacement vector from the solution of increment 1, and Eq. 2.5 is solved for a new displacement vector  $\mathbf{u}^1$ . This solution is not correct because the structure does not exert a force equal to, 2.0, the applied force. This resulting difference is the  $F_{Residual}$  residual force, which represents the amount of force out of equilibrium. A new stiffness matrix and load vector are assembled with the previous found displacement vector of  $\mathbf{u}^1$ . The Eq. 2.5 is solved again for a new displacement vector. A residual force can be seen at the end of iteration 2, which suggest that the solution has not yet been found. The process repeats until the convergence criteria is satisfied.

The user can define three types of convergence controls in Marc; residual checking, displacement checking, and strain energy checking. Residual checking minimizes the maximum nodal residual force and is normalized with respect to the maximum nodal  $F_{Reaction}$  reaction force as expressed in Eq. 2.6. This effectively minimizes the out of equilibrium force to a tolerance set by the user. Displacement checking minimizes the maximum nodal  $D_{Iteration}$  displacement of an iteration. This is divided by the maximum nodal  $D_{Increment}$  displacement of the interment as seen in Eq. 2.7. It can be noted in Figure 2.2, that upon converging the displacement of an iteration decreases, thus the solution occurs when the iteration displacement is near zero. As presented, both the resid-

ual and displacement checking are relative convergence criteria. Strain energy checking is similar to displacement checking, but instead of displacements the global strain energy is minimized. Marc allows for the combination of residual checking and displacement checking, but not strain energy checking. It is assumed that two convergence criteria is better than one, so all Marc non-linear FE analyses in this thesis were performed utilizing residual and displacement checking with a maximum tolerance of 0.001.

$$\frac{\max(|F_{Residual}|)}{\max(|F_{Reaction}|)} < \text{Tolerance} \quad (2.6)$$

$$\frac{\max(|D_{Iteration}|)}{\max(|D_{Increment}|)} < \text{Tolerance} \quad (2.7)$$

Alternatively a modified Newton-Raphson method can be used to solve non-linear FE analyses in Marc. The modified Newton-Raphson method is similar to the Newton-Raphson method. However, the stiffness matrix is not recalculated every iteration with the modified Newton-Raphson method, and instead the initial stiffness matrix of an increment is used for each iteration. The result is that iterations can be performed rapidly as the stiffness matrix does not require assembly each iteration, however the approach requires much more iterations. The modified Newton-Rapshson method is effective for large scale problems, nonetheless MSC Marc (2014) advises to avoid using the modified Newton-Raphson method with highly non-linear problems. In order for a for a highly non-linear problem to converge, the reassembly of the stiffness matrix cannot be avoided. The FE models presented in this thesis all use a realtively small number of elements, so all non-linear FE models in this thesis were run with the full Newton-Raphson method.

It is important to mention that both the Newton-Raphson and the modified Newton-Raphson methods are not guaranteed to converge as stated by Cook *et al.* (2002). However it is expected that with continued iteration both the residual force and displacement of an iteration are to approach zero. Additionally it is recommended that small load steps are taken to get an accurate representation of the non-linear load displacement relationship.

## 2.6 Digital Image Correlation

Digital Image Correlation (DIC) is a tool used to compute the displacement values of a specimen from a sequence of images (LaVision GmbH, 2015). The DIC system is used to capture images as a test specimen deforms. Each image is split into subsets of  $N \times N$  pixels. A unique contrast pattern is present in each individual subset. The least squares method and iterative optimization is used to fit linear transformations to the contrast pattern of subsequent images, which will result in a subset deformation when the subset changes shape and

location. This is repeated across the entire image to obtain the full field displacement data. Specimens are often covered with a random speckle paint pattern in an effort to increase the unique contrast in each subset. A sample speckle pattern can be seen in Figure 2.3.

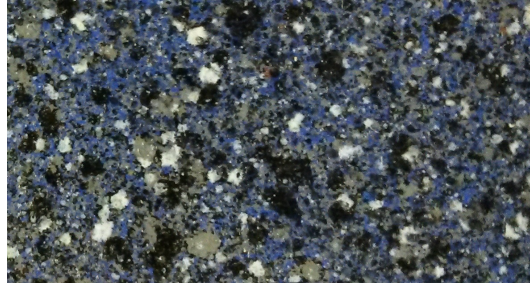


**Figure 2.3:** Random paint speckle pattern on PVC-coated polyester

The DIC system used in the work presented by this thesis is a product of LaVision GmbH. The StrainMaster Portable DIC hardware was used with two VC-Imager E-lite 5 megapixel cameras (LaVision GmbH, 2014*b*), and seen in Figure 2.4. This two camera system is capable of full 3D stereoscopic displacement measurements on the surface of a specimen. DaVis software by LaVision GmbH (2014*a*) was used to calculate the displacement fields from images captured by the StrainMaster. The system is calibrated before capturing a sequence of images to ensure sub-pixel accuracy.

The DIC system was used to measure the radius of a steel bearing ball, to understand the three dimensional capabilities of the system. Information on how the radius was determined from the DIC system is presented in Appendix A. The DIC determined radius of the ball was accurate, with an average percent error of 0.42. This suggest that the DIC can accurately determine data points on a surface of a curved object.

## 2.7 Inflatable Beam Bending

Experimental testing on inflatable beams has been an important process in the validation of many numerical models. Without validation, the ability of the numerical model to replicate the physical behavior is largely unknown. This section discusses the various experimental setups, numerical models, and results of inflated beam testing in literature.

A shear-moment mathematical model was used to predict the load displacement behavior of cantilever beams by Main *et al.* (1994). Main *et al.* performed physical testing on the inflatable cantilever beams to validate the model. Four different cylinders were made from rip-stop nylon with various length/diameter ratios between 2.5 and 18. With a typical cantilever beam,



**Figure 2.4:** Two camera StrainMaster Portable by LaVision GmbH

the base is kept rigid while a tip load is applied and the deflection of the tip is measured. For an inflatable cylindrical beam undergoing cantilever bending, Main *et al.* discovered that a large portion of the tip load is carried by the tensile strength of the material. This tensile load, along with changes in the moment of inertia due to wrinkling, lead to a poor correlation of the experimental test data and the shear-moment model. Main *et al.* created a specialized test fixture to minimize the tensile load by keeping the beam approximately perpendicular to the tip load by rotating the base. Tests conducted utilizing this fixture correlated better with the shear-moment model at the lower test pressure of 34,475 Pa than the higher pressure of 68,950 Pa. The poor correlation at higher pressures was believed to be contributed to the non-linear response of the nylon material.

Inflatable fabric panels were tested in a three point bending configuration by Wielgosz and Thomas (2002). The panels were constructed with two parallel coated woven fabrics connected by polyester yarns. When inflated the coated fabric on the panel would remain flat, resembling a rectangular cross section when inflated. The three point bending tests applied a lengthwise center load to the inflated panel, while the ends of the panel were supported. Timoshenko's beam theory was used instead of Bernoulli's beam theory to derive a mathematical model of the panel behavior, because shear stress cannot be neglected for the inflatable structure. The theoretical and experimental load displacement values showed strong correlation at all pressures, suggesting that the derived mathematical model was capable of accurately predicting the

load response of the beam for a variety of load conditions.

Inflatable cylinders made of Vectran and polyethylene naphthalate were investigated by Cavallaro *et al.* (2003). Four point bending was chosen over a three point bending configuration. A greater load state can be achieved utilizing four point bending as opposed to three point bending, because a lesser load occurs at each support reducing the effects of localized wrinkling of the inflatable beam. The four point bending tests were conducted using a displacement controlled Instron® machine. The load of was recorded with the Instron's load cell, while the center displacement of the beam was recorded with a displacement wire transducer. It was observed that the shear deformation, which was largely influenced by the inflation pressure of the beam, dominated the stiffness of the inflatable air beam. A non-linear FE model was constructed of the cylinders utilizing shell elements with an orthotropic material model. The results of the FE analysis matched poorly with experimental tests because of the non-linearity of the material. The effective shear moduli decreased on the compression side while increasing on the tension side of the inflatable beam. It was concluded that the pressurized cylinder structures differ fundamentally from conventional structures of metal and fiber composites, largely because the material did not behave as a continuum.

Three point bending tests were conducted on inflatable cylinders made from coated textiles by Thomas and Wielgosz (2004). Simple supports were made from PVC cylinders fit to the diameter of the inflatable tube, which were free to rotate on a ball bearing. The displacement of the beam was measured using a camera. The cylinder's cross section didn't remain orthogonal to the neutral axis during bending, which demonstrated the influence of the material's shear response while the inflatable beam experienced bending. Timoshenko's beam theory was used to derive a mathematical model of the inflatable cylinder. However, the theoretical model did not match as well with the experimental results as matched by the previous work on inflatable panels by Wielgosz and Thomas (2002). A new inflatable cylindrical beam FE was derived that utilized a non-symmetric stiffness matrix. The FE analysis with the purposed element matched the experimental results better than the theoretical model based on Timoshenko's beam theory, however it produced a bending shape that was more non-symmetric than the experimental data.

Three point and four point bending were performed on inflatable fabric cylinders woven into a circular cross section by Davids *et al.* (2007). An Instron® hydraulic actuator with nylon straps were used to apply and measure the load on the beam. Wire transducers were used to measure the displacement in the center of the beam as well as two additional locations along each half of the beam. Utilizing virtual work principles and Timoshenko beam theory, a new discrete inflatable cylindrical beam element was derived. The FE analyses utilizing this new element formulation matched well with the experimental results in both three and four point bending at different pressures. While the performance of the derived beam element was impressive, it can only be used

in the analysis of inflatable fabric tubes.

Cantilever, three point, and four point bending, are all popular methods of testing inflatable beams; the cantilever beam being the most difficult to test as the support and loads require a large amount of consideration. Both optical tools and wire transducers have been used to measure the deflections of the beam with success. Traditional Bernoulli beam theory cannot be used to model the load deflection response of the inflatable beams, because the theory ignores the material's shear response. It has been shown that the shear stress of an inflatable beam is a significant contribution to the stiffness of the beam. Timoshenko beam theory has been used with mixed results to create mathematical models of bending inflatable beams. Specialized inflatable beam elements, such as the element derived by Davids *et al.* (2007), have been used to model the bending of an inflatable beam with success. However these elements are specific to a particular geometry, and cannot be used to directly model other inflatable structures. Using shell elements to model the bending of an inflatable cylinder was explained to be difficult by Cavallaro *et al.* (2003). This was due to the non-linear behavior of the inflatable beam, which originated from the non-linear material properties. The benefit of successfully modeling the bending of inflatable cylinders with shell elements in the FE method, is that shell elements can be used to model additional structures. Despite the success of the specialized inflatable beam elements, the process used to derive the element formulation is only applicable for beams.

# Chapter 3

## Non-Linear Orthotropic Material Model from Uniaxial Tests

Three uniaxial tests were conducted on PVC-coated polyester in the material warp, fill, and 45° bias directions. Utilizing Digital Image Correlation (DIC), virtual strain gauges are used to determine the strain of the specimens. Finite element (FE) models were constructed replicating the physical behavior of the uniaxial tests. Optimization was used to obtain the material model that matches the load deformation behavior of the virtual strain gauge. A non-linear orthotropic material model was determined.

### 3.1 Experimental Tests

Uniaxial tests were performed following the ASTM D751 - 06 (2011) cut strip test method on a MTS Criterion® 44. The MTS test system is capable of pulling the clamp at a uniform speed of 1020 mm/min, which exceeds the ASTM D751 testing speed of 300 mm/min. A MTS LPS.304 low profile shear beam force transducer was mounted to the MTS load frame, which has a force rating of 30 kN. The LPS.304 determines the uniaxial load with high fidelity as the transducer is rated with an accuracy class of 0.5 percent from 300 N to 30,000 N. This force transducer exceeds the ASTM D751 machine efficiency requirement by having an error less than one percent for its loading range. Test specimens are prepared to be 25 mm in width and 175 mm in length. Clamps 30 mm wide are used to hold the specimens sufficiently flat and parallel during the test. The distance between the clamps at the start of the test is 75 mm as prescribed by the ASTM D751 standard. The uniaxial tests are performed with DIC to measure the displacements on the specimens surface.

Uniaxial tests were performed in the warp, fill, and 45° bias yarn directions of the PVC-coated polyester. The 45° bias test has been used to provide insight on the material's shear response. For each material yarn direction, five uniaxial tests were performed. The resulting load and maximum DIC dis-

placement value from all uniaxial tests are presented in Figure 3.1. A fourth order polynomial was fit to the data points of each uniaxial test direction. The close grouping of data points for a particular material direction suggests that the tests produced a consistent load displacement curve. Each uniaxial specimen was pulled until the sample broke. While each test direction failed above 1000 N, the 45° bias yarn direction exhibited considerably larger displacements than the warp or fill direction.

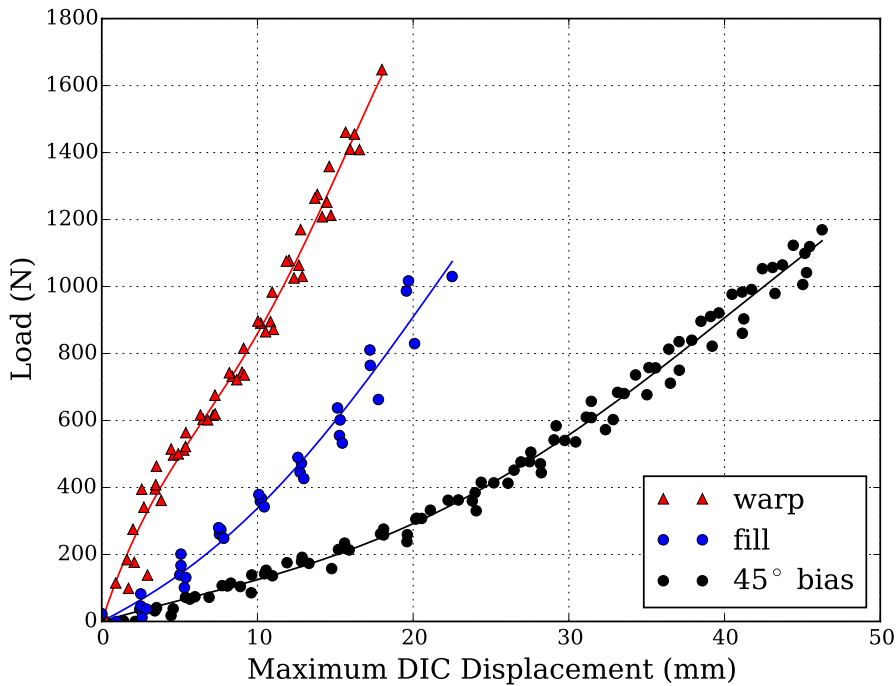


**Figure 3.1:** Fitted polynomials through the load displacement values for five tests in each material direction

There is a lack of data points above 700 N in the fill direction, despite each uniaxial test failing above 1000 N. This is because the DIC failed to correlate displacements on the specimen for a couple of the tests in the fill direction. When this happens the DIC loses a significant portion of the data points on the surface of the specimen. While the lack of displacements at a high load value may appear to be problematic, the test data showed a strong correlation before this point. Thus it is safe to assume that had the DIC been able to capture displacements at a load above 700 N for each sample in the fill direction, the additional data points would be similar to the existing data set.

The maximum DIC displacement value is a poor measurement. The maximum DIC displacement value of a uniaxial test does not incorporate a correction if the material slips. For instance the maximum DIC value may be larger

CHAPTER 3. NON-LINEAR ORTHOTROPIC MATERIAL MODEL FROM  
22 UNIAXIAL TESTS

for a particular test in which the material slipped than in a test in which the material did not slip. Material slip is evident in some of the images captured by the DIC, as seen in Figure 3.2. Despite inconsistent material slip, the tests shown in Figure 3.1 produce a similar load displacement relationship. A more accurate displacement measurement is required, because the images from the uniaxial tests indicated that the material slipped at the test grips.

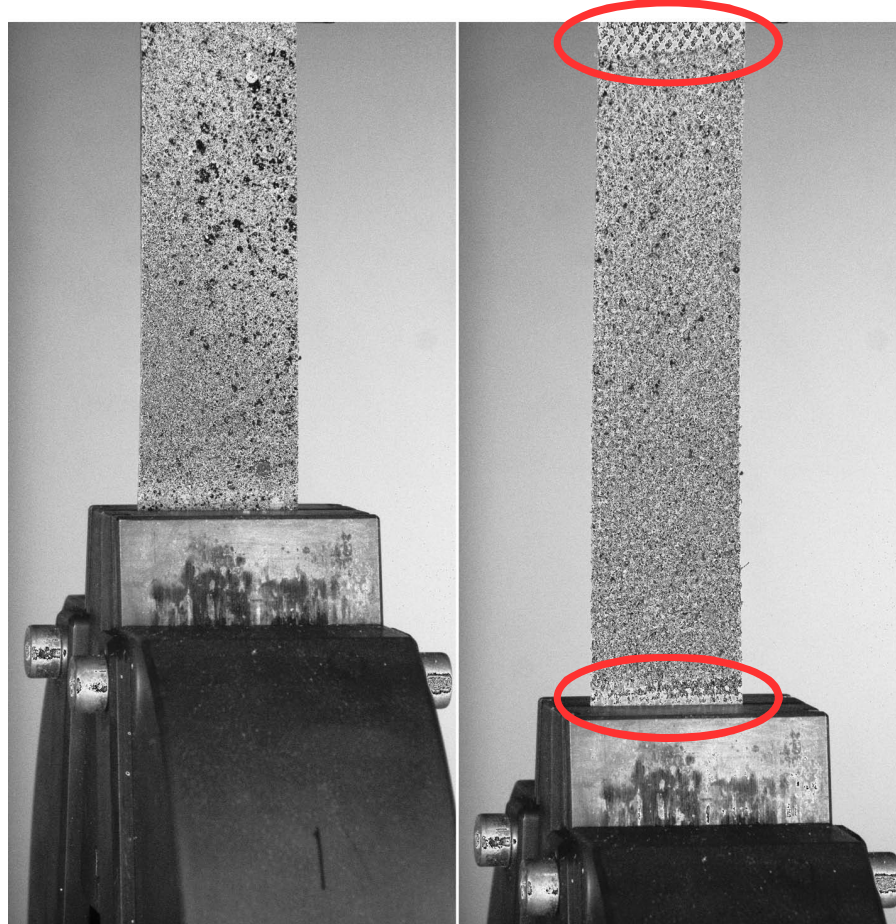


**Figure 3.2:** Contrast DIC images of uniaxial specimen in the material fill direction with circles highlighting evidence of material slip in the deformed state

### 3.2 Virtual Strain Gauge

The DIC generates points on the surface of an uniaxial specimen in three dimensions. A virtual strain gauge is created by tracking the displacement between two points on the surface of the uniaxial specimen. The initial distance

represents a length of a line. As the specimen deforms from the uniaxial test, the length of the line increases. The virtual strain gauge provides a displacement value that is relative to a point on the surface of the specimen, while the maximum DIC displacement value would be relative to the initial configuration. Slip from the test grips does not interfere with the displacements of the virtual strain gauge, because the displacement measurement is relative to a point on the surface of the material and not the test system.

An initial and deformed uniaxial test of the material fill direction can be seen in Figure 3.3, with a virtual strain gauge plotted on the specimen's surface. The blue patch is a correlation map in a mask on the surface of a uniaxial specimen. The virtual strain gauge is represented by the green line which tracks the displacement on the specimen's surface between the end points of the line. The top point of the line can be seen moving down due to the material slipping. The specimen is shown in the  $xy$  plane, but the displacement of the virtual strain gauge is calculated using the full  $x$ ,  $y$ , and  $z$  coordinates. It can be noted that the specimen data points do not make a perfect rectangle despite the uniaxial test samples being rectangular. The missing specimen data points are the result of the DIC failing to find a correlation. Additional data points may be lost on the specimen as the specimen deforms, because areas on the specimen may not resemble the initial state while deforming. Overall an accurate displacement value for the uniaxial tests that accounts for material slip can be determined by the virtual strain gauge.

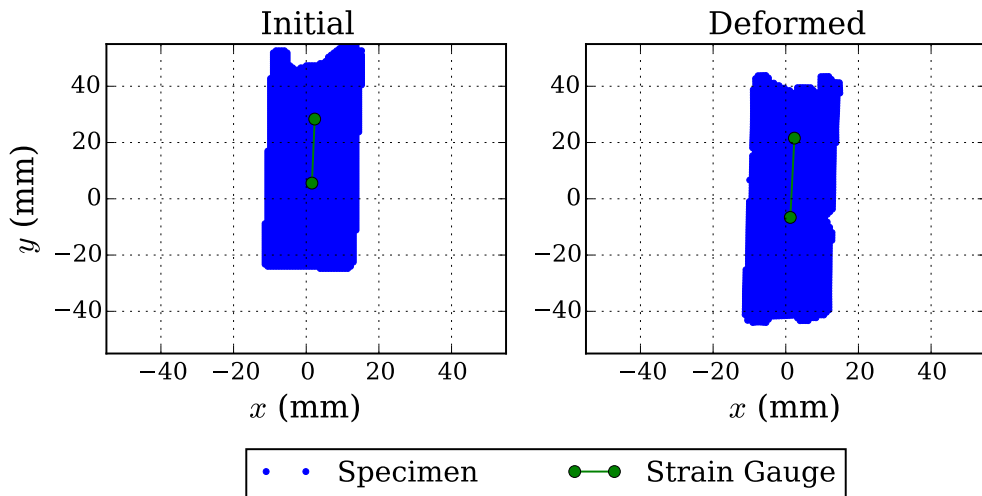


**Figure 3.3:** Virtual strain gauge on the initial and deformed uniaxial specimen in the material fill direction where the blue is an overlay of the masked region on the uniaxial sample

The DaVis software by LaVision GmbH (2014a) includes a virtual strain gauge feature. In the graphical user interface of DaVis, a user may click on

**CHAPTER 3. NON-LINEAR ORTHOTROPIC MATERIAL MODEL FROM  
24 UNIAXIAL TESTS**

two points in an image captured by the DIC to create a virtual strain gauge. However, it is very difficult to ensure that the selected two points create a line parallel to the specimen. A better implementation of the virtual strain gauge would allow for the user to specify the coordinates of the points to create a virtual strain gauge on the initial image. A Python script was created specifically for creating virtual strain gauges on exported displacement field data from DaVis. The script calculates the length between two points specified on the sample throughout the test. The Python script produced strain values analogous to the DaVis software, with the added benefit of being able to explicitly control the strain gauge points. All strain gauge values presented were obtained using this Python script.

Virtual strain gauges of similar length were placed approximately in the center of the test specimens in the warp, fill, and 45° bias direction. The displacements of the strain gauges were calculated using a strain gauge of the exact same length, for a given material direction. The load strain gauge displacement relationships can be seen in Figure 3.4. A polynomial, represented by the solid line, was fit to the test data in each material direction using the least squares method. These polynomials were used to characterize the uniaxial non-linear orthotropic material model. It was assumed that the polynomials were an accurate representation of the uniaxial tests, because the polynomials go through the center of each data set.

**Table 3.1:** Virtual strain gauge values including: initial length  $l_i$ , final length  $l_f$ , maximum engineering strain  $\varepsilon$  (mm/mm), and coefficient of determination  $R^2$  of the fitted polynomial

| Direction | $l_i$ (mm) | $l_f$ (mm) | max $\varepsilon$ | $R^2$ |
|-----------|------------|------------|-------------------|-------|
| warp      | 20.022     | 23.329     | 0.165             | 0.998 |
| fill      | 22.780     | 28.721     | 0.261             | 0.959 |
| 45° bias  | 19.767     | 30.734     | 0.555             | 0.987 |

In order to characterize the uniaxial non-linear orthotropic material model, the load virtual strain gauge data will need to be compared to FE models often. It is easier for the FE models to compare the load virtual strain gauge displacements when using a polynomial to describe the relationship, rather than interpolating between the data points. This is one reason why a fourth order polynomial was fitted to the load strain gauge displacement for each material direction. The polynomial is represented by the sold lines in Figure 3.4. The coefficient of determination of the fitted polynomials, length details, and engineering strain of the virtual strain gauges are all provided in Table 3.1. The lowest  $R^2$  value of the fourth order polynomials fitted to the load strain gauge displacement data was 0.959, indicating that each polynomial is an excellent fit to the virtual strain gauge data. It is safe to use the polynomials instead of

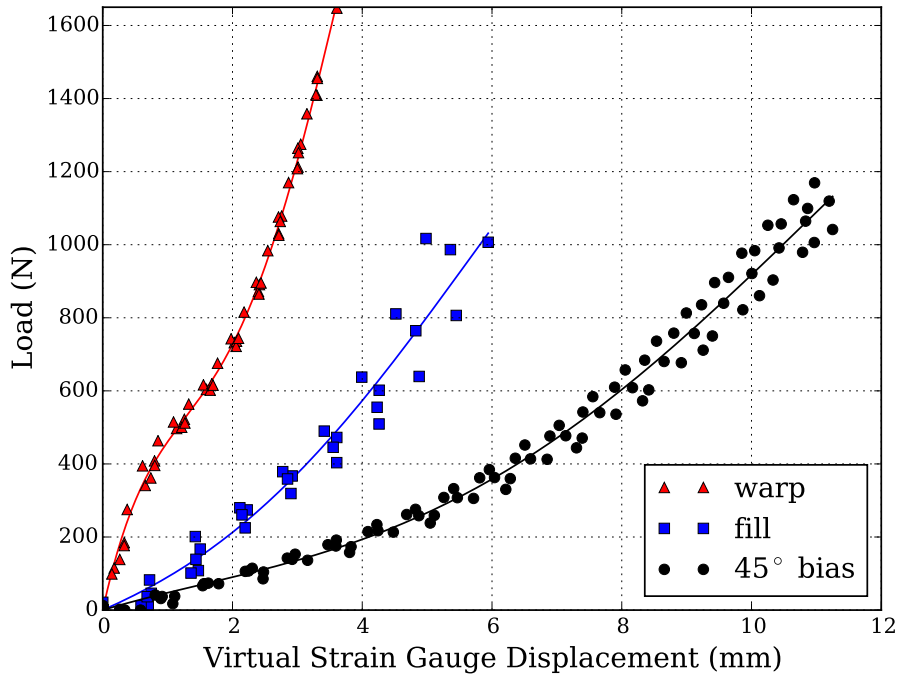


**Figure 3.4:** Load strain gauge displacement values for the uniaxial tests in the Warp, Fill, and  $45^\circ$  bias material directions with fitted polynomial indicated by the solid line

the load strain gauge displacement data points because of the superb fit of the polynomial. Working with the polynomial is preferred over the data points, because the polynomial can be evaluated anywhere in the displacement range, so no interpolation is needed between displacement data points.

Polynomial fits were chosen to have the lowest root mean square error and highest coefficient of determination. Fits with different order polynomials were attempted, and it was determined that the fourth order polynomials were the best fit. It can be noted that the fill and bias directions can be simplified to third order polynomials, with little change in the quality of fit. The polynomials were forced through the origin, however this wouldn't be required for the later described inverse analysis. This is because it isn't expected that the numerical models match the polynomials exactly, but rather that the polynomials serve as a tool in the matching of the numerical models to the experimental test results.

It was attempted to obtain Poisson's ratio by creating an additional strain gauge perpendicular to the described strain gauge on the uniaxial warp specimen, however the results were not successful. The Poisson's ratio found was near to zero, which would indicate that the fiber directions were decoupled. This decoupled behavior in the warp test is different than the deformation

**CHAPTER 3. NON-LINEAR ORTHOTROPIC MATERIAL MODEL FROM  
26 UNIAXIAL TESTS**

experienced in the bias extension test. In addition, it was found that the Poisson's ratio changes as the specimen deformed. While Poisson's ratio is an interesting topic for future study, the investigation was not critical to this work. Instead of obtaining Poisson's ratio from the tests, a Poisson's ratio from literature was used.

### **3.3 Uniaxial Finite Element Models**

Three non-linear FE models were created in MSC Marc to replicate the three distinct uniaxial tests in the warp, fill, and 45° bias material direction. Symmetry is utilized to simplify the uniaxial FE models in the warp and fill directions. However, the uniaxial 45° bias test cannot use symmetry as the test produced an unsymmetrical displacement field. A non-linear orthotropic material model is used to replicate the non-linear behavior of the uniaxial tests. The material model will be determined through optimization, by minimizing the load displacement difference of the FE models and the virtual strain gauges from the physical tests.

The uniaxial tests in the warp and fill material directions can be modeled with shell elements. In both material directions, the displacements of the uniaxial specimens were symmetric about the long axis of the uniaxial specimen. The symmetry greatly simplifies the FE model as any line parallel to the edge of the test grips, in the initial configuration, would remain parallel throughout the test. Thus a representative FE model only needs to include the area of the virtual strain gauge. The mesh used for the warp uniaxial test is seen in Figure 3.5, while a similar mesh is used in the fill direction. Both meshes use 40 linear quad elements. The width of the mesh is one half the width of the 25 mm wide specimen, because of symmetry. The warp mesh has the material primary direction aligned with the y axis, while the fill mesh has the material secondary direction aligned with the y axis. For both the warp and fill models, the length of the mesh matches exactly with the initial length of the virtual strain gauge in the corresponding material direction. Roller constraints are used on the top and symmetric line of the mesh. A displacement in the *y* direction is applied to the nodes on the bottom edge of the mesh, such that the final deformed mesh will have the length of the final deformed strain gauge as referenced in Table 3.1. The load extracted from the FE models in the warp and fill direction will need to be doubled before comparing the FE results to the physical tests, because the FE models only model half of the uniaxial specimen's width.

The entire 45° bias uniaxial test needs to modeled in the FE software since the test specimen was not symmetric. The geometry of the 45° bias uniaxial test was modeled with 300 linear quad elements between the test grips. The resulting mesh is 25 mm in width and 75 mm in length, which is the same size as the prepared uniaxial specimen between the test grips. Appropriate care

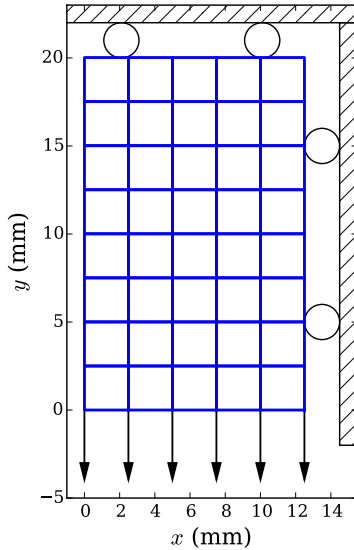


**Figure 3.5:** Symmetric FE mesh of the warp uniaxial test with boundary conditions

was used when generating the mesh, such that in the center of the mesh two nodes match the initial length of the virtual strain gauge. The virtual strain gauge location on the mesh can be seen by the two green dots in the center of Figure 3.6. The displacements of the nodes representing the virtual strain gauge on the FE model are exported by a simple script, which calculates the overall displacement of the strain gauge on the FE model. The displacement values of the virtual strain gauge of the FE model is compared directly with the displacement of virtual strain gauge in the physical  $45^\circ$  bias tests. The elements of the mesh are oriented such that the primary direction is  $45^\circ$  from the  $y$  axis. The nodes on the top of the mesh are fixed to simulate the physical clamping condition. A fixed displacement is applied to the nodes on the bottom of the mesh, such that in the  $y$  direction the model will displace similar to that of the lower jaw in the physical test while not allowing any displacement in the  $x$  direction.

MSC Marc (2014) includes a material model, the NLELAST model definition, capable of creating a simplified non-linear elastic orthotropic material model. The non-linear orthotropic material model is capable of reproducing the non-linear load displacement curves of the uniaxial tests. The Young's moduli ( $E_1$ ,  $E_2$ ), Poisson's ratio ( $\nu_{12}$ ), and shear modulus ( $G_{12}$ ) can be defined as functions of the strain component in their respective direction. A Poisson's ratio of 0.24 was used, which is similar to the Poisson's ratio used for various PVC-coated polyesters by Galliot and Luchsinger (2009) in a standard linear orthotropic model. To add complexity to the inverse bubble inflation test, which is discussed later, third order polynomials are chosen for each of the moduli as seen in Eqs. 3.1 - 3.3. The stress output of such a model may be non-sensible as the model may violate the constitutive relationships of traditional

**CHAPTER 3. NON-LINEAR ORTHOTROPIC MATERIAL MODEL FROM  
28 UNIAXIAL TESTS**

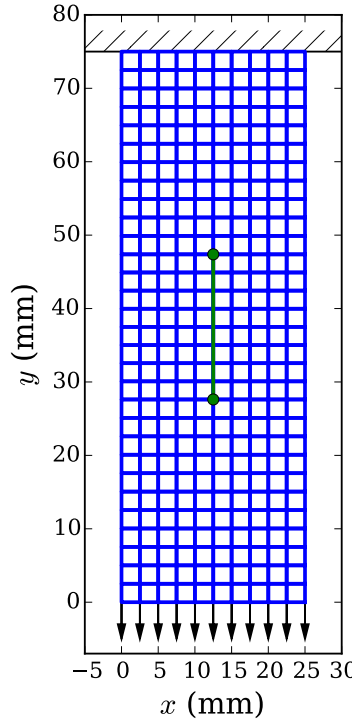


**Figure 3.6:**  $45^\circ$  bias uniaxial test FE mesh with boundary conditions and virtual strain gauge indicated by the green dots in the center of the mesh

FE theory. However such material models may still be useful in the design and analysis of structures, by accurately predicting the load displacement behavior. The best non-linear orthotropic material model will be determined by matching the load displacement behavior of the virtual strain gauges of the FE models to the physical uniaxial tests.

$$G_{12}(\gamma_{12}) = \beta_0\gamma_{12}^3 + \beta_1\gamma_{12}^2 + \beta_2\gamma_{12} + \beta_3 \quad (3.1)$$

$$E_2(\varepsilon_2) = \beta_4\varepsilon_2^3 + \beta_5\varepsilon_2^2 + \beta_6\varepsilon_2 + \beta_7 \quad (3.2)$$

$$E_1(\varepsilon_1) = \beta_8\varepsilon_1^3 + \beta_9\varepsilon_1^2 + \beta_{10}\varepsilon_1 + \beta_{11} \quad (3.3)$$

All three FE models use a constant time step, such that 100 increments produces a maximum displacement analogous to the physical test. The residual force and relative displacement tolerance was set to 0.001. All shell elements have a constant thickness of 0.81 mm, representing the thickness of the material. The  $\beta$  terms of the non-linear orthotropic material model will be determined with optimization, such that the material model parameters in the FE models match the load displacement behavior of the virtual strain gauges seen in Figure 3.4.

## 3.4 Optimization of FE Models

Optimization is used to determine the best non-linear orthotropic material model by minimizing the difference between the physical uniaxial tests and the FE models. The uniaxial FE models are considered simultaneously to compute a single error value that describes the fit of the FE models to the virtual strain gauge test results. Design Optimization Tools (DOT) in company with a Python script is used to run the FE models and determine the optimum material parameters.

Root mean square error (RMS) is used to determine the error between the FE model and the physical tests. The polynomials fitted to the load displacement virtual strain gauge data from the physical uniaxial tests are represented by  $P_{warp}$ ,  $P_{fill}$ , and  $P_{bias}$ . At each of the 100 increments of the FE model, the load extracted from the FE model is represented by  $F_{warp}$ ,  $F_{fill}$ , and  $F_{bias}$ . The load from the polynomials is compared directly with the load of the FE model at the 100 FE increments. Three RMS errors are calculated for each material direction, and can be seen in Eqs. 3.4 - 3.6.

$$e_{warp} = \sqrt{\frac{\sum_{i=1}^{100} (F_{warp}(i) - P_{warp}(i))^2}{100}} \quad (3.4)$$

$$e_{fill} = \sqrt{\frac{\sum_{i=1}^{100} (F_{fill}(i) - P_{fill}(i))^2}{100}} \quad (3.5)$$

$$e_{bias} = \sqrt{\frac{\sum_{i=1}^{100} (F_{bias}(i) - P_{bias}(i))^2}{100}} \quad (3.6)$$

The three RMS errors can be combined into a single error value  $e_{uniaxial}$ . It is possible to create the single error value by simply adding up the RMS of each material direction, as seen in Eq. 3.7. Each material direction terminates at a load of the same order of magnitude, as seen in Figure 3.4, so there is no need to normalize the RMS of each individual direction. Additionally there is no weight to a particular material direction as the optimization goal is to find the best overall material model. A  $e_{uniaxial}$  value of 0.0 represents a non-linear orthotropic material model in which the uniaxial FE models match exactly with the experimental uniaxial tests.

$$e_{uniaxial} = e_{warp} + e_{fill} + e_{bias} \quad (3.7)$$

The overall objective function of the optimization can be expressed by minimizing the overall error of the FE models load displacement results for a

**CHAPTER 3. NON-LINEAR ORTHOTROPIC MATERIAL MODEL FROM  
30 UNIAXIAL TESTS**

particular material model. The ideal material model will match the uniaxial virtual strain gauge load displacement results exactly. This is subjected to two constraints, the first being that the moduli in the material model must remain positive for the entire strain range because a negative moduli for a positive strain is non-sensible. The second being that all of the FE analyses are valid, in which case Marc outputs an exit code for each analysis of 3004. The overall objective function can be seen in Eq. 3.8. The two constraints serve as logical flags for the constrained optimization. When a constraint is violated, a value of 1 is fed into the algorithm, while a value of -1 indicates a satisfied constraint. This type of true-false boolean constraint may be problematic for a gradient based optimization algorithm, however DOT deals with boolean constraints well by backtracking when encountering a violated constraint in the one dimensional search. It is important to mention that DOT's approach works well, provided that the optimization is started from a feasible point.

$$\begin{aligned} & \text{minimize: } e_{\text{uniaxial}} \\ & \text{such that: } E_1, E_2, G_{12} > 0 \quad \text{and} \\ & \quad \text{All Marc Exit Codes} = 3004 \end{aligned} \tag{3.8}$$

The  $\beta$  terms of Eqs. 3.1 - 3.3 are the variables the optimizer will use to determine the best non-linear orthotropic material model, however what determines a reasonable starting point and defines the variable bounds is unknown. An initial optimization was performed on  $\beta$  terms that began in the feasible region to satisfy the boolean constraints. From this optimization, a material model was created that matched well with the uniaxial test data. The DOT parameters were used in their default configuration, including gradient step size, scaling, and convergence criteria. The Modified Method of Feasible Directions (MMFD) algorithm proved to be the most reliable gradient based optimization algorithm from the DOT library for the inverse problems considered here. The optimization is run from multiple starting points to ensure the best material model is found, and to avoid selecting a local minimum in the design space as the best material model. The best material model can be described mathematically as having the lowest objective function value.

### 3.5 Material Models

Material model parameters were determined through optimization, by minimizing the difference of the virtual strain gauge load displacement curves and the uniaxial FE models. The optimization did not find material model parameters that would lead to a perfect fit of the uniaxial strain gauge data. However, a material model that resembles the strain gauge load displacement behavior was found, with an objective value of 50.1. The optimization was

not deemed too computational intensive, and multiple optimizations could be performed in a day on a desktop PC.

The resulting non-linear orthotropic material model matched well with the physical test data. The load displacement data from the FE models with the determined material model can be seen in Figure 3.7 on top of the fitted polynomials to the virtual strain gauge load displacement physical data. It can be noted that the fit in the warp material direction is superior to the other two directions. The material model struggled to create the low stiffness experienced by small strains in the fill direction.

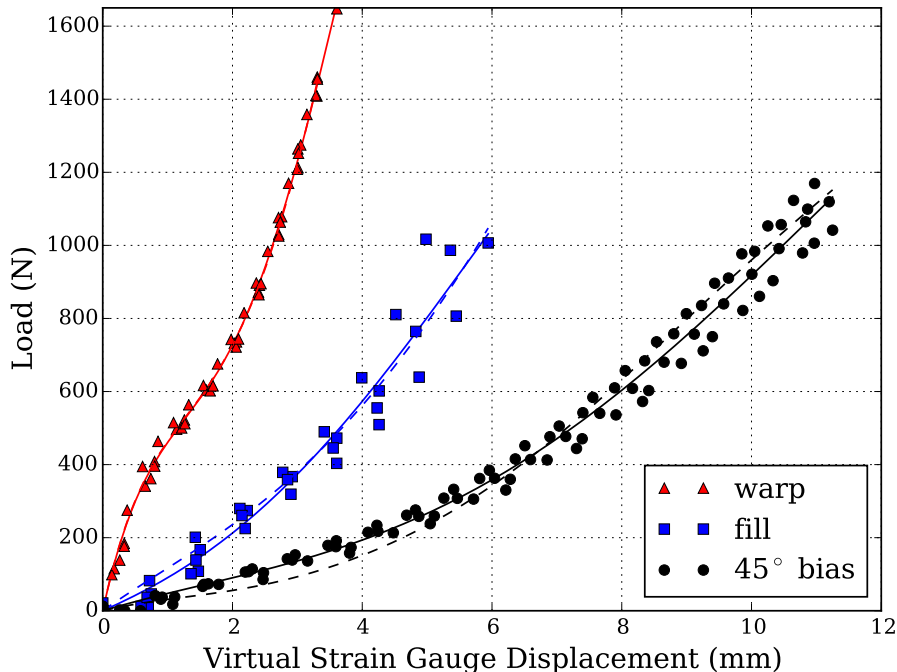


**Figure 3.7:** Load displacement result of the non-linear orthotropic FE models (dashed line) on top of the polynomial fitted to the virtual strain gauge data (solid line)

A plot of the three moduli determined from the optimization can be seen in Figure 3.8. The moduli are limited to the maximum strain  $\varepsilon$  value of the physical uniaxial test. It can be seen that the magnitude and non-linearity of  $E_1$  dominates the other moduli. Additionally it can be noted that the moduli curves do not represent a third order polynomial. This suggest that the third order polynomials may be simplified. A lower order simplification does not guarantee better material fits, as in Figure 3.7, so second order material models were not explored since the existing fit was of acceptable quality. It is important to mention that simplifying the polynomial order of the non-linear

CHAPTER 3. NON-LINEAR ORTHOTROPIC MATERIAL MODEL FROM  
32 UNIAXIAL TESTS

orthotropic material model parameters greatly reduces the computational cost of determining the material model parameters. The resulting  $\beta$  values, of Eqs. 3.1 - 3.3, that define the material model can be seen in Table 3.2.

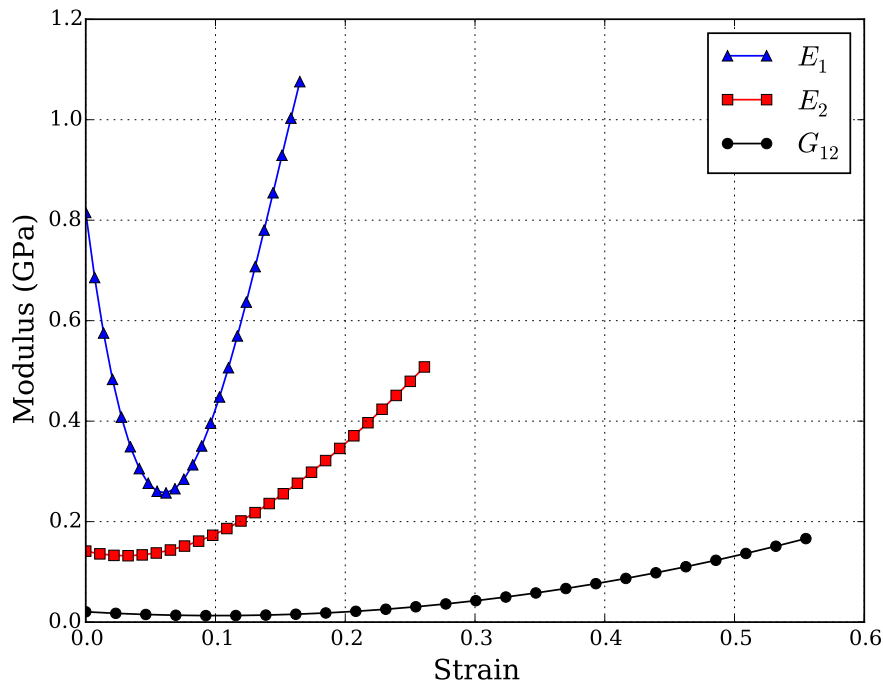


**Figure 3.8:** Non-linear orthotropic material model determined from the simultaneous optimization of the three FE models, where each modulus is limited to the failure strain

**Table 3.2:** Variables determined from the optimization of the uniaxial test cases that define the non-linear orthotropic material model of Eqs. 3.1 - 3.3

| Solution     |                           |
|--------------|---------------------------|
| $\beta_0$    | $-7.96599 \times 10^{-3}$ |
| $\beta_1$    | $7.49311 \times 10^{-1}$  |
| $\beta_2$    | $-1.50931 \times 10^{-1}$ |
| $\beta_3$    | $2.05148 \times 10^{-2}$  |
| $\beta_4$    | $-1.13743 \times 10^1$    |
| $\beta_5$    | $1.07160 \times 10^1$     |
| $\beta_6$    | $-6.17621 \times 10^{-1}$ |
| $\beta_7$    | $1.41287 \times 10^{-1}$  |
| $\beta_8$    | $-4.78030 \times 10^2$    |
| $\beta_9$    | $2.11227 \times 10^2$     |
| $\beta_{10}$ | $-2.02600 \times 10^1$    |
| $\beta_{11}$ | $8.15340 \times 10^{-1}$  |

# Chapter 4

## Inverse Bubble Inflation Method

Membrane structures designed with technical woven textiles, coated fabrics, and various polymer membranes are often operated in their non-linear region, thus it is anticipated that the material model should be able to replicate the non-linear behavior of the material. An inverse bubble inflation method may provide an improved method of homogenization for the material, while still accounting for the complex load state of the material. However, a mechanism for obtaining material models utilizing the inverse method with a bubble inflation test has not yet been established. This chapter proposes the procedure for calibrating a non-linear orthotropic material model from an inverse bubble inflation test. The results of a non-linear Finite Element (FE) analysis of a bubble inflation test are used instead of experimental data from a physical bubble test. The non-linear orthotropic material model is used as the solution to the inverse problem. To demonstrate the capability of the inverse bubble inflation test, it is shown that the method can replicate the non-linear orthotropic material model from the solution. This suggests that the inverse bubble inflation test can successfully determine a non-linear orthotropic material model from a bubble inflation test. The inverse bubble inflation technique is then ready to determine the non-linear orthotropic material models from experimental bubble inflation tests.

This chapter proposes the use of an inverse bubble inflation test for obtaining non-linear material models suitable for the FE method. The procedure for obtaining the material model via the inverse bubble inflation technique is outlined. The results of an FE analysis with a known material model are used as a substitute for the experimental bubble inflation test data. This is done to demonstrate that the method is capable of finding the correct material model parameters. If the material model obtained from the inverse bubble procedure is analogous to the known starting point, it can be concluded that the inverse bubble inflation technique is a valid method of obtaining non-linear material models from physical test data.

## 4.1 Methodology

It is important to understand the effectiveness of the inverse bubble inflation method for an ideal test scenario before attempting the technique on physical test data. A large number of factors may influence the ability of the method to obtain an accurate material model, or otherwise prove the inverse method impractical. To demonstrate the ability of the inverse bubble inflation test to reproduce the material models from a known solution with ideal conditions helps to show that the technique is capable of producing accurate material models. At this point the test method would be suitable for characterizing material models from physical tests.

A non-linear FE model representing the physical response of the bubble test was created using MSC Marc (2014). The model comprises of 800 linear quad elements arranged in a circle that is 200 mm in diameter, as seen in Figure 4.1. The appropriate mesh size was determined by an initial mesh convergence study. Pin constraints are applied around the edge of the circle. A linear pressure ramp of 300 kPa is applied to all of the elements, which represents the load from the inflated medium as a function of time. Upon completion of the FE simulation, the nodal data is exported at pressures of interest for the error calculation.

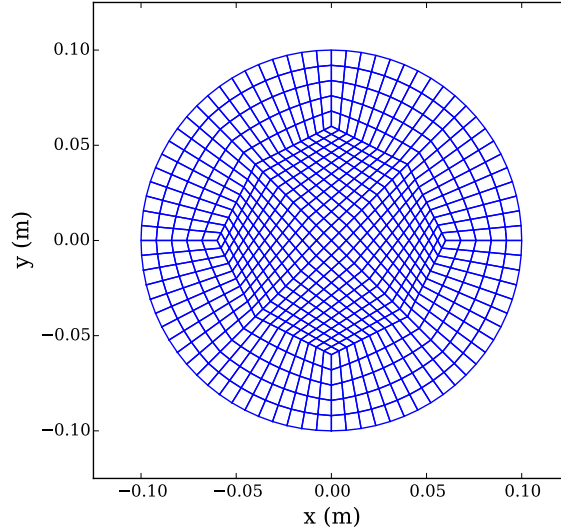


**Figure 4.1:** Mesh used for the bubble inflation FE model

MSC Marc (2014) includes a material model, the NLELAST model definition, capable of creating a simplified non-linear elastic orthotropic material model. The Young's moduli ( $E_1$ ,  $E_2$ ), Poisson's ratio ( $\nu_{12}$ ), and shear modulus ( $G_{12}$ ) can be defined as functions of the strain component in their respective

directions. To add complexity to the inverse bubble inflation test, third order polynomials are chosen for each of the moduli as seen in Eqs. 4.1 - 4.3. Demonstrating the success of the inverse bubble inflation test on this highly non-linear material model suggest that the inverse method may be just as successful with simpler material models.

$$G_{12}(\gamma_{12}) = \beta_0\gamma_{12}^3 + \beta_1\gamma_{12}^2 + \beta_2\gamma_{12} + \beta_3 \quad (4.1)$$

$$E_2(\varepsilon_2) = \beta_4\varepsilon_2^3 + \beta_5\varepsilon_2^2 + \beta_6\varepsilon_2 + \beta_7 \quad (4.2)$$

$$E_1(\varepsilon_1) = \beta_8\varepsilon_1^3 + \beta_9\varepsilon_1^2 + \beta_{10}\varepsilon_1 + \beta_{11} \quad (4.3)$$

A mesh convergence study determined that the 800 element mesh produced acceptable displacement error while having a low computational cost in terms of run time. The mesh size used is largely dependent upon the computational resources available and desired accuracy. Since the optimizer will call the FE model for each function evaluation, reducing the FE model run time greatly reduces the optimization time. To avoid a mesh sensitive optimization result, it is recommended to perform an initial mesh convergence study. The maximum displacement value was within 0.05 percent for mesh sizes of 800 and 800,000 elements.

The sensitivity of the FE model to Poisson's ratio was investigated. The FE bubble inflation model was run with different Poisson's ratios for the same non-linear moduli ( $E_1$ ,  $E_2$ , &  $G_{12}$ ). The resulting maximum displacement values were normalized to the set's average, and can be seen in Figure 4.2 for Poisson's ratios ranging from 0.05 to 0.45. It was observed that for the same non-linear moduli, the Poisson's ratio varied the maximum displacement value by plus or minus three percent. It was determined that the Poisson's ratio was not a significant contribution to the FE bubble inflation model. Thus the Poisson's ratio was held constant, and not included as a variable for optimization.

Vanderplaats Research & Development Inc. (2001) Design Optimization Tools (DOT) was the optimization library used in the inverse method. Gradient based optimization proved to be a sufficient optimization method in demonstrating the effectiveness of the inverse bubble test. The constrained gradient optimization algorithm used was the Modified Method of Feasible Directions (MMFD). A simple Python script interfaces with DOT and the MSC Marc input file of the bubble model. The material model variables ( $\beta_0$  -  $\beta_{11}$  of Eqs. 4.1 - 4.3) are fed into DOT as variables to optimize. The optimization goal is to minimize the error between the FE model bubble displacements and the known displacements. This is subjected to two constraints. The first being that the moduli must remain above zero for the strain range of the material model. The second constraint ensures that the non-linear FE analysis

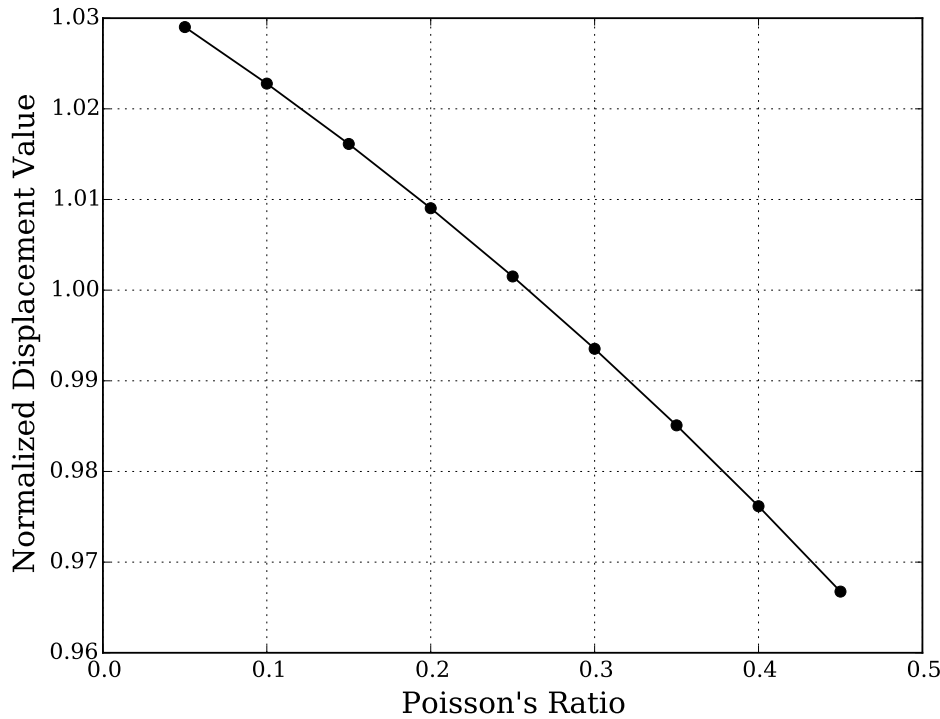


**Figure 4.2:** Normalized maximum displacement value of FE bubble inflation model for various Poisson's ratios

produces a valid exit code, as some set of material model parameters may generate convergence problems. DOT was designed to be useful as an engineering optimizer, so during a one dimensional search the algorithm attempts to stay in the feasible region as much as possible.

## 4.2 Surface Fitting

The non-linear orthotropic material model chosen derives from physical tests on PVC-coated polyester. The  $\beta$  terms in Eqs. 1-3 were fit to the uniaxial test data in the primary, secondary, and  $45^\circ$  bias directions. A plot of the three moduli limited to their strain component can be seen in Figure 4.3. The magnitude and non-linearity of  $E_1$  dominates the other moduli. It can be noted that it is possible to simplify the moduli to a lower order polynomial as the curves do not represent a third order polynomial, but solving the variables of the third order polynomial creates a more complex optimization problem and better demonstrates the effectiveness of the inverse method. A Poisson's ratio of 0.24 was used, which is similar to the Poisson's ratio used for various PVC-coated polyesters by Galliot and Luchsinger (2009) in a standard orthotropic

model. The FE bubble inflation model is run with this material model, simulating a physical bubble inflation test on PVC-coated polyester. Each curve ends at their maximum strain value as experienced by the FE bubble model. The result of the analysis will be used instead of experimental bubble test data to demonstrate the effectiveness of the inverse bubble inflation test.

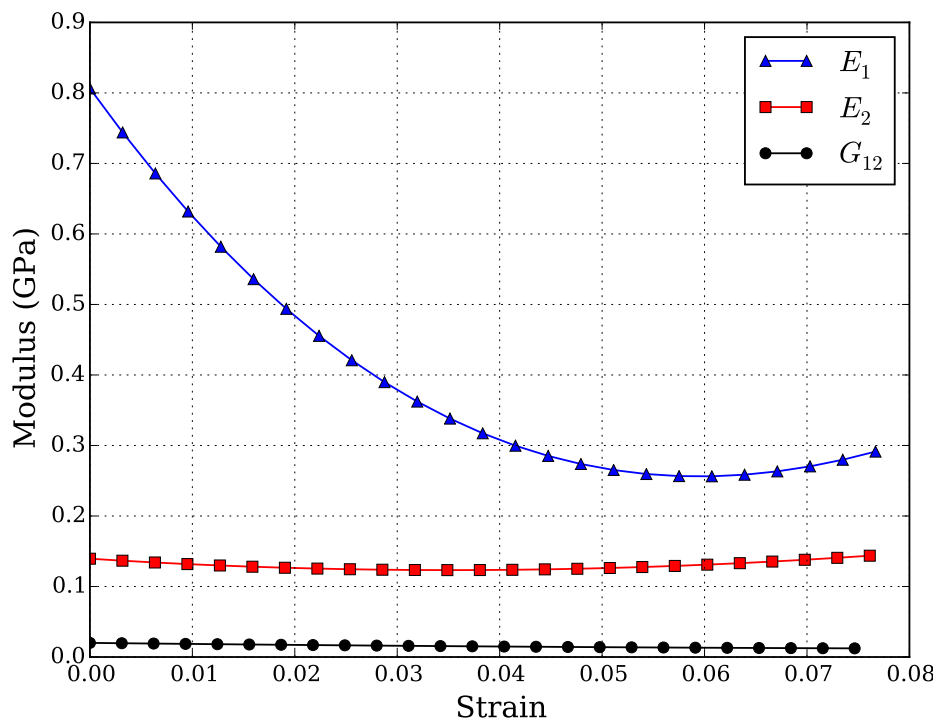
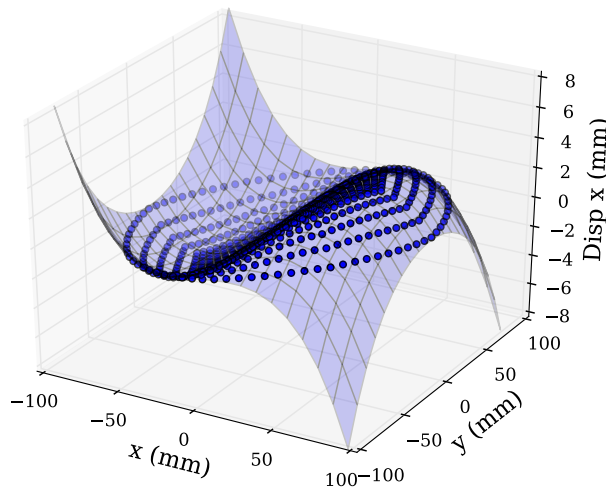


Figure 4.3: Non-linear orthotropic material model moduli as functions of strain

Three separate polynomials are fitted to the nodal displacement values at seven unique pressure instances of the inflating FE model. All of the nodes of the mesh prior to inflation lie in the  $xy$  plane. Thus each node will have a unique displacement value as a function of its original  $xy$  location. The least squares method was used to fit a fourth order polynomial surface to the node locations for the displacement values in the  $x$ ,  $y$ , and  $z$  directions. It was found that a fourth order polynomial, defined by 25 coefficients and shown in Eq. 4.4, to be the best fit. The fitted surfaces along with the nodal displacement values can be seen in Figures 4.4 - 4.6.

$$\begin{aligned}
 F(x, y) = & C_0x^4y^4 + C_1x^3y^4 + C_2x^2y^4 + C_3xy^4 + C_4y^4 + \\
 & C_5x^4y^3 + C_6x^3y^3 + C_7x^2y^3 + C_8xy^3 + C_9y^3 + \\
 & C_{10}x^4y^2 + C_{11}x^3y^2 + C_{12}x^2y^2 + C_{13}xy^2 + C_{14}y^2 + \\
 & C_{15}x^4y + C_{16}x^3y + C_{17}x^2y + C_{18}xy + C_{19}y + \\
 & C_{20}x^4 + C_{21}x^3 + C_{22}x^2 + C_{23}x + C_{24}
 \end{aligned} \quad (4.4)$$



**Figure 4.4:** Nodal displacement  $x$  values on the fitted fourth order polynomial surface at 300 kPa

The entire nodal displacements of the bubble inflation FE model can be represented by a series of polynomials, as a function of the original nodal  $xy$  coordinates, at different inflation pressures. The polynomials are exceptional fits to the nodal  $x$ ,  $y$ , and  $z$  displacements. The coefficient of determination for each polynomial was greater than 0.999 as seen in Table 4.1. A comparison of the fitted displacement  $z$  values from the fitted polynomial and the known displacement  $z$  values is seen in Figure 4.7. The fitted polynomial and known displacement values are nearly identical.

Utilizing polynomials to represent the FE model adds simplicity to the inverse method. Only the coefficients of the polynomials need to be stored, as opposed to the entire nodal displacement values. The error formulation minimizes the difference in the full field nodal displacement values. The correct displacement values can be calculated by simply evaluating a polynomial. These are then compared with the nodal displacements of a new FE run to evaluate the error from a new material model.

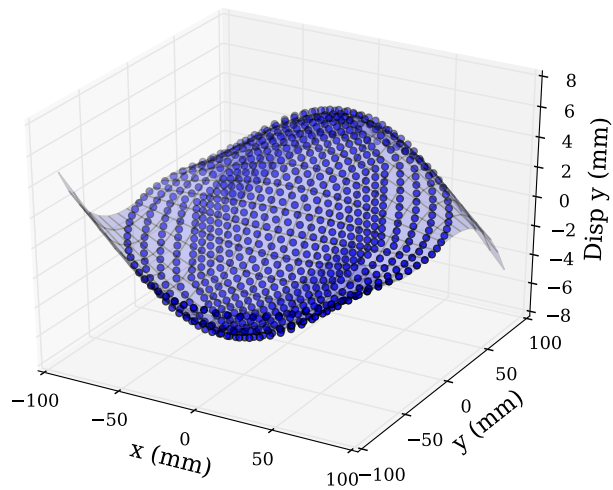


**Figure 4.5:** Nodal displacement  $y$  values on the fitted fourth order polynomial surface at 300 kPa

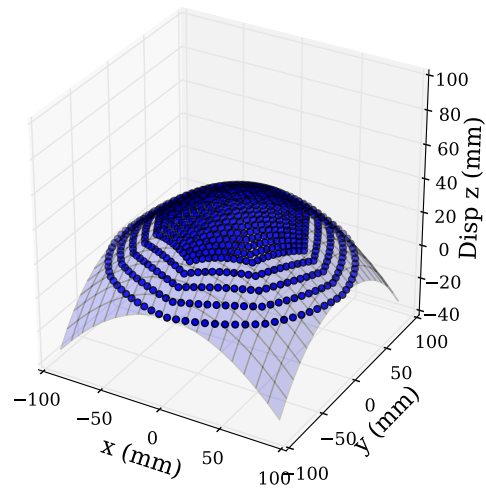


**Figure 4.6:** Nodal displacement  $z$  values on the fitted fourth order polynomial surface at 300 kPa

A DIC setup using at least two cameras is capable of accurately providing the full three dimensional displacement field on a physical bubble inflation test. It can be cumbersome setting up the DIC to calculate displacement

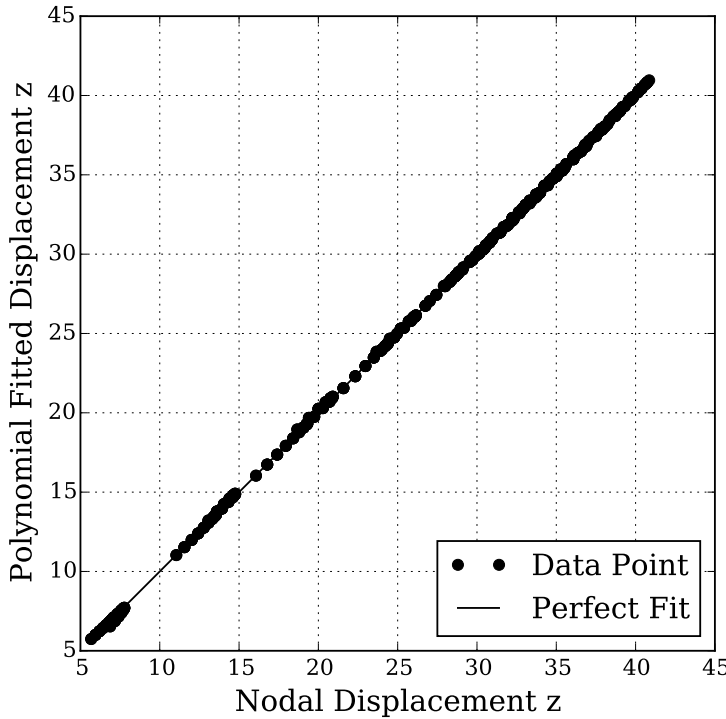


**Figure 4.7:** Displacement  $z$  nodal values against the displacement  $z$  polynomial fitted values at 300 kPa

**Table 4.1:** Coefficient of determination for the polynomials used to define the bubble displacements

| Pressure (kPa) | $R^2$ Disp $x$ | $R^2$ Disp $y$ | $R^2$ Disp $z$ |
|----------------|----------------|----------------|----------------|
| 22             | 0.99999        | 0.99971        | 0.99999        |
| 59             | 0.99999        | 0.99980        | 0.99999        |
| 97             | 0.99998        | 0.99994        | 0.99999        |
| 132            | 0.99994        | 0.99989        | 0.99999        |
| 186            | 0.99986        | 0.99970        | 0.99998        |
| 251            | 0.99967        | 0.99901        | 0.99994        |
| 300            | 0.99962        | 0.99836        | 0.99994        |

values at the exact node locations of the FE model. Instead of mapping the DIC displacement values to specific node locations, a polynomial surface of best fit is used. These polynomials can be arranged such that the axes align with that of the FE mesh. Then the polynomial can be evaluated at the FE model's node locations to compare the displacement results of the FE model and the physical test. Additionally the polynomials represent a smooth surface to match the full displacement field to the FE model. This smooth

surface eliminates noise in test data that may result from the DIC calculated displacement data. Thus the inverse bubble inflation test can be utilized on physical test data easily by swapping the current displacement polynomials with displacement polynomials from a physical test.

The inverse bubble inflation test was first attempted by only matching the nodal  $z$  values of the FE models. It was then discovered that the physical shape was non-unique to the material model. This was because very different non-linear material models could reproduce a nearly identical inflated bubble shape. Instead, by matching the full displacement field ( $x$ ,  $y$ , and  $z$  displacement components) it ensured that a unique solution was determined.

## 4.3 Optimization

Optimization is the mechanism used by the inverse method to determine material model parameters. The FE analysis results for a particular set of material model parameters is compared against the solution, utilizing a single objective function. An objective function value of 0.0 indicates that the exact displacement field was produced. This objective function is minimized until a local minimum has been found. Multiple gradient optimizations are run simultaneously from random starting points to determine the global minimum, which represents the material model determined by the inverse bubble inflation test.

### 4.3.1 Objective Function

Root mean square (RMS) error is used to evaluate how well the FE results of a particular material model matches with the known solution. The error can be represented by a single value for each FE analysis. This single value is minimized as the optimizer searches for the ideal material model.

At each of the seven pressures for which polynomials were fitted to the bubble inflation model (see Table 4.1), three RMS errors are calculated. One for each nodal displacement direction. The fitted polynomials (which could represent experimental bubble inflation displacement data, but in this case represent the known solution) are the terms  $P_x$ ,  $P_y$ , and  $P_z$ . The results of the FE model nodal displacements for a new material model are the terms  $d_x$ ,  $d_y$ , and  $d_z$ . Both the polynomials and the displacements are functions of pressure  $p$ , as there is a unique set of polynomials and displacements for each of the seven pressures of interest. The root mean square errors for the three directions are seen in Eqs. 4.5 - 4.7 as functions of pressure, where  $n$  represents the total number of nodes.

$$e_x(p) = \sqrt{\frac{\sum_{i=1}^n (d_{x_i}(p) - P_{x_i}(p))^2}{n}} \quad (4.5)$$

$$e_y(p) = \sqrt{\frac{\sum_{i=1}^n (d_{y_i}(p) - P_{y_i}(p))^2}{n}} \quad (4.6)$$

$$e_z(p) = \sqrt{\frac{\sum_{i=1}^n (d_{z_i}(p) - P_{z_i}(p))^2}{n}} \quad (4.7)$$

In total, 21 different root mean square error terms are calculated for the three directions at seven different pressures. A single error value which represents the overall fit between the FE bubble inflation model and the solution can be created by simply summing up all of the root mean square errors. However this introduces bias into the objective function. The FE bubble model is inflated in the  $z$  direction, thus it is anticipated that the nodal displacements will always be larger in the  $z$  direction as opposed to the  $x$  and  $y$  displacements. In an effort to reduce this bias, each root mean square error is normalized by the maximum polynomial value at the corresponding pressure. The result is a summation of equally weighted errors seen in Eq. 4.8. Thus  $e$  represents a single value that describes the entire fit between the known solution and the attempted material model.

$$e = \sum_{i=1}^7 \frac{e_x(i)}{\max(P_x(i))} + \frac{e_y(i)}{\max(P_y(i))} + \frac{e_z(i)}{\max(P_z(i))} \quad (4.8)$$

Optimization is used to minimize  $e$  the overall error of the FE model's results for a particular material model. The formulated objective function is subjected to two constraints, the first being that the moduli in the material model remain positive for their entire strain limit. The second being that the FE analysis is valid, in which case Marc outputs an exit code of 3004. The two constraints are true-false booleans, implemented in the same way as discussed in Chapter 3. The objective function is summarized in Eq. 4.9.

$$\begin{aligned} & \text{minimize: } e \\ & \text{such that: } E_1, E_2, G_{12} > 0 \quad \text{and} \\ & \quad \text{Marc Exit Code} = 3004 \end{aligned} \quad (4.9)$$

### 4.3.2 Procedure

Multiple optimizations are run to ensure that the best material model is found. Fifty starting points are randomly generated between the upper and lower bounds. Each starting point, is then run through the bubble inflation FE analysis to ensure the constraints are satisfied. If a constraint is violated for a particular starting point, a random starting point is generated between the

bounds. This process is repeated until each starting point begins in the feasible region. It is ensured that each starting point satisfies the constraints, because the DOT optimizer cannot start with a violated true-false constraint. The material model variables chosen as the solution and optimization bounds are listed in Table 4.2. These bounds were chosen to be an order of magnitude in size, with the solution variable appearing somewhere between the bounds. If the solution is unknown, appropriate bounds may be chosen around the result of a single initial optimization. Random starting points were found easier to generate than starting points selected from a latin hypercube sampling that reside in the feasible region. Often a set of starting points, generated from a latin hypercube sampling, included points that violated one or more of the constraints. In order to overcome the violated constraints, a new latin hypercube sampling was generated. The repeated formation of latin hypercube starting points was found more computationally intensive than obtaining starting points generated from random to reside in the feasible region. All 50 optimizations were run simultaneously with the MMFD algorithm. The material model determined from the inverse method has the lowest found objective function.

**Table 4.2:** Variables and bounds used for the non-linear orthotropic material model

|              | Solution                  | Lower Bound           | Upper Bound          |
|--------------|---------------------------|-----------------------|----------------------|
| $\beta_0$    | $-7.96788 \times 10^{-3}$ | $-1.0 \times 10^{-2}$ | $0.0 \times 10^0$    |
| $\beta_1$    | $7.10747 \times 10^{-1}$  | $0.0 \times 10^0$     | $1.0 \times 10^0$    |
| $\beta_2$    | $-1.56912 \times 10^{-1}$ | $-3.0 \times 10^{-1}$ | $0.0 \times 10^0$    |
| $\beta_3$    | $2.00439 \times 10^{-2}$  | $7.0 \times 10^{-3}$  | $7.0 \times 10^{-2}$ |
| $\beta_4$    | $-1.06241 \times 10^1$    | $-1.0 \times 10^3$    | $1.0 \times 10^2$    |
| $\beta_5$    | $1.37830 \times 10^1$     | $-1.0 \times 10^1$    | $1.0 \times 10^2$    |
| $\beta_6$    | $-9.31830 \times 10^{-1}$ | $-1.0 \times 10^1$    | $1.0 \times 10^0$    |
| $\beta_7$    | $1.39437 \times 10^{-1}$  | $5.0 \times 10^{-2}$  | $5.0 \times 10^{-1}$ |
| $\beta_8$    | $-4.79622 \times 10^2$    | $-1.0 \times 10^3$    | $0.0 \times 10^0$    |
| $\beta_9$    | $2.12650 \times 10^2$     | $0.0 \times 10^0$     | $7.0 \times 10^2$    |
| $\beta_{10}$ | $-2.02028 \times 10^1$    | $-7.0 \times 10^1$    | $0.0 \times 10^0$    |
| $\beta_{11}$ | $8.06350 \times 10^{-1}$  | $2.5 \times 10^{-1}$  | $1.5 \times 10^0$    |

The DOT parameters are utilized in their default configuration. The overall optimization process is well suited for parallel computing as the 12 variable gradient search may be performed at the same time. In addition multiple cores can be used in the FE bubble inflation analysis.

## 4.4 Results

All 50 optimizations were performed in parallel. The optimum determined from each starting point can be seen in Figure 4.8, sorted from the worst objective value found to the best. The result of each optimization represents a local minimum that was found in the design space. It is important to note that no two optimizations found the exact same optimum material model. More than half of the optimizations resulted in an objective value less than 0.5, in which an objective of zero represents a material model that produces the exact same displacement field as the solution. These low objective functions suggest that resulting material models produce nodal displacements similar to the solution. However, the large number of local minima suggests that the problem is not well posed.

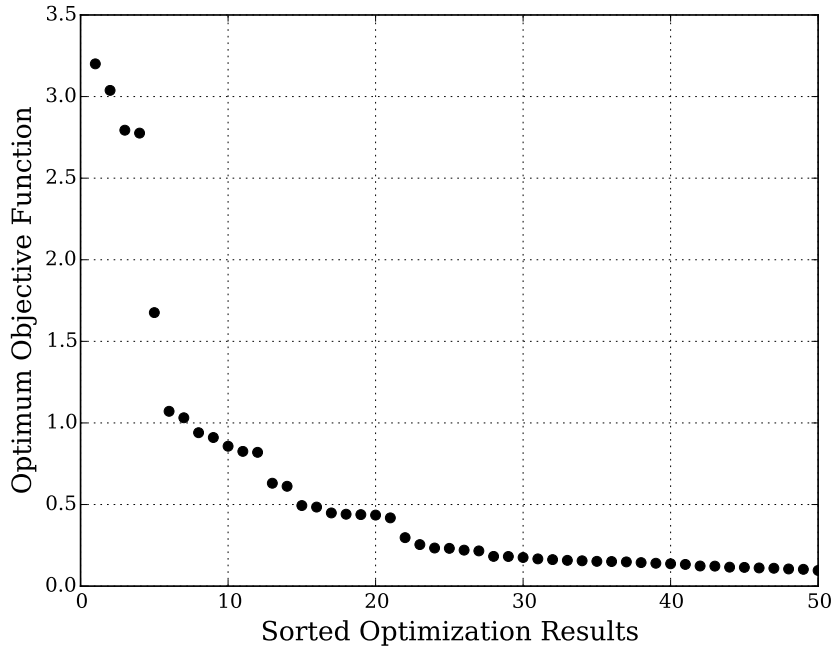


**Figure 4.8:** Optima sorted from worst to best of optimization results from 50 random starting points

The material models determined through the optimization are similar to the known solution. The solution is the material model that was utilized in generating the polynomial displacement surfaces. The material models resulting from the top 10 percent of optimizations, alongside the solution material model are shown in Figure 4.9. The small variance between moduli curves leads to even smaller deviations in the full displacement field of the FE model.

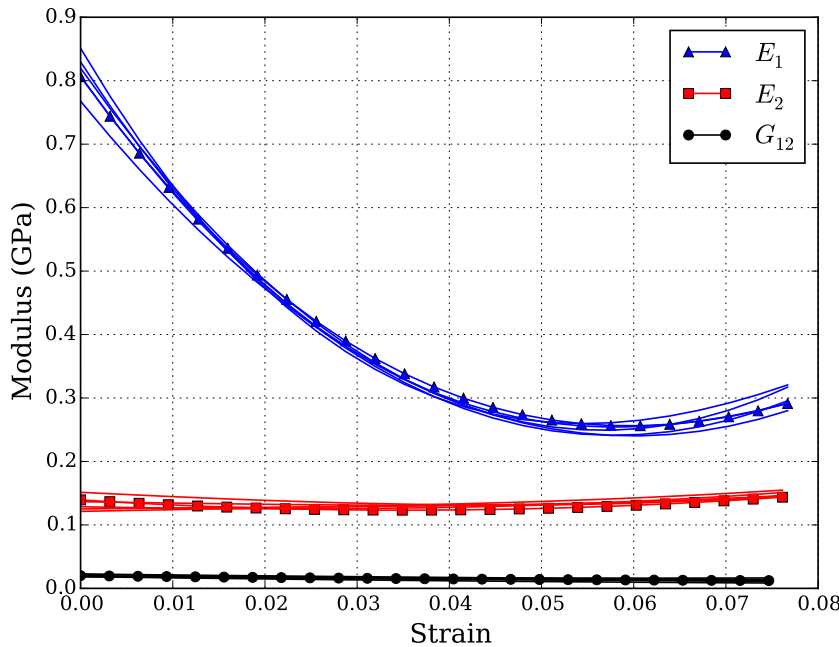


**Figure 4.9:** Five best material models resulting from the optimization of 50 random starting points plotted alongside known solution

The best material model parameters produce a displacement field that is nearly identical to the known solution. Two-dimensional plots of the node locations cut through the  $y$  and  $x$  axes, as the material is inflated, are shown in Figures 4.10 & 4.11. The node locations resulting from the 10 percent best found material models are plotted alongside the known solution. At the seven pressures, the node locations are analogous among the different material models. It can be further noted that the subtle variance in the best material models (seen in Figure 4.9) is even less noticeable in the cut through plots of the FE bubble inflation models.

The inverse bubble inflation test was demonstrated by reproducing a highly non-linear material model of a known solution. However, obtaining the exact non-linear material model of the bubble inflation test poses to be a challenging optimization problem. This can be seen by the large number of local minimum discovered while not finding an objective function of zero.

## 4.4. RESULTS

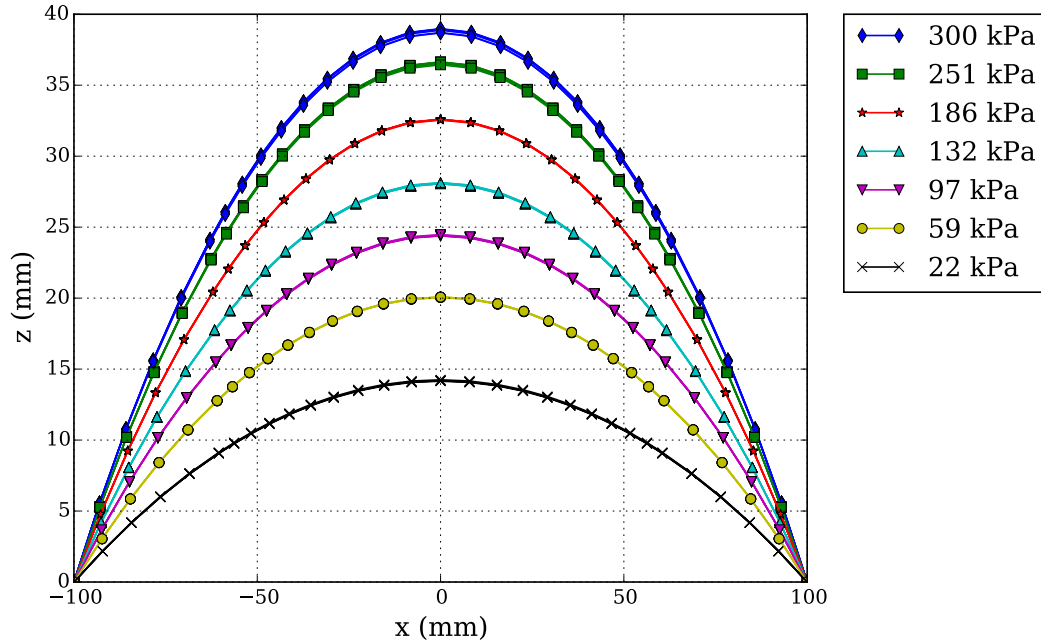


**Figure 4.10:** Node locations cut through the  $y$  axis from the FE bubble inflation models of the five best material models plotted alongside the known solution

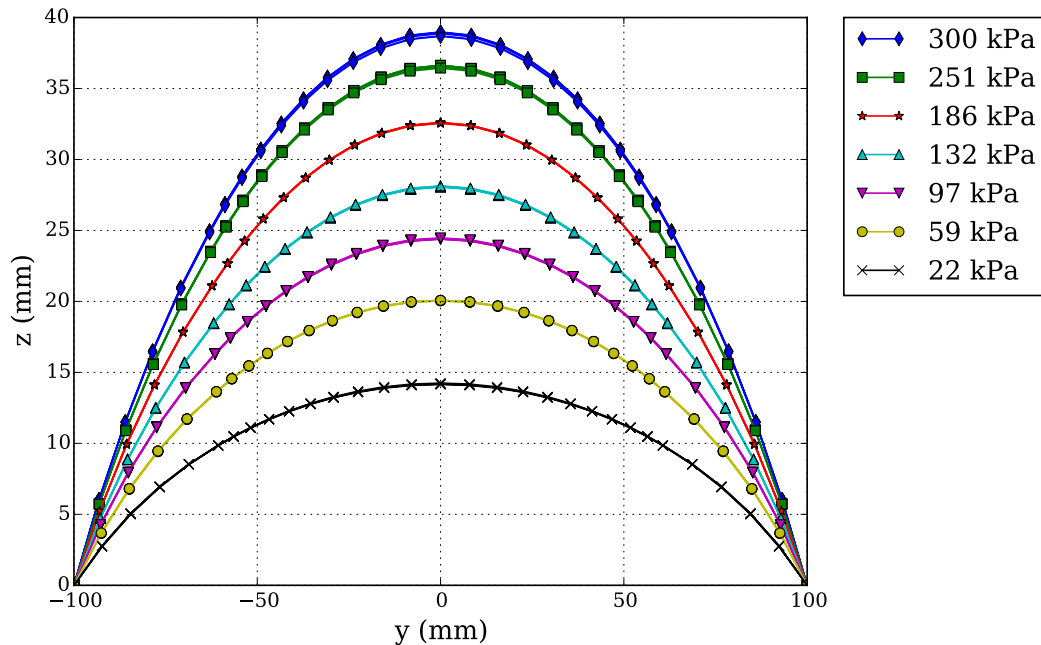


**Figure 4.11:** Node locations cut through the  $x$  axis from the FE bubble inflation models of the five best material models plotted alongside the known solution

# Chapter 5

## Inverse Bubble Tests

This chapter describes the bubble inflation test setup. Multiple bubble inflation tests were performed on PVC-coated polyester, however only four bubble inflation tests were processed with inverse bubble analysis. A unique non-linear orthotropic material model was determined from each of the four bubble inflation tests. The non-linear orthotropic material models from the inverse bubble analysis and uniaxial tests were compared directly. To better understand how the different material models affect the load displacement behavior of a structure, finite element (FE) models of the uniaxial test were run using the inverse bubble inflation material models. The results of these uniaxial FE models are compared directly to the uniaxial test. It was shown that inverse bubble inflation material models produced load displacement behavior that did not match the uniaxial tests.

### 5.1 Bubble Inflation Test

The bubble inflation test fixture is seen in Figure 5.1. The fixture consists of two aluminum parts. The diameter of the circular hole is 200 mm. Initially 16 M6 bolts were used to secure the top plate to the base of the fixture. However, it was found that the M6 bolts did not provide a sufficient clamping force to secure the PVC-coated polyester. Tests where the PVC-coated polyester slips during the bubble inflation test are invalid, because it is difficult to account for the slip in the boundary conditions of the numerical model used in the inverse analysis. The test fixture was reworked to allow for 16 M10 bolts. The M10 bolts produced better bubble inflation tests, as the PVC-coated polyester slipped less with the M10 bolts than the M6 bolts. The M10 bolts were torqued between 15 and 20 N m for testing.

There are two push-in fittings on the base of the bubble inflation fixture. The purpose of one fitting is to supply the pressurized compressed air to the bubble test, while the other fitting is used to monitor the pressure. Additional information about the Festo SPTE-P10R-S4-V-2.5K pressure transmitter used

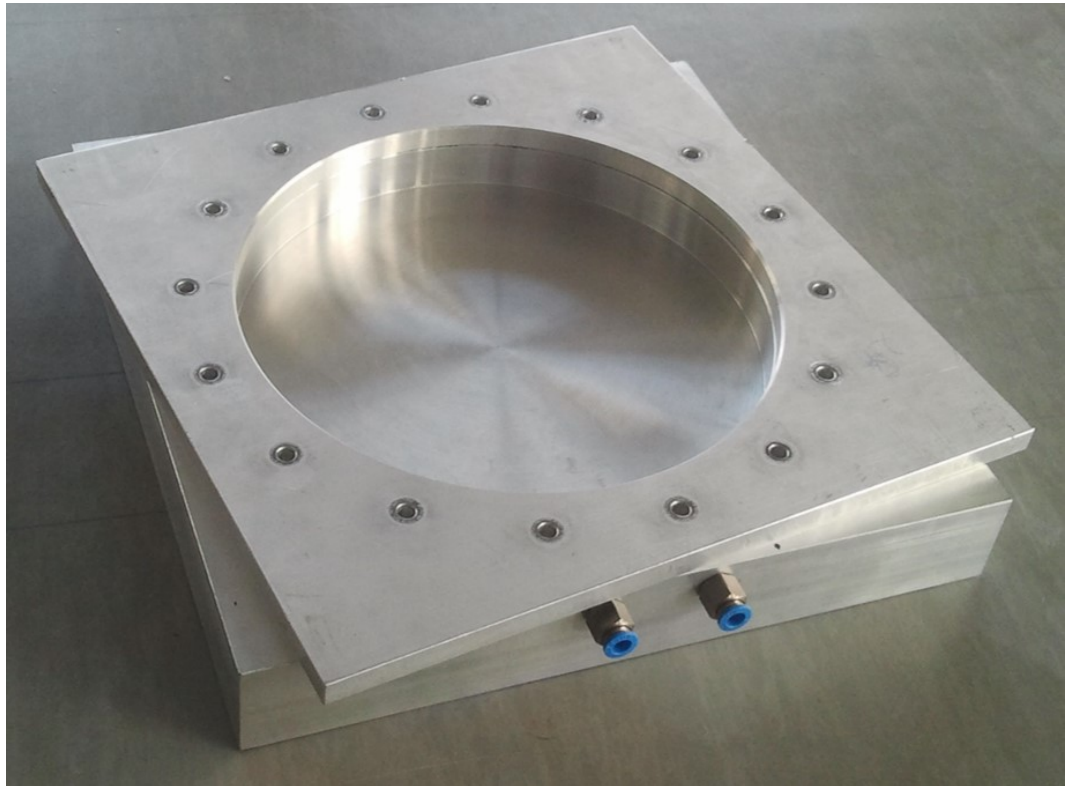


**Figure 5.1:** Top plate resting on the base of the aluminum bubble inflation test fixture

in the bubble inflation tests can be seen in Appendix B. For a bubble test, the pressure is manually increased by adjusting a throttle valve to increase the flow rate.

Bubble inflation tests were recorded using the StrainMaster Digital Image Correlation (DIC) hardware and the DaVis software. The test images and pressures are synchronously recorded, such that the pressure values become embedded in the images. The cameras were positioned directly above the bubble test fixture, such that the entire sample was visible by both cameras. The two cameras were placed as far apart as possible on the StrainMaster, however the angle between the cameras and the center of the bubble test was less than 90°.

Multiple bubble inflation tests were performed with similar camera set-ups. However, only four bubble inflation tests were processed with the DaVis software. Tests which the material slipped from the test fixture were discarded. The four bubble inflation tests processed did not slip. The maximum strain values from the bubble tests are presented in Table 5.1. It is noted that the maximum strain in the fill direction is higher than the strain in the warp direction, which agrees with the uniaxial tests which showed that the material was stiffer in the warp direction. The stiffer material direction is expected to

deform less, therefore the warp direction experiences less material strain.

The DIC calculated strain values overlaid on the bubble test fixture for the final image of bubble inflation test 3 are presented in Figures 5.2 - 5.4. In general the strain fields exhibit a smooth transition from the data points, however there are a few areas on the surface which experience an unusually high strain value. These high values are believed to result from numerical noise. The strain values of Table 5.1 were chosen by looking at similar strain overlays for the different bubble tests. The maximum strain value was chosen utilizing engineering judgment as opposed to picking the maximum strain value based on the image, because the presence of a high strain value in a small area poorly represents the maximum strain value experienced by the test. The maximum strain values are important, because the material model cannot be characterized beyond the maximum strain.

**Table 5.1:** Maximum engineering strain values (mm/mm) of the bubble tests in the warp ( $\varepsilon_1$ ), fill ( $\varepsilon_2$ ), and shear ( $\gamma_{12}$ ) material directions

|                 | Test 1 | Test 2 | Test 3 | Test 4 |
|-----------------|--------|--------|--------|--------|
| $\varepsilon_1$ | 0.12   | 0.16   | 0.13   | 0.19   |
| $\varepsilon_2$ | 0.14   | 0.21   | 0.15   | 0.24   |
| $\gamma_{12}$   | 0.04   | 0.07   | 0.07   | 0.08   |

## 5.2 Inverse Analysis

The four bubble inflation tests were inflated to different pressures and at different rates, because the pressure was controlled manually with a throttle valve. A unique non-linear orthotropic material model was determined for each bubble inflation test using the process demonstrated in Chapter 4. Despite the different pressures chosen for the inverse analysis and the different inflation rates of the bubble tests, all bubble inflation tests produced similar non-linear orthotropic material models.

The DIC bubble inflation results are compared to the numerical model at seven unique pressures, which is the same as the method used in Chapter 4. The pressures used for each test are presented in Table 5.2. The set of pressures were chosen based on the pressures of the recorded DIC images, of which the pressures were approximately equally spaced. It was not possible to obtain seven pressure increments that were exactly equal in spacing from the captured DIC data.

For each bubble inflation test, the least squares method was used to fit fourth order polynomial surfaces to the DIC displacement values in the  $x$ ,  $y$ , and  $z$  directions. Thus for each unique pressure in Table 5.2, there are 3 unique

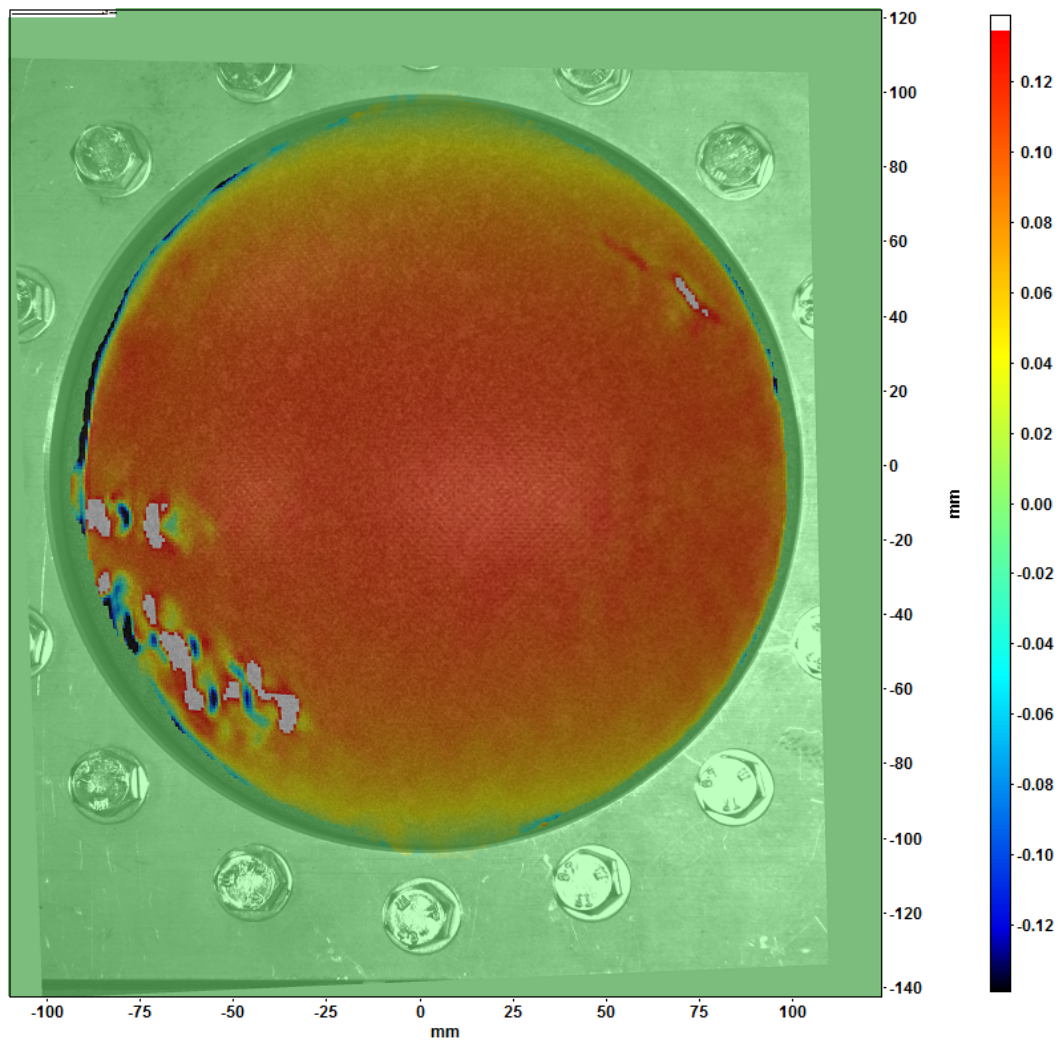


**Figure 5.2:** Maximum strain values in the warp direction ( $\varepsilon_1$ ) of bubble inflation test 3 overlaid on the DIC image

**Table 5.2:** The seven unique pressures (kPa) used for the inverse analysis of the recorded bubble tests

| Test 1 | Test 2 | Test 3 | Test 4 |
|--------|--------|--------|--------|
| 22     | 102    | 54     | 85     |
| 59     | 180    | 103    | 171    |
| 97     | 303    | 143    | 252    |
| 132    | 400    | 188    | 331    |
| 186    | 463    | 234    | 420    |
| 251    | 534    | 281    | 495    |
| 300    | 560    | 328    | 580    |

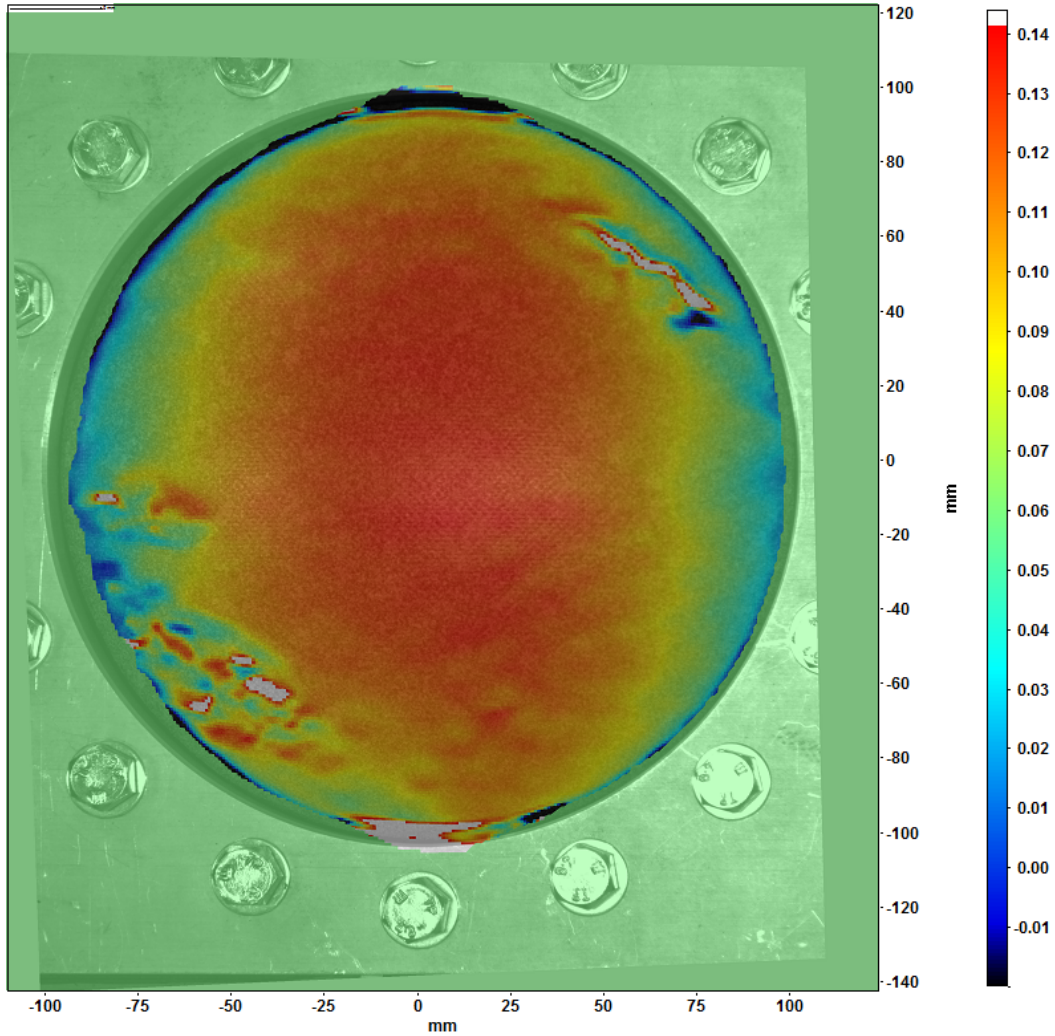


**Figure 5.3:** Maximum strain values in the fill direction ( $\varepsilon_2$ ) of bubble inflation test 3 overlaid on the DIC image

polynomial surfaces. The coefficient of determination for fitted displacement polynomials of bubble inflation test 4 are seen in Table 5.3. Test 4 is presented because it had the worst coefficients of determination values. Despite having the worst fits of the four bubble tests, the lowest coefficient of determination was 0.923 which still suggests an acceptable fit. A comparison of the fitted displacement  $z$  values from the fitted polynomial and the DIC displacement  $z$  values of test 3 is presented in Figure 5.5. The quality of the fitted fourth order polynomials are good, however the polynomials are not perfect fits and do not match the DIC displacement values exactly.

Fifty inverse analysis optimizations were performed for each bubble test, using random starting points between the bounds of Table 4.2. Many optimization runs resulted in variable  $\beta_3$  hitting the upper boundary, so the upper

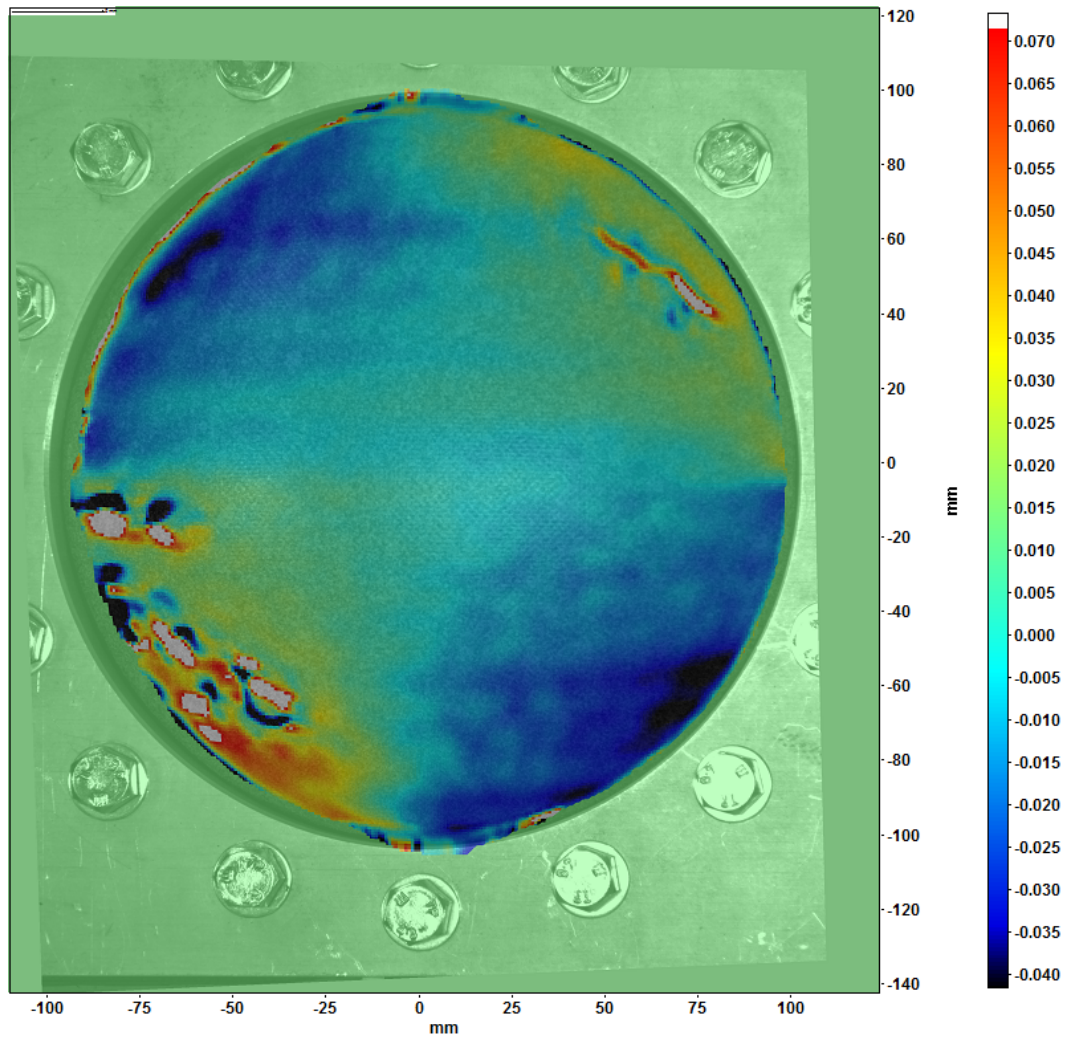


**Figure 5.4:** Maximum strain values in the shear direction ( $\gamma_{12}$ ) of bubble inflation test 3 overlaid on the DIC image

**Table 5.3:** Coefficient of determination for the polynomials used to define the DIC displacements of bubble inflation test 4

| Pressure (kPa) | $R^2$ Disp x | $R^2$ Disp y | $R^2$ Disp z |
|----------------|--------------|--------------|--------------|
| 85             | 0.923        | 0.962        | 0.976        |
| 171            | 0.976        | 0.989        | 0.990        |
| 252            | 0.987        | 0.994        | 0.993        |
| 331            | 0.991        | 0.996        | 0.995        |
| 420            | 0.993        | 0.996        | 0.996        |
| 495            | 0.994        | 0.996        | 0.996        |
| 580            | 0.995        | 0.997        | 0.997        |

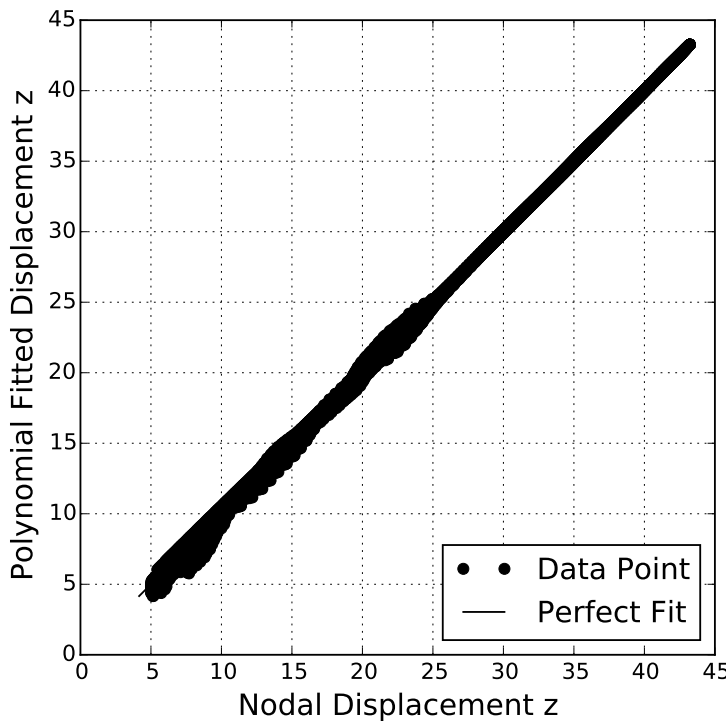


**Figure 5.5:** Displacement  $z$  nodal values against the displacement  $z$  polynomial fitted values at 328 kPa of bubble inflation test 3

bound was increased and the optimization run again. The optimum determined from each optimization can be seen in Fig. 5.6, sorted from the worst objective value found to the best. The optima represent the local minima in the objective function found by the optimization. It can be noted that the design space appears to be fairly flat, meaning that the local minima have a similar objective function value near the best found objective function. The objective functions are higher for bubble test 2 and 4, which were inflated to a higher pressure than bubble test 1 and 3. The non-linear orthotropic material model from each bubble test was determined to be the best found objective function from the set of 50 optimizations. It is important to mention that the best objective function from each of the batches of optimizations were lower than the objective functions of the uniaxial material models, however this wasn't true for all 50 optimizations in a batch.

### 5.3. RESULTING NON-LINEAR ORTHOTROPIC MATERIAL MODEL COMPARISON

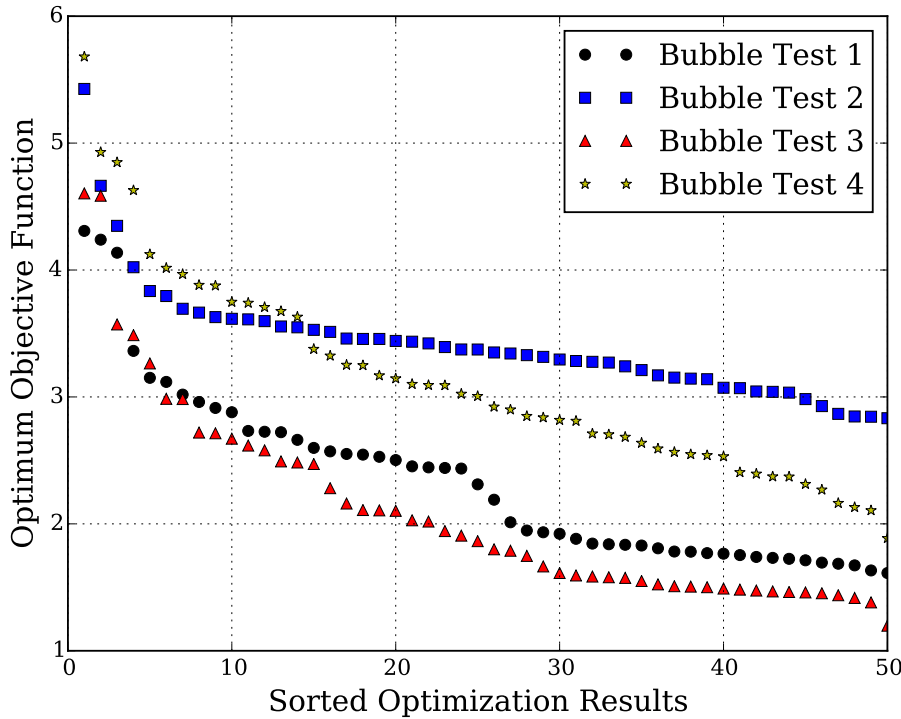


**Figure 5.6:** Optima sorted from worst to best objective function of optimization results from 50 random starting points for the four bubble inflation tests

## 5.3 Resulting Non-linear Orthotropic Material Model Comparison

The variables defining the non-linear orthotropic material models determined from the inverse bubble inflation analyses are presented in Table 5.4. It can be clearly noted that each bubble test resulted in a different material model since each test produced different  $\beta$  variables. This section will compare the moduli from the non-linear orthotropic material models resulting from the uniaxial and the inverse bubble inflation analyses.

The non-linear orthotropic material models'  $E_1$  component, determined from the uniaxial and inverse bubble tests, is presented in Figure 5.7. Each curve is limited to the maximum strain value  $\varepsilon_1$  experienced by the test. While each of the bubble tests produced an  $E_1$  value that is of the same order of magnitude as the uniaxial value, the bubble test materials do not match the uniaxial  $E_1$  component. In general, the bubble material models over or under predict the magnitude of the uniaxial  $E_1$  at points throughout the strain range.

The non-linear orthotropic material models'  $E_2$  competent, determined from the uniaxial and inverse bubble tests, is presented in Figure 5.8. Each curve is limited to the maximum strain value  $\varepsilon_2$  experienced by the test. As

**Table 5.4:** Variables of the non-linear orthotropic material models determined from the inverse analysis on the four bubble tests

|              | Test 1                    | Test 2                    | Test 3                    | Test 4                    |
|--------------|---------------------------|---------------------------|---------------------------|---------------------------|
| $\beta_0$    | $-1.28170 \times 10^{-3}$ | $-4.42858 \times 10^{-3}$ | $-1.09230 \times 10^{-3}$ | $-2.97973 \times 10^{-3}$ |
| $\beta_1$    | $9.49079 \times 10^{-1}$  | $9.87096 \times 10^{-1}$  | $8.24376 \times 10^{-1}$  | $3.67627 \times 10^{-1}$  |
| $\beta_2$    | $-4.48869 \times 10^{-2}$ | $-2.05457 \times 10^{-1}$ | $-1.73231 \times 10^{-1}$ | $-1.01234 \times 10^{-1}$ |
| $\beta_3$    | $8.04287 \times 10^{-2}$  | $9.33764 \times 10^{-2}$  | $1.22820 \times 10^{-1}$  | $8.26297 \times 10^{-2}$  |
| $\beta_4$    | $9.70652 \times 10^1$     | $6.73425 \times 10^1$     | $9.99878 \times 10^1$     | $8.17789 \times 10^1$     |
| $\beta_5$    | $1.23017 \times 10^1$     | $1.46374 \times 10^1$     | $-2.19352 \times 10^0$    | $1.56849 \times 10^1$     |
| $\beta_6$    | $-2.75939 \times 10^0$    | $-3.42911 \times 10^0$    | $-2.44582 \times 10^0$    | $-4.03842 \times 10^0$    |
| $\beta_7$    | $1.18880 \times 10^{-1}$  | $1.46766 \times 10^{-1}$  | $1.89481 \times 10^{-1}$  | $1.81033 \times 10^{-1}$  |
| $\beta_8$    | $-1.59163 \times 10^2$    | $-3.81685 \times 10^2$    | $-3.65789 \times 10^2$    | $-2.89436 \times 10^2$    |
| $\beta_9$    | $3.81894 \times 10^2$     | $1.32145 \times 10^2$     | $3.07545 \times 10^2$     | $9.75725 \times 10^1$     |
| $\beta_{10}$ | $-4.04413 \times 10^1$    | $-1.26632 \times 10^1$    | $-3.34450 \times 10^1$    | $-9.87010 \times 10^0$    |
| $\beta_{11}$ | $1.17116 \times 10^0$     | $7.42916 \times 10^{-1}$  | $9.89845 \times 10^{-1}$  | $5.63206 \times 10^{-1}$  |

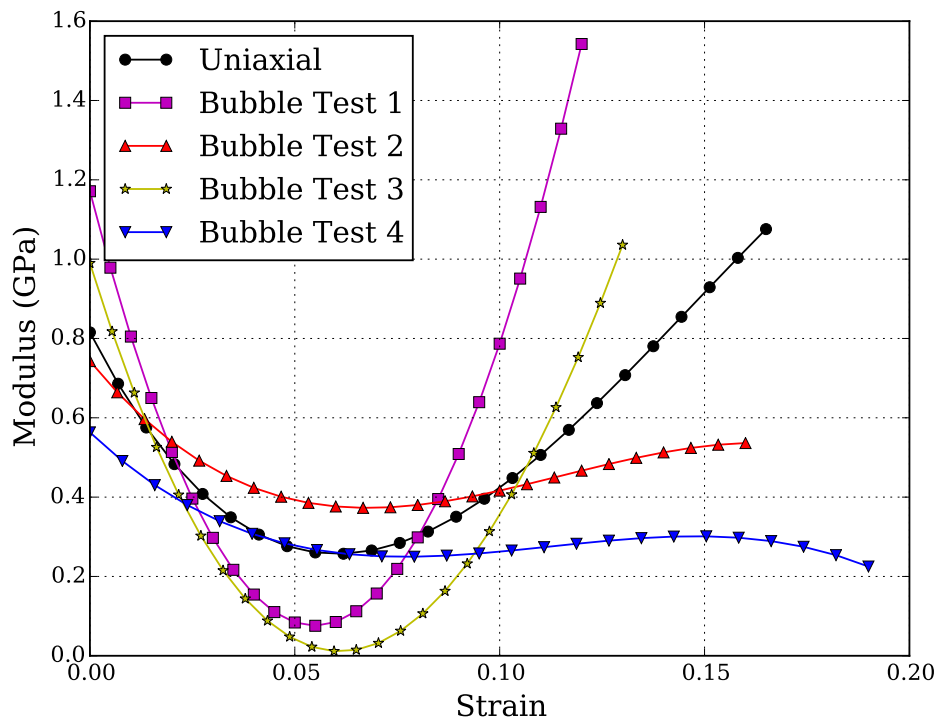


**Figure 5.7:** Non-linear orthotropic  $E_1$  determined from the uniaxial and inverse bubble inflation tests limited to the maximum strain value

was the case with the  $E_1$  modulus, the bubble tests generally over and under predict the magnitude of the uniaxial  $E_2$  at different strain values. It was

### 5.3. RESULTING NON-LINEAR ORTHOTROPIC MATERIAL MODEL COMPARISON

57

observed that there is much less variance between the bubble test  $E_2$  moduli than the previously discussed  $E_1$  moduli. This suggests that the inverse bubble inflation method was producing similar  $E_2$  functions, while the  $E_2$  curves from the bubble tests are noticeably different than the curve from the uniaxial test.

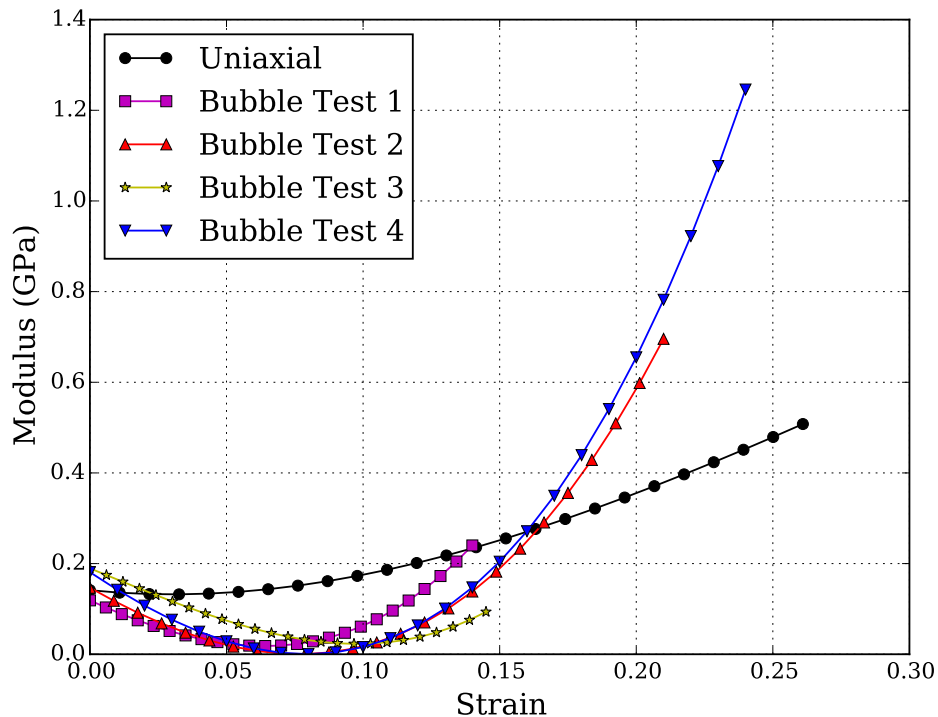


**Figure 5.8:** Non-linear orthotropic  $E_2$  determined from the uniaxial and inverse bubble inflation tests limited to the maximum strain value

The non-linear orthotropic material models'  $G_{12}$  competent, determined from the uniaxial and inverse bubble tests, is presented in Figure 5.9. Each curve is limited to the maximum strain value  $\gamma_{12}$  experienced by the test. The shear strain values experience by the bubble test are significantly smaller than the failure shear strain of the uniaxial test. The bubble tests produced similar  $G_{12}$  curves, however these curves are severely stiffer for the low bubble test strains than the  $G_{12}$  curve from the uniaxial tests. The  $G_{12}$  values from the bubble test are almost an order of magnitude larger than the uniaxial values for the same strain range. However, the bubble test  $G_{12}$  values produced moduli that are represented by a strain range between 0.4 and 0.5 of the uniaxial test, despite the maximum shear strain of the bubble tests only being 0.08.

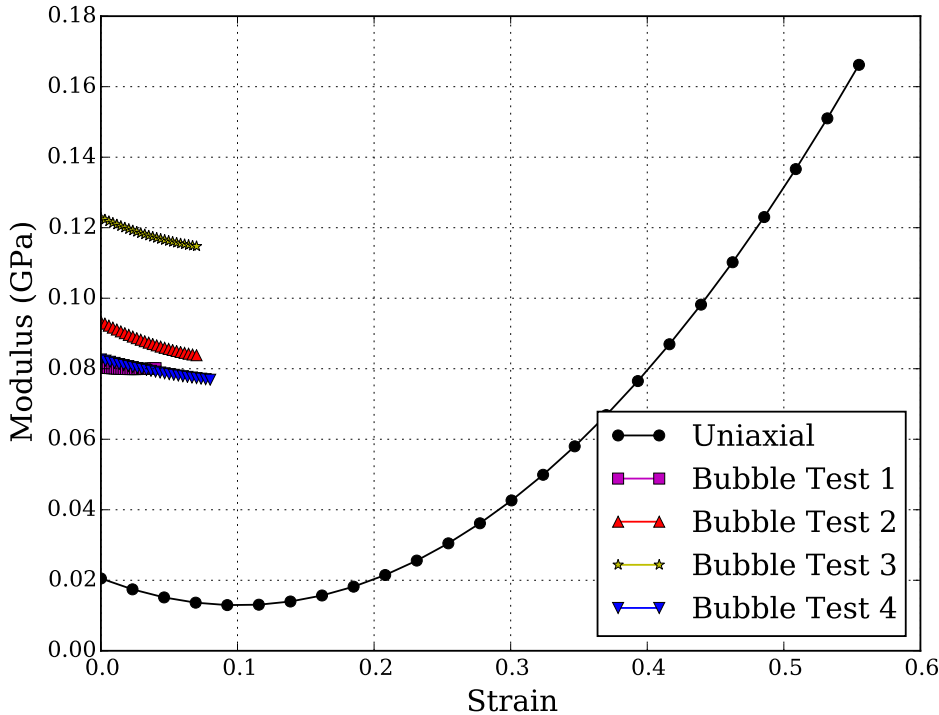


**Figure 5.9:** Non-linear orthotropic  $G_{12}$  determined from the uniaxial and inverse bubble inflation tests limited to the maximum strain value

## 5.4 Uniaxial Tests and Material Model Comparison

The non-linear orthotropic material models determined from the inverse bubble inflation tests were used with the non-linear FE models of Chapter 3. The FE models were previously used to determine the non-linear orthotropic material model from the uniaxial tests. There is one FE model for each of the three distinct uniaxial tests in the warp, fill, and  $45^\circ$  bias material direction. The FE models are run with the inverse bubble material models to compare the inverse bubble inflation tests directly to the uniaxial material response. Additionally the uniaxial FE models help to evaluate how the different moduli determined from the bubble tests affect a load displacement relationship.

The load displacement results of the FE models in the warp direction are plotted alongside the uniaxial test, used to create the uniaxial material model, in Figure 5.10. At load displacement values, the bubble material models match well with the uniaxial test, however for larger displacements the load between the uniaxial test and the FE model may vary by as much as 200 N. There was no bubble material model that matched with the warp uniaxial test exactly.

The load displacement results of the FE models in the fill direction are

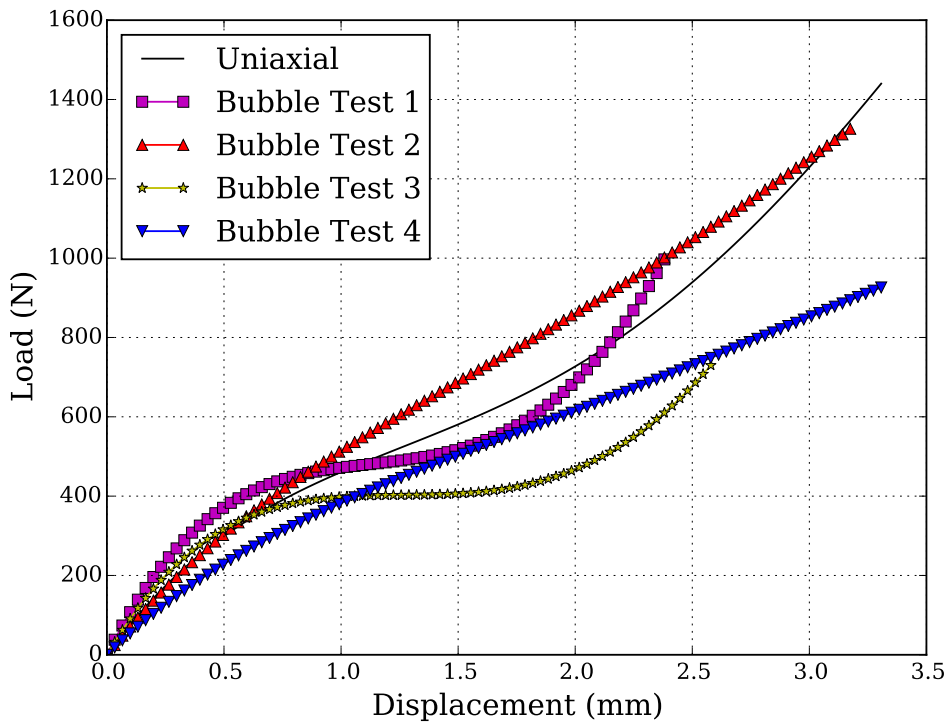


**Figure 5.10:** Warp uniaxial test and the results of the uniaxial FE models utilizing the bubble inflation material models

plotted in Figure 5.11 alongside the uniaxial test used to create the uniaxial material model. Each one of the bubble material models initially over predict the stiffness of the uniaxial test, but then severely under predict the stiffness. It can be seen that the bubble material models produce a large area of deformation without significant load, which is vastly different than the uniaxial test. This deformation without load may cause numerical instability, and create singular stiffness matrices. Overall the bubble material models capture the material response better in the warp material direction than the fill direction.

The load displacement curves resulting from the FE models in the  $45^\circ$  bias direction are plotted in Figure 5.12 alongside the uniaxial test used to create the uniaxial material model. The bubble material models were limited to the maximum strain of the bubble inflation tests. This strain limit on the bubble material models is the reason why the load displacement curves of the bubble material models in the  $45^\circ$  bias direction are extremely short. The shear modulus of the bubble material models is significantly larger at low strains than the uniaxial material model. Having a stiffer shear modulus, produces a significantly stiffer  $45^\circ$  bias load displacement curve for the bubble material models, than the  $45^\circ$  bias uniaxial test.

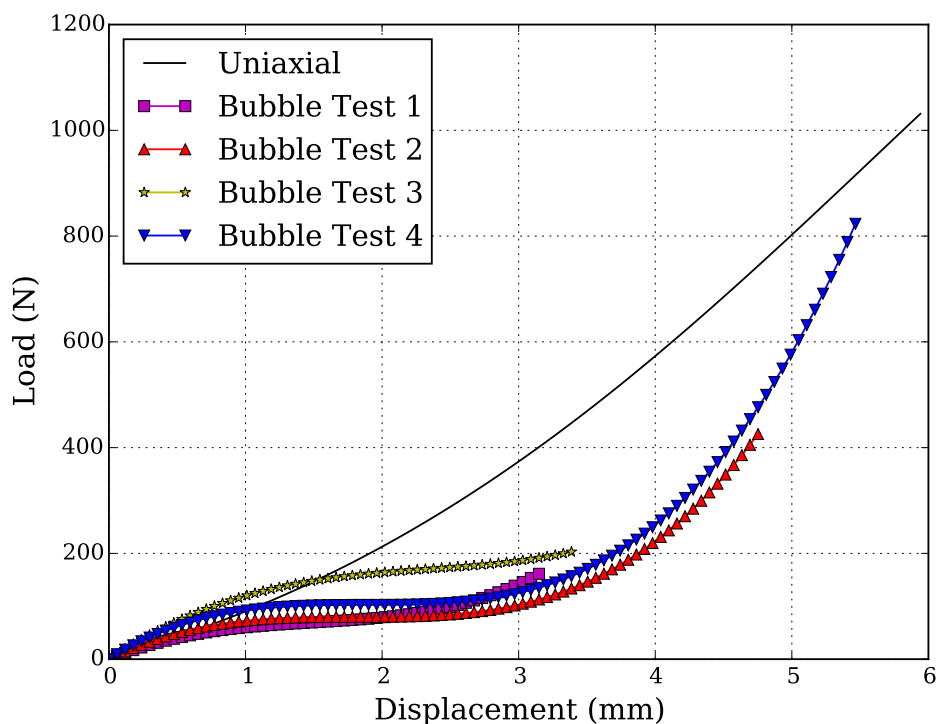


**Figure 5.11:** Fill uniaxial test and the results of the uniaxial FE models utilizing the bubble inflation material models

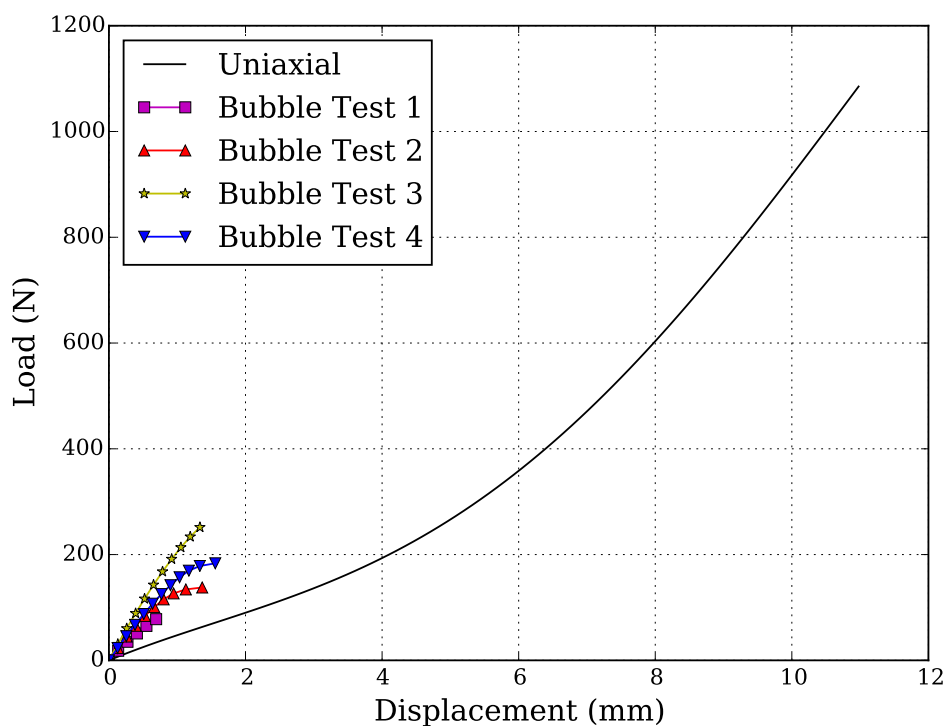


**Figure 5.12:**  $45^\circ$  bias uniaxial test and the results of the uniaxial FE models utilizing the bubble inflation material models

# Chapter 6

## Inflatable Beam Bending

Inflatable cylinders were manufactured from PVC-coated polyester. The inflatable cylinders were tested in a three point bending configuration. Finite element (FE) models were created to replicate the inflation, and three point bending of the cylinders. The FE models were run with the inverse bubble inflation and uniaxial material models. The load displacement results from the three point bending tests are presented along with the results of the FE models.

### 6.1 PVC-Coated Polyester Inflatable Cylinders

Three inflatable cylinders were manufactured by Ceasar Inflatables. The inflatables cylinders, pictured in Figure 6.1, are made from the same PVC-coated polyester tested in the uniaxial and bubble inflation tests. The cylinders are all three meters in length, with varying diameter of 150 mm, 200 mm, and 300 mm. The cylinders were chosen to have a length to diameter ratio greater than 10, such that the cylinders may be considered as slender beams by someone in the future.

Each PVC-coated cylinders was manufactured from a flat sheet of PVC-coated polyester. The PVC-coated polyester was bonded using an adhesive, creating a seam down the length of the cylinder. The seam has three layers of PVC-coated polyester, while the rest of the cylinder only has one layer. The end caps of the cylinder are also made from PVC-coated polyester, and secured to the cylinder using the same adhesive. A valve was bonded to one of the end caps. The valve and seam can be seen for one of the cylinders in Figure 6.2.

### 6.2 Three Point Bending Test Method

Three point bending was chosen to test the stiffness of the inflatable cylinders, because of the test's simplicity. A three point bending test only requires two supports. A load is applied between the two supports, such that the beam



**Figure 6.1:** Three PVC-coated polyester cylinders with diameters of 150 mm, 200 mm, 250 mm

bends symmetrically about the applied load. The load, deflection of the cylinder, and internal pressure are recorded. The stiffness of the inflatable cylinder depends on the inflation pressure. An inflatable cylinders can be referred to as an inflatable beam for the three point bending tests. FE models will be created of the bending inflatable beams, and used to validate the generated material models. Ideally it will be shown that, either the uniaxial, or the inverse bubble inflation material models better predict the load deflection behavior of the inflatable beams.

The 3-Point bending test consists of two end supports mounted to the floor in the structures laboratory. A polyester strap, rated for 2.7 tons, will be utilized to apply a load in the center of the inflatable beam. The strap runs through the floor, beneath the structures laboratory where weights will be hung from the strap. Weights will be applied in 5 kg increments until the inflatable cylinder buckles. There is a total of 80 kg of mass available in 5 kg increments to load the inflatable cylinder. The displacement of the bending beams was measured with an ASM WS12-2000-10V-L10 draw wire displacement sensor. Demonstration of the accuracy of the sensor can be seen in Appendix C. The draw wire was secured to the polyester tow strap. The sensor was positioned above the center of the inflatable cylinder. The same



**Figure 6.2:** Inflatable cylinder valve on the end cap and seam running down the length of the cylinder

pressure transducer used in the bubble inflation tests (the Festo SPTE-P10R-S4-V-2.5K of which additional information can be found in Appendix B) was used to measure the internal pressure of the inflatable cylinders. Both the displacement and the pressure were recorded with an HBM Spider8 bridge amplifier.

It is important that the boundary conditions of the three point bending test can be replicated with the FE method in order to accurately model the bending tests. Rigid supports can be simply modeled as rigid bodies with contact in the FE method. However, the interaction between the cylinder and the polyester tow strap would be difficult to reproduce in the FE method. Since modeling of rigid bodies with contact iterations is relatively simple, it was decided to place a rigid collar around the center of the inflatable cylinder. The load could be applied on the collar, which distributes the load onto the bending beam. Thus the load of the FE model can be applied by displacing a rigid collar around the center of the inflatable beam. The load information was extracted from the contact between the rigid body and the nodes of the cylinder. A cylindrical collar with an inner diameter of 240 mm and length of

## 6.2. THREE POINT BENDING TEST METHOD

## 65

145 mm was used for the 150 mm and 200 mm diameters cylinder. While a cylindrical collar with an inner diameter of 295 mm and length of 147 mm was used on the 250 mm cylinder.

An inflatable beam bending in the test setup is pictured in Figure 6.3. The collar in the center of the beam is seen in blue, while directly above the collar is the mounted draw wire displacement sensor. The two end supports used have an outer diameter of 100 mm. The dimensions of the test setup is presented in Figure 6.4. Each cylinder was tested such that the seam running down the length of the cylinder was placed on the two end supports.



**Figure 6.3:** 150 mm inflatable cylinder bending in the test setup

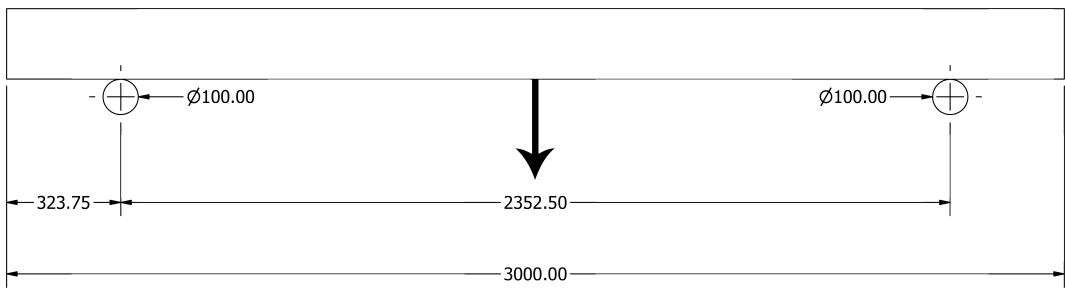


**Figure 6.4:** Dimensions in mm of three point bending test setup

The three inflatable cylinders were tested, each at three different pressures making up 9 test cases in total. Each test case was repeated three times to ensure quality measurements were recorded. After each test, the cylinders were lifted from the supports while the collar and polyester strap were repositioned.

| Diameter (mm) | Test 1 (bar) | Test 2 (bar) | Test 3 (bar) |
|---------------|--------------|--------------|--------------|
| 150           | 0.90         | 1.10         | 1.40         |
| 200           | 0.60         | 0.80         | 1.00         |
| 250           | 0.50         | 0.65         | 0.85         |

**Table 6.1:** This table shows the various diameters of inflatable cylinders along with the operating pressures used for the three point bending tests

It was necessary to reposition the beams after the test, as the beams moved during testing. Additionally the variance between the three tests, for the same load and pressure, provides information about the error in the testing environment. The pressures, of which the cylinders were inflated to, are seen in Table 6.1. Preliminary FE models utilizing the uniaxial material model were constructed to approximate appropriate testing pressures. The testing pressures were chosen such that the cylinders will have similar maximum strains of 0.06, 0.08, and 0.10 when the FE models were inflated. The expected material failure occurs around a strain of 0.24, thus the inflatable cylinders were not expected to burst during inflation. The material strain while testing is a combination of the bending stiffness and the internal pressure. While additional strain is expected to develop from the bending load case, the majority of the total strain was expected to come from the internal pressure.

### 6.3 Three Point Bending Test Results

The load displacement results of the three point bending beams can be seen in Figures 6.5 - 6.7. The displacement values were recorded when the beams approached a static state. The variance between the load displacement curves for the bending tests at the same pressure represents the error in the test setup. The beams were placed such that the load was applied in the approximate center of the beam. After each test the beam, draw wire, polyester strap, and collar were repositioned. This repositioning may account for some of the error. In addition it is impossible to inflate the cylinders to the exact same pressure, so a small amount of error may come from the cylinders being at a slightly different inflation pressures. With all these error factors stated, the variance in tests for the same pressure is small, as tests of the same pressure produced similar load displacement curves.

The stiffness of the inflatable beams depends upon geometry and pressure. The larger the diameter of the inflatable cylinder, the stiffer the cylinder was in three point bending. For all beam tests, the internal pressure of the inflatable cylinder was a significant contribution to the bending stiffness. The beams were stiffer in three point bending with higher internal pressures. For a given displacement, the load may change by as much as 30 percent from the low to

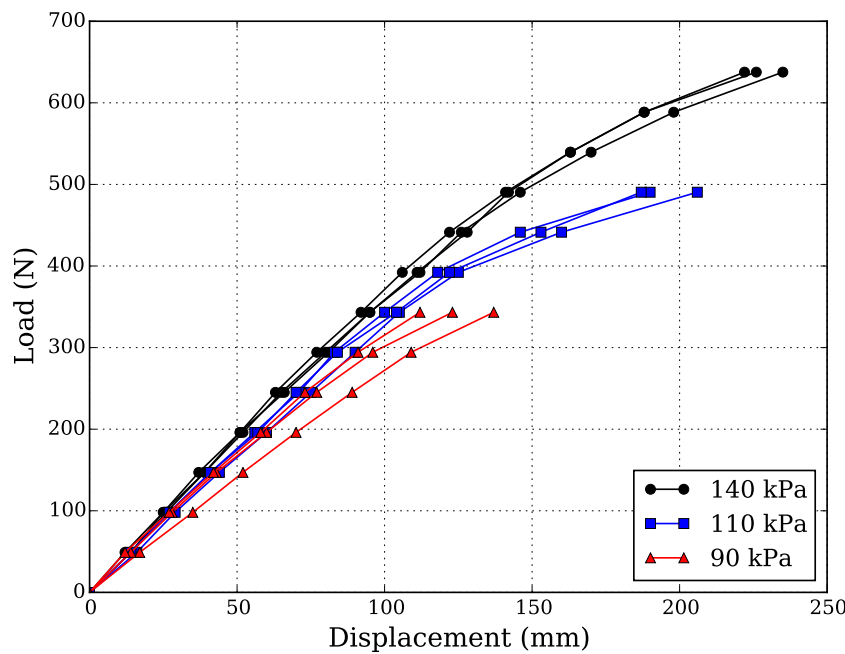


**Figure 6.5:** Center load displacement of the three point bending test on the 150 mm diameter cylinder for three different inflated pressures

high tested pressures.

The internal pressure did not appear to affect the stiffness of the 150 mm diameter cylinder as much as the other two cylinders. However it is noticeable that the buckling load increased with higher pressures, as the 150 mm beam had a higher buckling load at higher pressures. The load of which the 150 mm beam buckled at 140 kPa is almost double the buckling load at 90 kPa. The 200 mm beam at 60 kPa was the only other tested beam configuration to buckle, as all other beam configurations were able to hold the maximum testing weight. A buckled 150 mm beam in the testing configuration is seen in Figure 6.8.

It was surprising to find that the inflatable cylinders produced a linear load displacement curve when tested in three point bending. This is despite the non-linear characteristics of the PVC-coated polyester. However the linear results should have been expected as with the literature discussed in Chapter 2, both mathematical models and beam FE models have successfully predicted the load deflection behavior of inflatable cylinders without the use of non-linear material models.

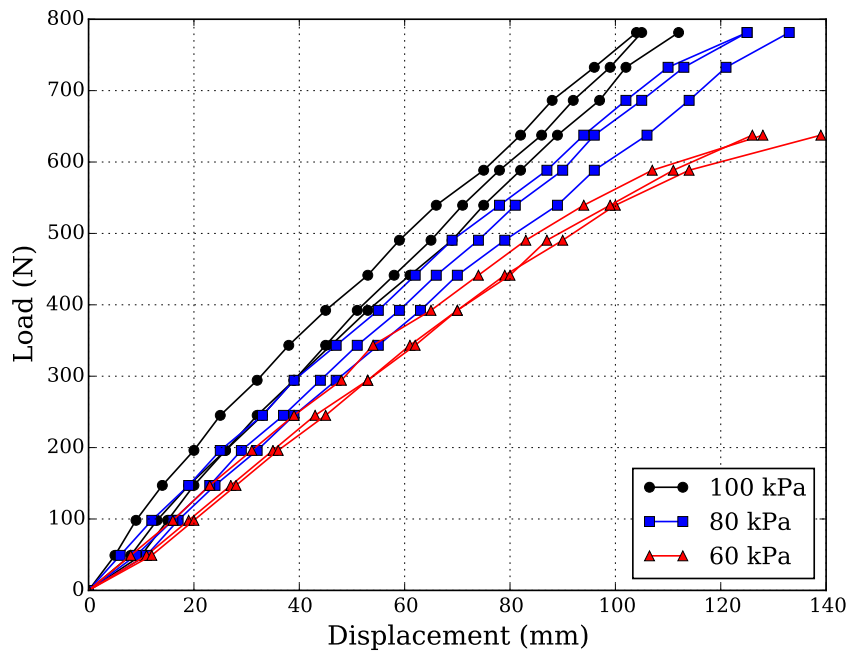


**Figure 6.6:** Center load displacement of the three point bending test on the 200 mm diameter cylinder for three different inflated pressures

## 6.4 Inflatable Beam Bending FE Models

The inflation and three point bending of the inflatable cylinders were modeled using MSC Marc. The mesh used to represent the cylinders was assumed to be a perfect cylinder. Since a number of different cylinder meshes would be required for the three different cylinders, a cylinder meshing script was created in Python. The Python script creates a cylinder mesh based on the arbitrary length, diameter, and desired nominal element size of the cylinder. The meshes created are thin shell linear quad elements, which are the same elements used in the uniaxial and bubble inflation FE models.

Two load cases are used for the FE models. The first load case is the inflation of the cylinder. A cavity is defined to occur on the inside of the shell elements with an enclosed gas. The cavity uses the ideal gas law to calculate changes in mass, pressure, temperature, and volume. The properties of the cavity gas are assumed to be atmospheric air with a reference pressure of 101 kPa, temperature of 300 K, and density of  $1.2041 \frac{\text{kg}}{\text{m}^3}$ . A cavity pressure load is applied with a linear pressure ramp to the desired inflation pressure. The second load case replicates the bending of the inflatable beam. Once the cylinder is inflated, the cavity pressure load changes to a constant mass load. The constant mass load assumes the mass of air to be constant and uses the ideal gas law to calculate the PV work of the bending inflated cylinder.

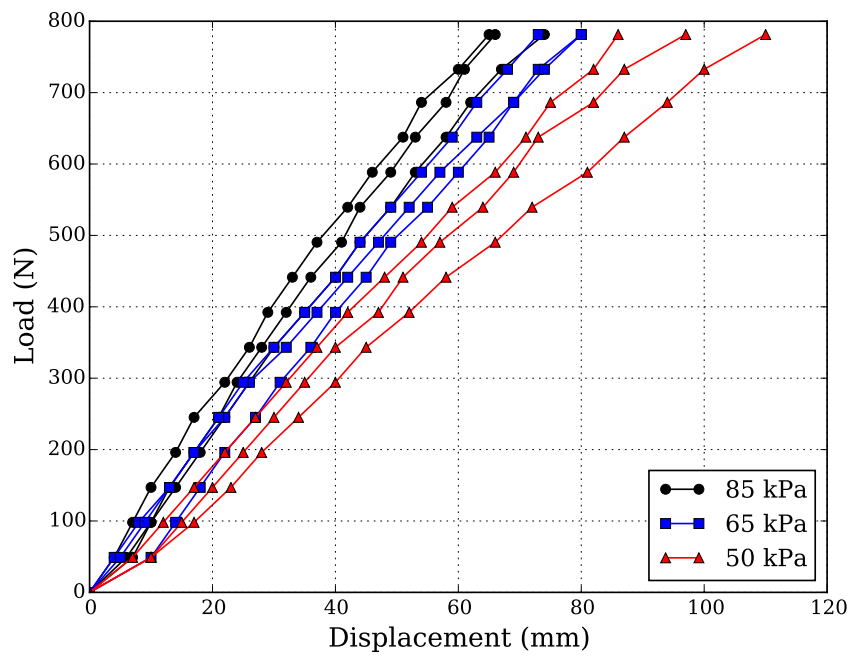


**Figure 6.7:** Center load displacement of the three point bending test on the 250 mm diameter cylinder for three different inflated pressures



**Figure 6.8:** 150 mm diameter inflatable cylinder at the buckling load in the three point bending test configuration

Rigid cylinders were created to model the supports and collar of the three point bending test setup. These rigid cylinders were used as contact bodies and can be seen as the two supports and collar around the inflatable FE model in Figure 6.9. The cylinder is simply supported during inflation, but once the cylinder is inflated the only boundary conditions are the contact between the supports, collar, and inflated cylinder. Displacement control was used in the FE model for both the supports and collar. The two supports are set to have a displacement of zero throughout the bending load case, while the collar dis-

places with a linear displacement ramp perpendicular to the inflatable cylinder. The displacing collar bends the inflatable cylinder as seen in Figure 6.10.

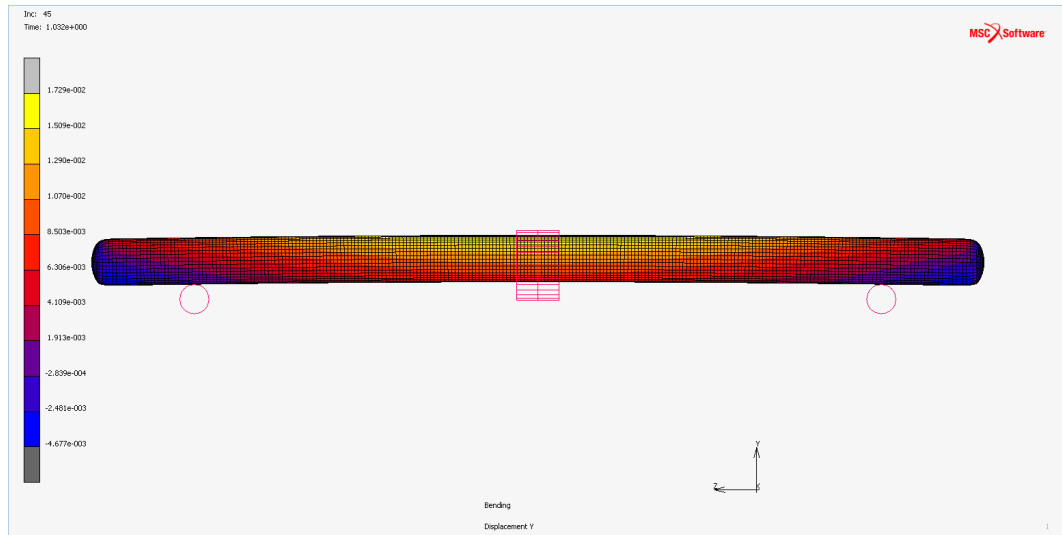


**Figure 6.9:** Inflated 150 mm diameter cylinder in MSC Marc with rigid elements replicating the three point bending boundary conditions

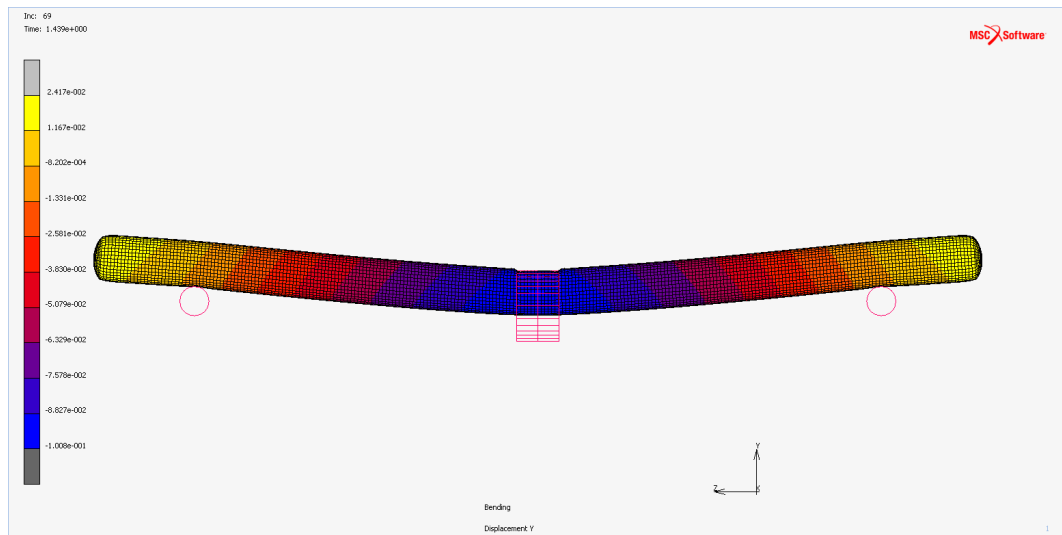


**Figure 6.10:** Bending 150 mm diameter inflatable cylinder FE model due to the displacement controlled rigid collar

Contact is used to model the interaction between the supports and the cylinder, and the interaction between the collar and the cylinder. Both the

supports and collar are geometric rigid cylinders, while the inflatable cylinder is a meshed deformable contact body. Node to segment contact was used with the default Marc contact parameters. Segment to segment contact was used in a test case, in which the load displacement results of the three point bending inflatable beam were nearly identical to the node to segment contact model. The contact normal force was exported along the nodes in contact with the collar to calculate the total three point bending load. In addition, the center node of the cylinder in contact with the collar was also exported. The summation of the contact normal forces as well as the exported displacement node are used to create load displacement curves that can be compared with the physical three point bending tests.

Mesh convergence for the cylinders is demonstrated in Appendix D. It is difficult to perform a full mesh convergence study on the cylinders because wrinkling becomes profound on the cylinder with small element sizes. Wrinkles forming on the FE model creates convergence problems while increasing the computational expense. The meshes used for computation were the finest possible that would allow the cylinder to inflate without issues from the solver.

The seam running down the length of the cylinder is modeled such that shell elements in the area of the seam have triple the thickness, because the seam has three layers of PVC-coated polyester. The triple thickness elements cause the cylinder to have extra stiffness on the one side of the cylinder. The extra stiffness on one side causes the cylinders to inflate with a slight arc as seen in Figure 6.9. This arc is also noticed when inflating the physical PVC-coated cylinders.

It is important to assign an element orientation when using an orthotropic material model, as the material model is direction depended. A local coordinate system was applied to the end caps of the cylinders. The elements on the end cap are aligned in a direction that is representative of the physical cylinders. However, elements along the length of the cylinder use the elemental coordinate system rather than a global alignment. The elemental coordinate system was set up, such that the element's primary direction runs down the length of the cylinder. While the element's secondary direction runs in the circumferential direction of the cylinder. The elemental coordinate system matches the physical construction of the cylinders, because the warp material direction runs along the length of the cylinders.

The FE models capture the pressure volume work of the bending inflatable beam. In general the increase of pressure of the beam is small as the beam undergoes three point bending, because the volume change of the inflatable cylinder is small. Figure 6.11 shows the pressure volume relationship of a 150 mm diameter inflatable cylinder undergoing three point bending. The cylinder was inflated to a pressure of 140.0 kPa prior to bending. The cylinder was deflected a total of 240 mm in three point bending, at which the pressure increased from 140.0 kPa to 141.1 kPa.

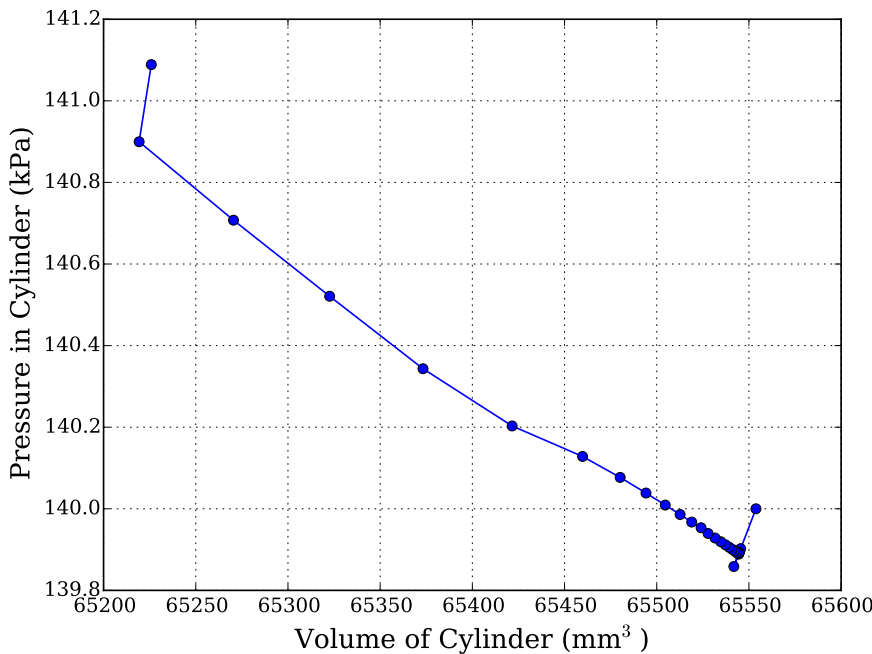


**Figure 6.11:** Pressure volume work of three point bending 150 mm diameter cylinder inflated to 140.0 kPa

## 6.5 FE Bending Results of Material Models

Three point bending FE models were created with the four bubble material models and the uniaxial material model. The results of the 150 mm diameter cylinder are seen in Figures 6.12 - 6.14. The results of the 200 mm diameter cylinder are seen in Figures 6.15 - 6.17. The results of the 250 mm diameter cylinder are seen in Figures 6.18 - 6.20.

The uniaxial material model matches the load displacement curve of the 150 mm diameter cylinder better than the 200 mm or 250 mm diameter cylinders. However for all nine tests, the uniaxial material model underestimates the stiffness of the inflatable beam. The uniaxial material model also matches the load displacement curve better at low pressures than at high pressures.

The variance of the bubble material models is larger than the variance of the physical test data. The bubble material model from test 4 generally falls within the load displacement physical test data. In contrast to the uniaxial material model, the bubble material models overestimate the stiffness of the inflatable beams.

The FE models don't accurately predict the buckling load of the inflatable beams. The load of the physical test results goes above the buckling load in the FE models in Figures 6.13 - 6.15. However before buckling can be predicted by the FE models, the FE models must first be able to accurately predict the

load displacement behavior of the inflatable beams.

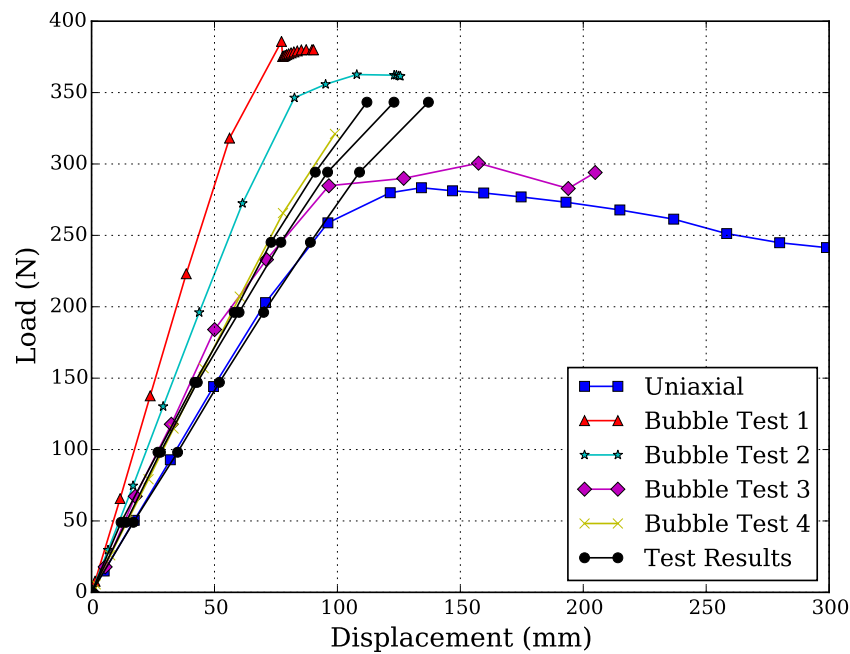


**Figure 6.12:** Three point bending load displacement results of 150 mm diameter cylinder inflated to 90 kPa compared to FE analyses using different material models

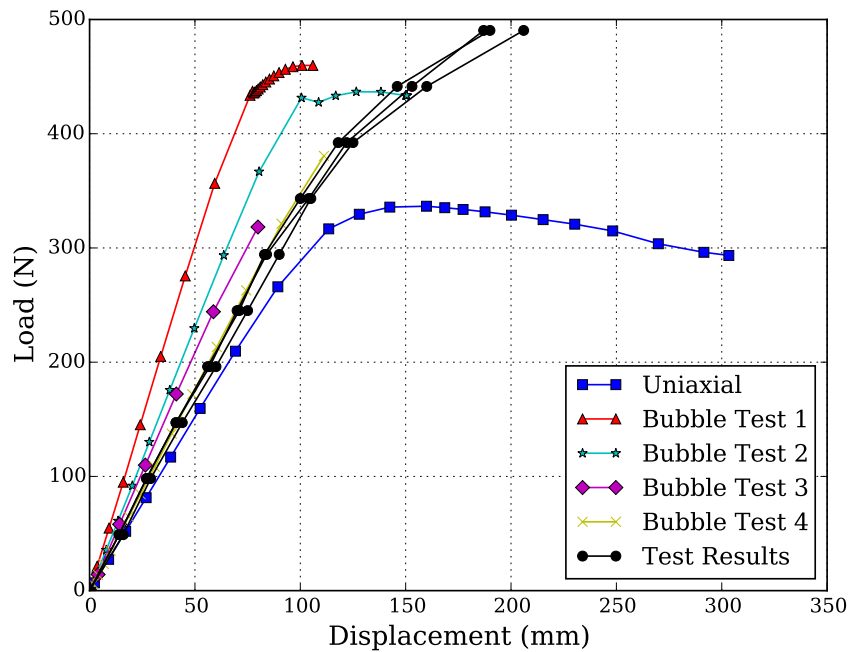


**Figure 6.13:** Three point bending load displacement results of 150 mm diameter cylinder inflated to 110 kPa compared to FE analyses using different material models

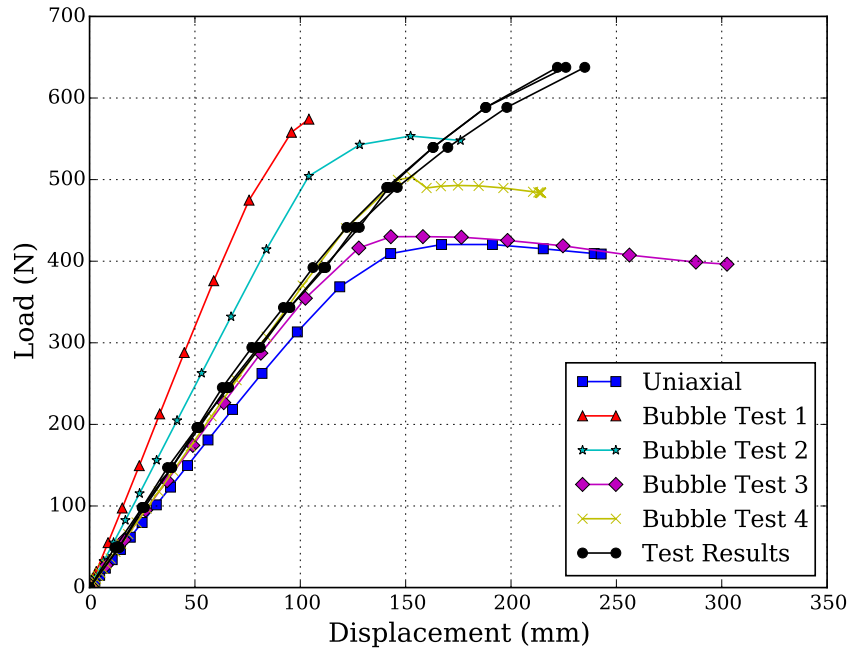


**Figure 6.14:** Three point bending load displacement results of 150 mm diameter cylinder inflated to 140 kPa compared to FE analyses using different material models

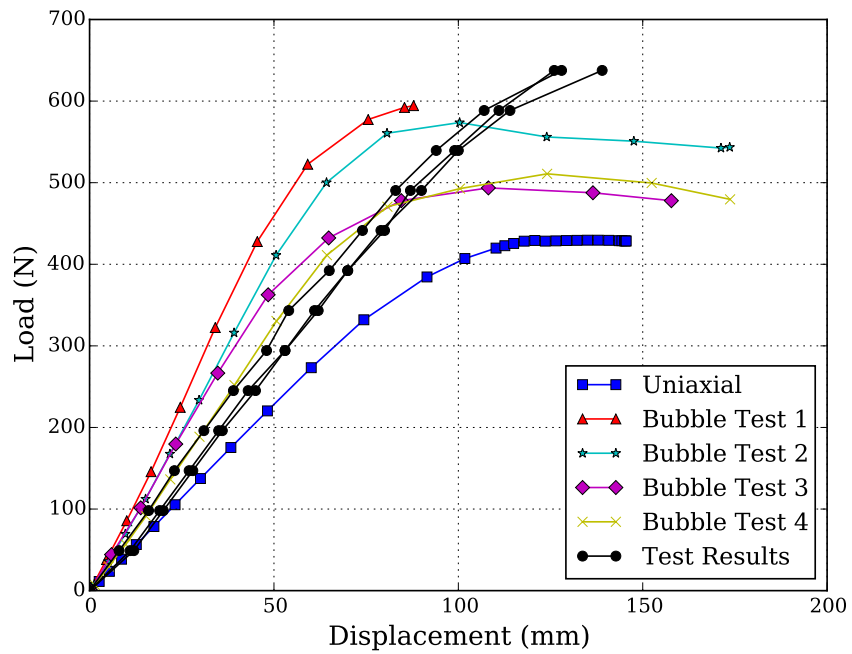


**Figure 6.15:** Three point bending load displacement results of 200 mm diameter cylinder inflated to 60 kPa compared to FE analyses using different material models

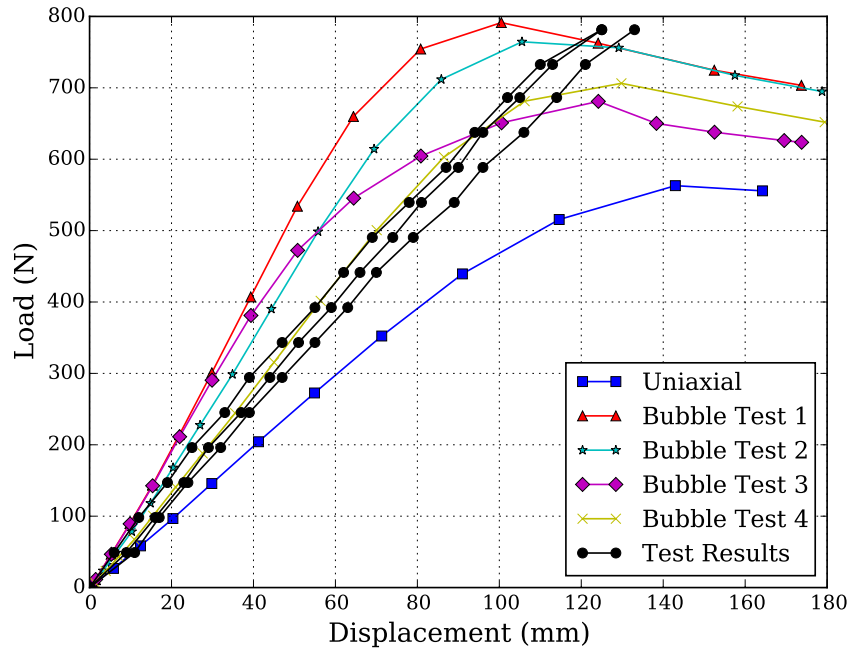


**Figure 6.16:** Three point bending load displacement results of 200 mm diameter cylinder inflated to 80 kPa compared to FE analyses using different material models

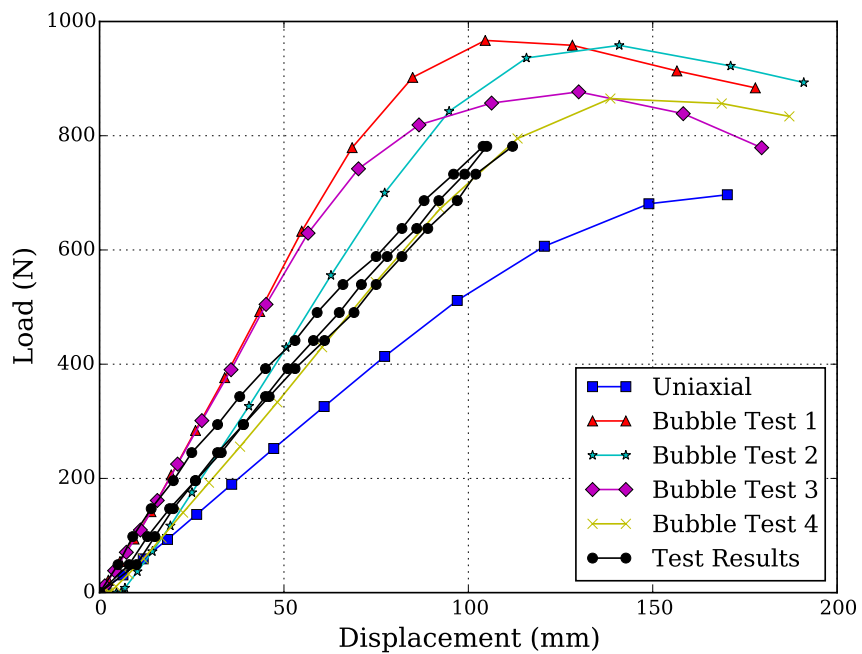


**Figure 6.17:** Three point bending load displacement results of 200 mm diameter cylinder inflated to 100 kPa compared to FE analyses using different material models

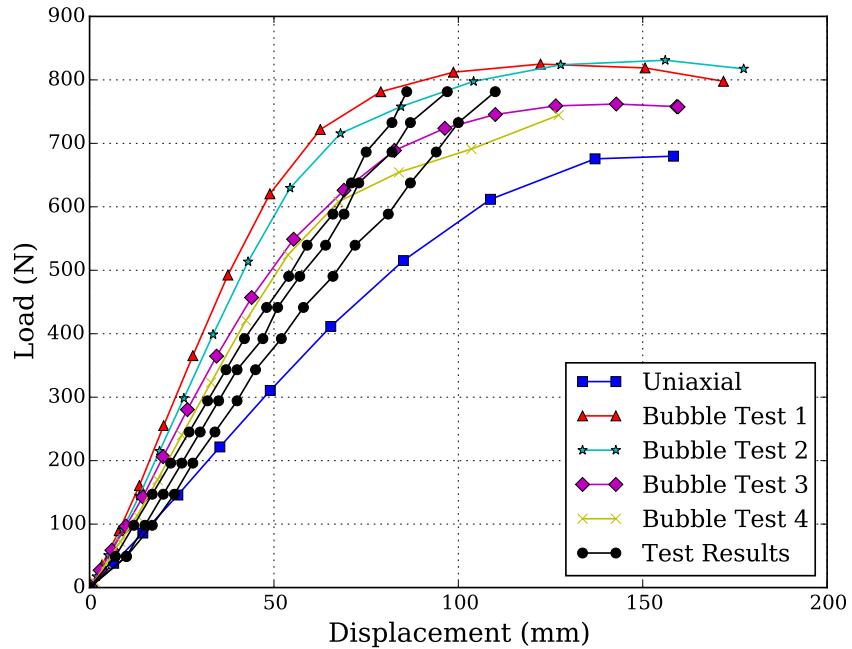


**Figure 6.18:** Three point bending load displacement results of 250 mm diameter cylinder inflated to 50 kPa compared to FE analyses using different material models

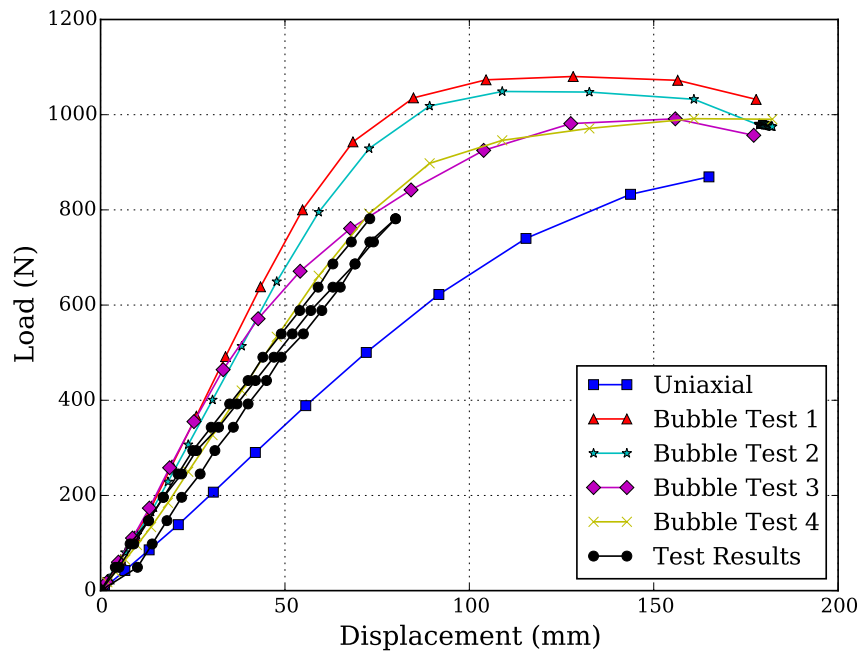


**Figure 6.19:** Three point bending load displacement results of 250 mm diameter cylinder inflated to 65 kPa compared to FE analyses using different material models

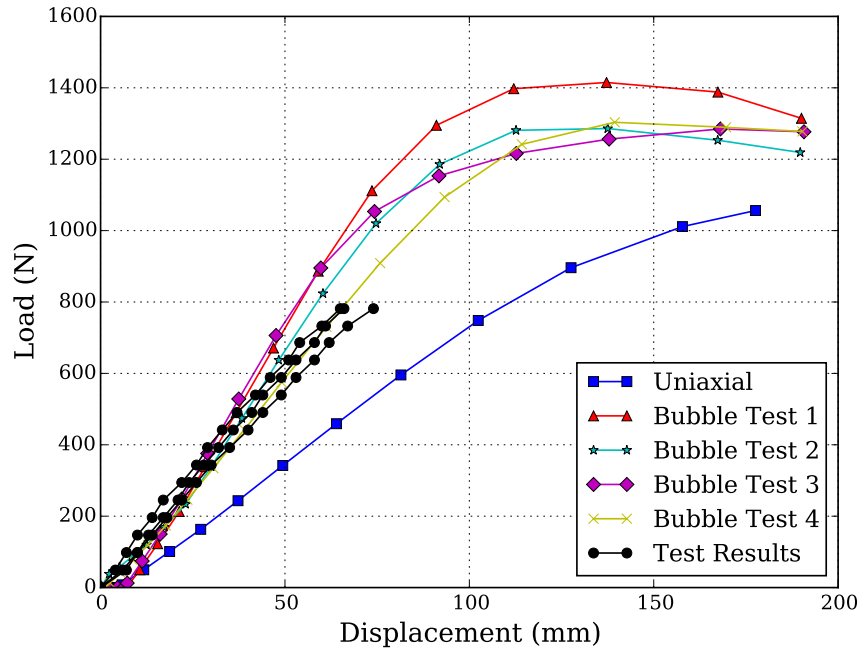


**Figure 6.20:** Three point bending load displacement results of 250 mm diameter cylinder inflated to 85 kPa compared to FE analyses using different material models

# Chapter 7

## Conclusion

Uniaxial tests were performed on PVC-coated polyester, from which a non-linear orthotropic material model was determined. A new inverse bubble inflation method was presented and demonstrated. Non-linear orthotropic material models were determined from bubble inflation tests on PVC-coated polyester. Multiple three point bending tests on PVC-coated polyester cylinders were performed to validate the created non-linear orthotropic material models. The inverse bubble inflation material models had a tendency to overestimate the stiffness of the inflatable beams, while the uniaxial material model underestimated the stiffness.

### 7.1 Uniaxial Material Models

Five uniaxial tests were performed on PVC-coated polyester in each of the warp, fill, and 45° bias material directions. The five tests produced load displacement curves that were similar in each material direction. Finite element (FE) models were created to replicate the warp, fill, and 45° bias uniaxial tests. A non-linear orthotropic material model was determined using optimization to match the load displacement results of the tests in the warp, fill, and 45° bias material directions. The non-linear orthotropic material model matched the warp, fill, and 45° bias uniaxial load displacement data extremely well.

### 7.2 Inverse Bubble Inflation Method

An inverse bubble inflation test was performed from a known non-linear orthotropic material model. It was demonstrated that the test produced non-linear material models similar to the solution. Thus the inverse bubble inflation method is capable of obtaining non-linear material models suitable for FE analysis.

Polynomial surfaces were fitted to the nodal FE displacement results of the known material model. These polynomials are utilized as the solution in the

formation of the objective function. Physical test data can be easily utilized in the established inverse bubble inflation method. Polynomials can be fitted to the full displacement field data that one may obtain by using a multi-camera digital image correlation (DIC) system.

The inverse bubble inflation test requires full displacement field matching. It was first attempted to obtain non-linear material models by matching the bubble shape, however this was unsuccessful. Many different material models were found to produce a similar bubble shape. Thus the nodal  $x$ ,  $y$ , and  $z$  displacements are matched instead, because the full displacement field response is unique to a particular material model.

The inverse method can be utilized to obtain non-linear material models from physical bubble inflation tests through gradient optimization. The performance of non-gradient based optimizations on the inverse bubble test, as well as other algorithms is still unknown. A simulation study can be performed on bubbles originating from shapes other than a circle to improve the effectiveness at characterizing a particular material parameter.

## 7.3 Bubble Inflation Tests

Four bubble inflation tests were performed on PVC-coated polyester. From each bubble test, a non-linear orthotropic material model was determined from the bubble test data by using the method established in Chapter 4. The resulting material models were similar to each other, but different to the non-linear orthotropic material model determined from the uniaxial testing.

The bubble material models were used in FE models that replicate the uniaxial tests. In the material warp direction the bubble material models produced a similar load displacement curve as the uniaxial test. However, the bubble material models produced very different load displacement curves in the fill and  $45^\circ$  bias uniaxial tests. In the fill direction, the bubble material models severely underpredicted the stiffness. While the bubble material model produced a stiffer  $45^\circ$  bias uniaxial response than the physical test in the  $45^\circ$  bias direction.

## 7.4 Inflatable Beam Testing

Three inflatable cylinders were manufactured from PVC-coated polyester, all 3 m in length, with diameters of 150 mm, 200 mm, and 250 mm. Each cylinder was tested in three point bending, at three different inflated pressures.

FE models were created to replicate the three point bending tests. The four bubble material models and, the uniaxial material model were run to understand which material model predicted the load displacement behavior of the three point bending tests the best. In general the bubble material models

overestimated the stiffness of the inflatable beams, while the uniaxial material model underestimated the stiffness. The material model from bubble test 4 matched the entire test data well, however the other bubble material models generally overestimate the stiffness of the beam.

Overall the inverse bubble material models matched the load displacement bending test data as well as the uniaxial material model. The uniaxial material model matched better for the 150 mm diameter cylinder, while the bubble material models matched better with the 250 mm diameter cylinder. The bubble material models overestimated, just as much as the uniaxial material model underestimated, for the 200 mm cylinder.

It is important to address how the material models and bending beam tests each experienced different biaxial load ratios, as the biaxial load ratio may have influenced the results. The biaxial load ratio from the uniaxial tests is infinity, while the bubble test had a load ratio of 1. The material models were created with load ratios that were different than the load ratio of 2 from the inflatable beam tests. At this time the exact effect of the load-ratio dependence of the material is unknown, and it would be recommended for future study to perform biaxial tests on the material with load ratios of 1 and 2 to understand the full effect of the load ratio.

## 7.5 Future Work

Three additional cylinders have been manufactured out of a different PVC-coated polyester. A non-linear orthotropic material model will be calculated for this new PVC-coated polyester from both uniaxial and inverse bubble inflation tests. The material models will be compared against each other, and against the three point bending results of the FE models to see if the results presented in this thesis are repeatable.

The bubble inflation test fixture uses a circular clamp to secure the inflating membrane material. This is traditionally how the bubble test has been performed. The inverse bubble inflation test matches the full displacement field of a bubble test to create a material model. Optimization may be performed on the shape of the bubble test fixture to produce a more unique displacement field that results in more pronounced shear stress for a variety of materials. The more unique a displacement field, the easier it would be for the inverse method to determine the material model.

Polynomial surfaces were fitted to the displacement field at specified increments of the bubble inflation test data. The inverse optimization utilized these polynomials rather than the actual test data. Little time was spent improving the fits of the polynomial surfaces. A mathematical model could be fitted to the entire bubble inflation test data rather than at specific points, which would make it easier for arbitrary bubble tests to be coupled to the inverse FE analysis. Other statistical modeling methods, such as Kriging and

support vector regression, could be used to better model the bubble test data. Potentially superior models of the experimental test data may improve the process of matching material models with the inverse bubble inflation test.

The inverse bubble inflation test method was created with the intention of being a tool for determining non-linear material models for a variety of membrane materials. There is not a well-established method for determining starting points for the inverse optimization problem, as starting points are randomly generated. Thus the first few iterations of the optimization problem are spent improving material model parameters from a poor guess. Machine learning could be included in the package to dramatically improve the computational expense of the inverse bubble inflation tests, by proposing reasonable starting points based on the bubble inflation test data. The results of each FE analysis could be stored in an artificial neural network, which could propose better starting points based on the bubble inflation test data and previously stored material models. Such methods may dramatically improve the feasibility and cost effectiveness of an inverse bubble inflation test method.

An initial study of the Poisson's ratio sensitivity for a bubble FE model showed that the maximum displacement varied by  $\pm 3.0$  percent. It was thought that this difference would make it possible to determine the Poisson's ratio with the inverse bubble inflation technique. However, optimization results from a test problem were unable to determine an appropriate Poisson's ratio for the material model. It is suspected that Poisson's ratio may be non-unique to the bubble test's full displacement field, thus the inverse bubble inflation test would be incapable of determining the Poisson's ratio. A potential project may be to investigate the limitations of the Poisson's ratio in determining material properties for inflatable structures, as the influence of Poisson's ratio for an inflatable structure is still unknown.

# Appendices

# Appendix A

## Digital Image Correlation on Steel Ball

To understand the capabilities of the Digital Image Correlation (DIC) system at capturing a curved surface in three dimensions (3D), images were captured with the DIC on a steel bearing ball having a radius of 40 mm. An equation of a sphere is fit to the data points of the surface captured by the DIC. The radius from the spherical fit and the known radius are compared. The average percent error between the radii was 0.42, suggesting that the DIC data points captured from the ball's surface are accurate.

### A.1 DIC Data on Steel Bearing Ball

Five sets of images were taken on a steel bearing ball having a radius of 40.0 mm using the DIC system. In each set of images, the ball is rotated and moved to a new location in 3D space before images are recorded by the DIC. Data points captured in 3D space can be seen in Figure A.1, where 52,080 data points make up the surface of the steel bearing ball.

Data points missing from the figure are where the DIC failed to find a unique contrast pattern in the subset of the image, or where the surface wasn't visible by both cameras. It is impossible for a two camera DIC system to capture the entire surface of a sphere. The range of which the two camera DIC system was able to correlate data points to the surface of the ball can be seen in Figures A.2 and A.3 for one set of images taken on the ball. In the  $xz$  plane approximately  $90^\circ$  of the ball's surface was captured, while in the  $yz$  plane approximately  $144^\circ$  of the ball's surface was captured by the DIC. This range is largely dependent on the camera setup, as a contrast pattern can only be correlated if the pattern is visible in both cameras. The center point of the sphere was determined by fitting the equation of a sphere to the DIC data points using the least squares method.

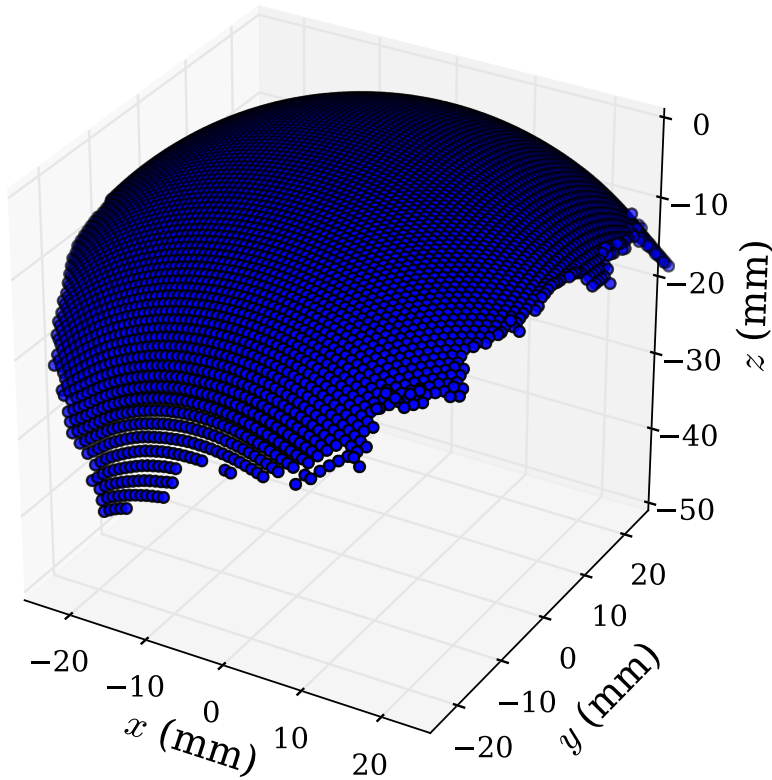


**Figure A.1:** 52,080 DIC data points captured from the surface of the steel bearing ball plotted in 3D

## A.2 Least Squares Spherical Fit

The general equation of a sphere in  $x$ ,  $y$ , and  $z$  coordinates is stated in Eq. A.1. The center point of the sphere with radius  $r$  is found at the point ( $x_0, y_0, z_0$ ). The following expands the general equation of a sphere such that the least squares method can be used to fit to the DIC Data points.

$$(x - x_0)^2 + (y - y_0)^2 + (z - z_0)^2 = r^2 \quad (\text{A.1})$$

After expanding and rearranging the terms, the new equation of a sphere is expressed in Eq. A.2, which needs to be expressed in vector/matrix notation in order to perform a least squares fit.

$$x^2 + y^2 + z^2 = 2xx_0 + 2yy_0 + 2zz_0 + r^2 - x_0^2 - y_0^2 - z_0^2 \quad (\text{A.2})$$

The  $\vec{f}$  vector in Eq. A.3, the  $A$  matrix in Eq. A.4, and the  $\vec{c}$  vector in Eq. A.5 represent the consolidated terms of the expanded sphere equation of Eq. A.2. The terms  $x_i$ ,  $y_i$ , and  $z_i$  represent the first DIC data point, while  $x_n$ ,  $y_n$ , and  $z_n$  represent the last DIC data point on the surface of the ball.

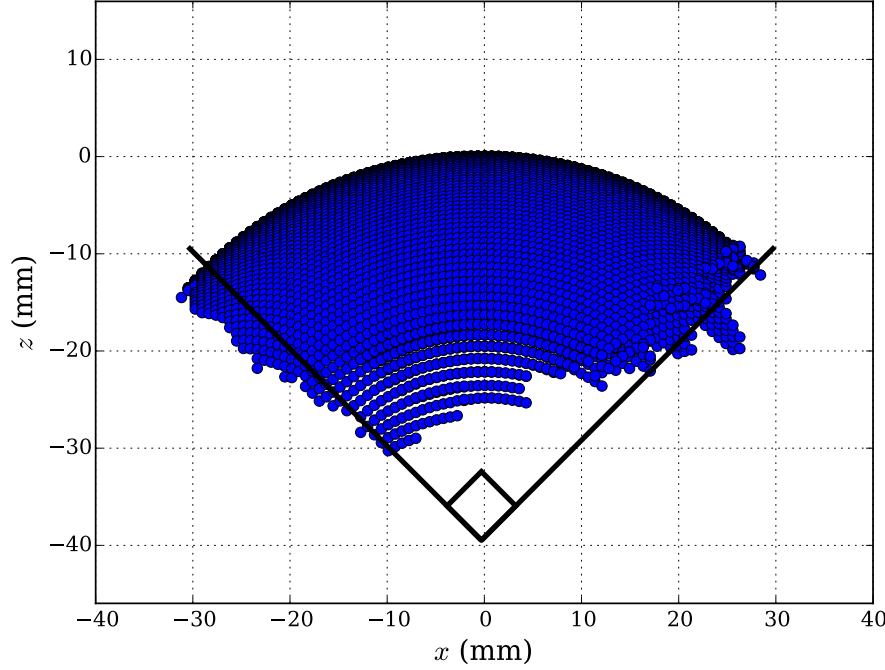


**Figure A.2:** 52,080 DIC data points approximately captured  $90^\circ$  from the surface of the steel bearing ball plotted in the  $xz$  plane

$$\vec{f} = \begin{bmatrix} x_i^2 + y_i^2 + z_i^2 \\ x_{i+1}^2 + y_{i+1}^2 + z_{i+1}^2 \\ \vdots \\ x_n^2 + y_n^2 + z_n^2 \end{bmatrix} \quad (\text{A.3})$$

$$A = \begin{bmatrix} 2x_i & 2y_i & 2z_i & 1 \\ 2x_{i+1} & 2y_{i+1} & 2z_{i+1} & 1 \\ \vdots & \vdots & \vdots & \vdots \\ 2x_n & 2y_n & 2z_n & 1 \end{bmatrix} \quad (\text{A.4})$$

$$\vec{c} = \begin{bmatrix} x_0 \\ y_0 \\ z_0 \\ r^2 - x_0^2 - y_0^2 - z_0^2 \end{bmatrix} \quad (\text{A.5})$$

The over-determined system suitable for the least squares method of a spherical fit is represented in Eq. A.6. The least squares method determines the best  $\vec{c}$  from the DIC data points. Information about the center point and radius of the sphere are contained in  $\vec{c}$ .

A spherical least squares fit was performed to the five sets of images recorded by the DIC. For a single test, the data points captured in 3D space plotted on top of the fitted sphere can be seen in Figure A.4.

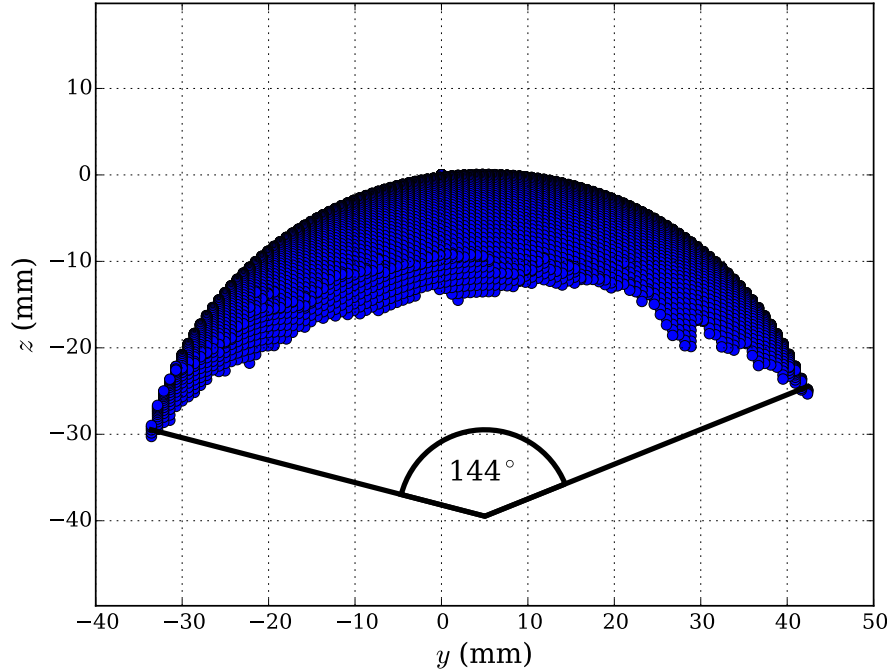


**Figure A.3:** 52,080 DIC data points approximately captured 144° from the surface of the steel bearing ball plotted in the  $yz$  plane

$$\vec{f} = A\vec{c} \quad (\text{A.6})$$

### A.3 Radius Comparison

The radii determined from least squares fit to the DIC data points on the steel ball's surface are presented in Table A.1. All fits determined a radius very near to the 40.0 mm radius of the steel bearing ball, with 0.67 being the worst percent error. The average percent error was 0.42 for the radii. This suggests that the DIC can accurately determine 3D points on a highly curved surface.

**Table A.1:** Radius determined by spherical least squares fit to five sets of DIC images on steel bearing ball

| DIC Image Set | Least Squares Radius (mm) | Percent Error |
|---------------|---------------------------|---------------|
| 1             | 39.73                     | 0.67          |
| 2             | 39.78                     | 0.54          |
| 3             | 39.90                     | 0.23          |
| 4             | 39.85                     | 0.38          |
| 5             | 39.89                     | 0.28          |

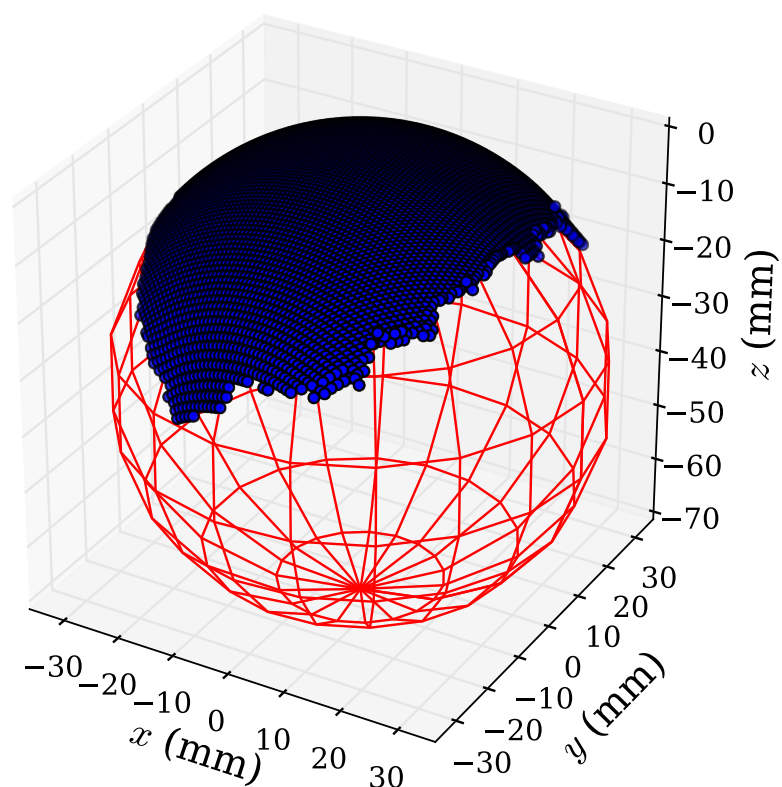


**Figure A.4:** 52,080 DIC data points captured from the surface of the steel bearing ball plotted in 3D on top of the fitted sphere

## Appendix B

### Festo SPTE-P10R-S4-V-2.5K Pressure Transmitter

The Festo SPTE-P10R-S4-V-2.5K pressure transmitter was used as the relative pneumatic pressure recording device for the bubble inflation tests and the inflatable beam tests. The device is powered by direct current with a potential of 18 - 30 volts, and has a pressure measuring range of 0 - 1,000 kPa. The SPTE converts relative pneumatic pressure into an analog reading, such that 0 volts occurs at a relative pressure of 0 kPa and 10 volts is outputted at a pressure of 1,000 kPa. The SPTE has an accuracy of  $\pm$  3 percent at ambient temperature with a repetition accuracy of  $\pm$  0.3 percent. Both accuracies are rated for the full scale pressure range, meaning the accuracy at ambient pressure is  $\pm$  30 kPa with a repetition accuracy of  $\pm$  3 kPa.

Simultaneous measurements were recorded with the SPTE and a Druk-meter 2500 kPa Wika Instruments to ensure the accuracy of the SPTE. The accuracy of the Wika Instruments pressure gage was  $\pm$  75 kPa. The raw results of the test is presented in Figure B.1, where it is seen that the SPTE and Wiki Instruments pressure gage are in strong agreement. No adjustments were made to the SPTE readings as the data collected falls within the accepted accuracies of both devices.

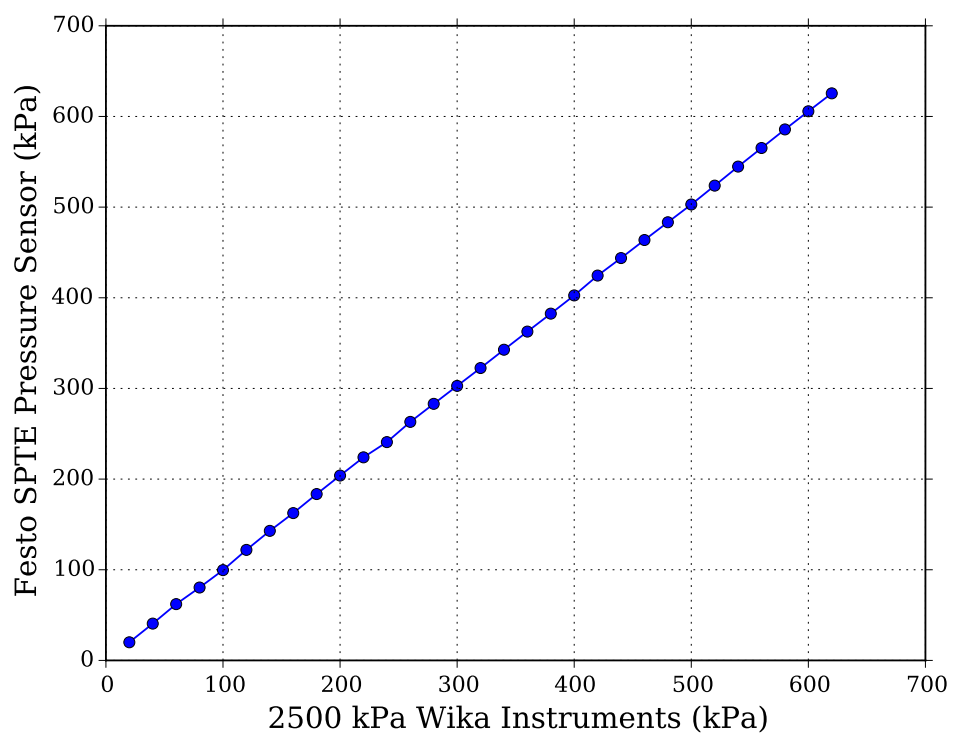


**Figure B.1:** Agreement of raw SPTE and Wiki Instruments pressure values

## Appendix C

### ASM Posiwire WS12-2000-10V-L10 Draw Wire

The ASM Posiwire WS12-2000-10V-L10 draw wire position transmitter was used to measure the displacement of the three point bending tests. The draw wire is limited to a length of 2,000 mm. The device outputs an analog voltage of 5 volts per 1,000 mm. The draw wire was pulled alongside a meter stick to understand the accuracy of the sensor. The values measured by the ASM Posiwire WS12-2000-10V-L10 sensor were within  $\pm 1$  mm of the meter stick reading and are presented in Figure C.1. The draw wire position sensor was determined to be highly accurate device for measuring displacement.

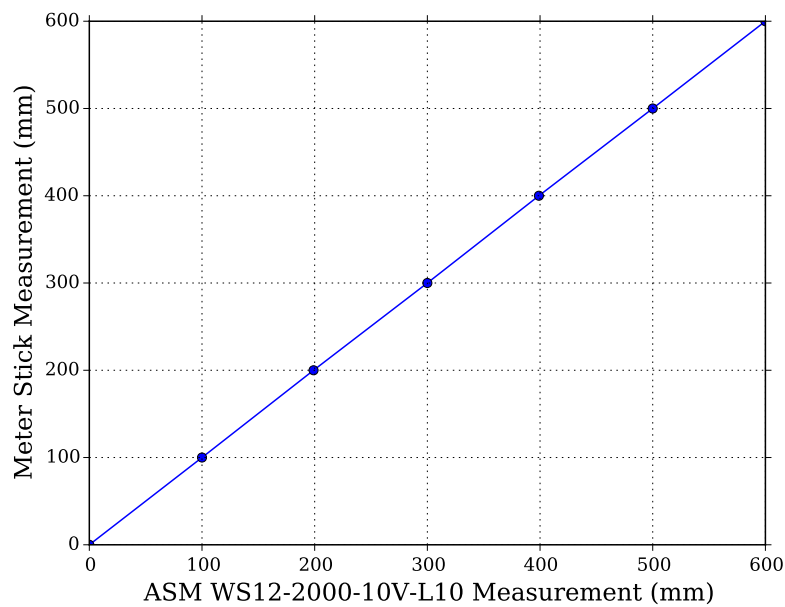


**Figure C.1:** Agreement of ASM Posiwire WS12-2000-10V-L10 draw wire position sensor and meter stick displacement measurements

## Appendix D

### Three Point Bending Mesh Convergence

Convergence behavior is demonstrated in Figure D.1 for the 150 mm cylinder. It is shown that the 10,760 element mesh produces a load displacement curve for three point bending that is analogous to the 3,864 element mesh. The 10,760 element mesh was used for the Finite Element (FE) models of the 150 mm cylinder.

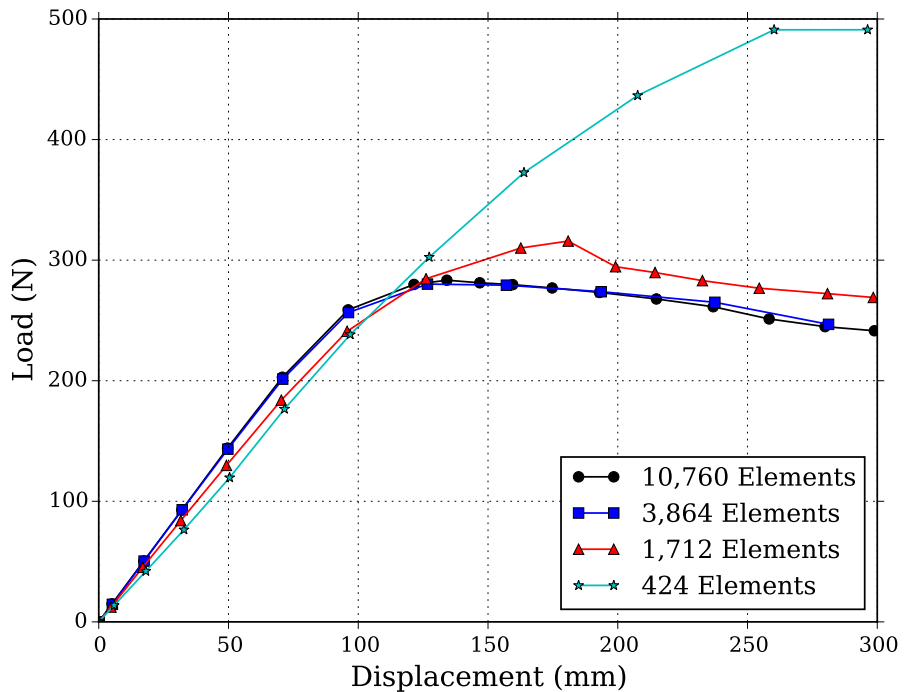


**Figure D.1:** Demonstrated load displacement mesh convergence for the 150 mm cylinder in three point bending

Convergence behavior is demonstrated in Figure D.2 for the 200 mm cylinder. It is shown that the 16,130 element mesh produces a load displacement curve for three point bending that is analogous to the 2,952 element mesh. The 2,952 element mesh was used rather than the 16,130 element mesh to reduce the computational time of the FE models for the 200 mm cylinder.

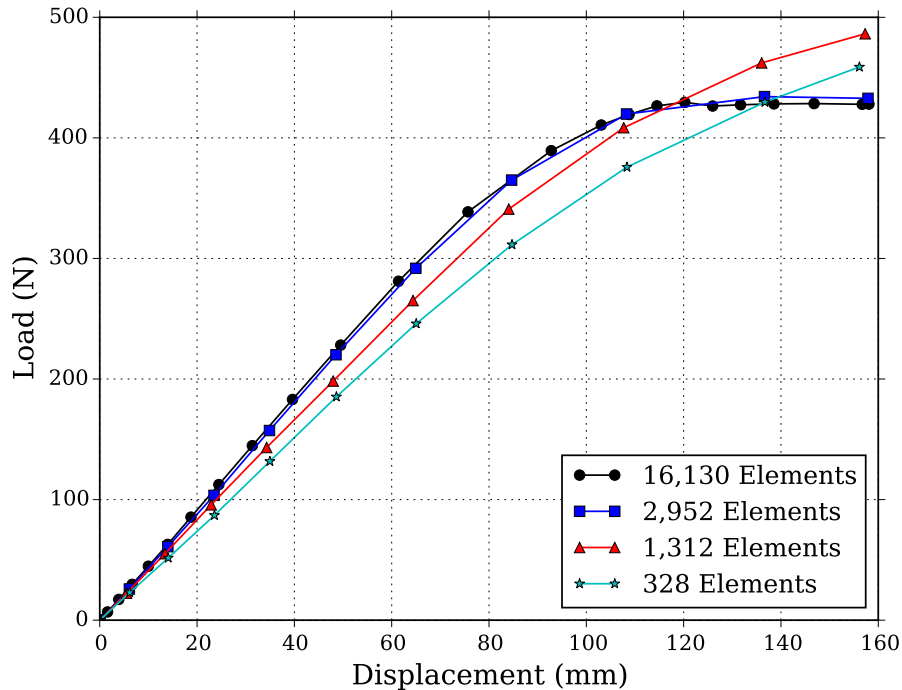


**Figure D.2:** Demonstrated load displacement mesh convergence for the 200 mm cylinder in three point bending

Convergence behavior is demonstrated in Figure D.3 for the 250 mm cylinder. It is shown that the 4,288 element mesh produces a load displacement curve for three point bending that is analogous to the 2,400 element mesh. The 4,288 element mesh was used for the Finite Element models of the 250 mm cylinder.

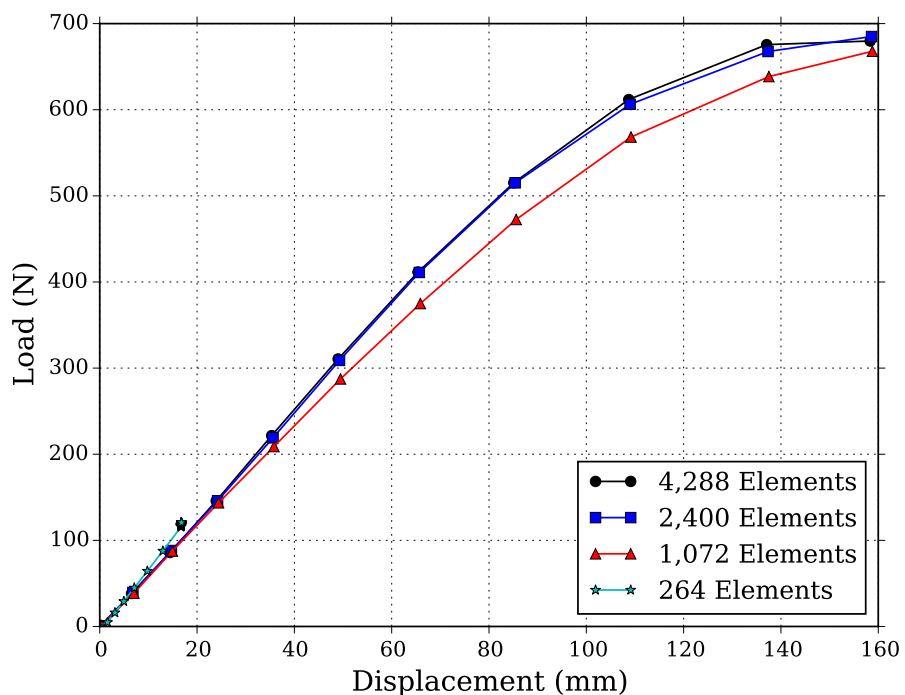


**Figure D.3:** Demonstrated load displacement mesh convergence for the 250 mm cylinder in three point bending

# List of References

- Ambroziak, A. and Kłosowski, P. (2014 January). Mechanical properties for preliminary design of structures made from PVC coated fabric. *Construction and Building Materials*, vol. 50, pp. 74–81. ISSN 09500618.
- ASTM D751 - 06 (2011). *Standard Test Methods for Coated Fabrics*. January.
- Cairo, R. (2011 May). Inflatable wind turbine blade and method for forming said rotor blade.  
Available at: <http://www.google.com/patents/US7938623>
- Cavallaro, P.V., Johnson, M.E. and Sadegh, A.M. (2003). Mechanics of plain-woven fabrics for inflated structures. *Composite Structures*, vol. 61, no. 4, pp. 375–393.
- Charalambides, M., Wanigasooriya, L., Williams, G. and Chakrabarti, S. (2002 January). Biaxial deformation of dough using the bubble inflation technique. I. Experimental. *Rheologica Acta*, vol. 41, no. 6, pp. 532–540. ISSN 0035-4511.
- Chen, S., Ding, X. and Yi, H. (2007 June). On the Anisotropic Tensile Behaviors of Flexible Polyvinyl Chloride-coated Fabrics. *Textile Research Journal*, vol. 77, no. 6, pp. 369–374. ISSN 0040-5175.
- Cook, R., Malkus, D., Plesha, M. and Witt, R. (2002). *Concepts and Applications of Finite Element Analysis*. 4th edn. John Wiley & Sons, Inc. ISBN 978-0-471-35605-9.
- Davids, W.G., Zhang, H., Turner, A.W. and Peterson, M. (2007 July). Beam Finite-Element Analysis of Pressurized Fabric Tubes. *Journal of Structural Engineering*, vol. 133, no. 7, pp. 990–998. ISSN 0733-9445.
- Galliot, C. and Luchsinger, R. (2009). A simple model describing the non-linear biaxial tensile behaviour of PVC-coated polyester fabrics for use in finite element analysis. *Composite Structures*, vol. 90, no. 4, pp. 438–447. ISSN 02638223.
- Galliot, C. and Luchsinger, R.H. (2011). Uniaxial and biaxial mechanical properties of ETFE foils. *Polymer Testing*, vol. 30, no. 4, pp. 356–365.
- Garbowski, T., Maier, G. and Novati, G. (2011 December). On calibration of orthotropic elastic-plastic constitutive models for paper foils by biaxial tests and inverse analyses. *Structural and Multidisciplinary Optimization*, vol. 46, no. 1, pp. 111–128. ISSN 1615-147X.

- LaVision GmbH (2014a). *Product-Manual DaVis 8.2 Software*. 8th edn. Göttingen, Germany.
- LaVision GmbH (2014b). *Product-Manual StrainMaster Portable*. 8th edn. Göttingen, Germany.
- LaVision GmbH (2015). *StrainMaster Advanced Digital Image Correlation Systems for Optical Full Field Measurement of Material Strain, Displacement and Shape*. Göttingen, Germany.  
Available at: [lavision.de/products/strainmaster/strainmaster-dic.php](http://lavision.de/products/strainmaster/strainmaster-dic.php)
- Luchsinger, R., Pedretti, A., Pedretti, M. and Steingruber, P. (2004). The new structural concept Tensairity: Basic principles. *Progress in Structural Engineering*, pp. 1–5.
- Luchsinger, R.H., Sydow, A. and Crettol, R. (2011). Structural behavior of asymmetric spindle-shaped Tensairity girders under bending loads. *Thin-Walled Structures*, vol. 49, no. 9, pp. 1045–1053.
- Main, J.A., Peterson, S.W. and Strauss, A.M. (1994 April). Load Deflection Behavior of Space Based Inflatable Fabric Beams. *Journal of Aerospace Engineering*, vol. 7, no. 2, pp. 225–238. ISSN 0893-1321.
- MSC Marc (2014). *Volume A : Theory and User Information*. MSC Software Corporation.
- Norris, R.K. and Pulliam, W.J. (2009). Historical Perspective on Inflatable Wing Structures. *50th AIAA/ASME/ASCE/AHS/ASC Structures, Structural Dynamics, and Materials Conference*, vol. AIAA, no. 2145.
- Reuge, N., Schmidt, F.M., Le Maoult, Y., Rachik, M. and Abbé, F. (2001 March). Elastomer biaxial characterization using bubble inflation technique. I: Experimental investigations. *Polymer Engineering and Science*, vol. 41, no. 3, pp. 522–531. ISSN 00323888.
- Roland, K. and Martin Fritzsche (2008 February). Rotor blade for wind farms.  
Available at: <https://www.google.com/patents/EP2025928A2?cl=en>
- Snyman, J.A. (2005). *Practical Mathematical Optimization*. Springer, New York. ISBN 0-387-24348-8.
- Tegen, S., Hand, M., Maples, B., Lantz, E., Schwabe, P. and Smith, A. (2012). 2010 Cost of Wind Energy Review. Tech. Rep., National Renewable Energy Laboratory, Golden.  
Available at: <http://www.nrel.gov/docs/fy12osti/52920.pdf>
- Thomas, J.C. and Wielgosz, C. (2004). Deflections of highly inflated fabric tubes. *Thin-Walled Structures*, vol. 42, no. 7, pp. 1049–1066.
- Vanderplaats Research & Development Inc. (2001). *DOT Users manual*. 5th edn. Colorado Springs, CO.

- Venter, G. (2010). Review of Optimization Techniques. *Encyclopedia of Aerospace Engineering*.
- Wielgosz, C. and Thomas, J.-C. (2002 June). Deflections of inflatable fabric panels at high pressure. *Thin-Walled Structures*, vol. 40, no. 6, pp. 523–536. ISSN 0263-8231.
- ZENG, P. (2013). Inflatable/deflatable wind turbine blade structure.  
Available at: <https://www.google.com/patents/WO2013040879A1?cl=en>